DOCTORAL DISSERTATION

Fundamental study on the improvement of the performance and durability of nonwoven filter media

（ろ布の高性能化・長寿命化のための基礎的研究）

Written by

Mohammad Irwan Fatkhur Rozy

Supervisor

Kunihiro Fukui

Fine Particle Technology Laboratory

Department of Chemical Engineering

Graduate School of Engineering

Hiroshima University

September 2021

Abstract

The filtration processes have recently received more attention to meet air pollutant emission standards, which have become stricter because of the urgent need to improve the air quality and reduce the emission of contaminants that may be harmful to human health. Thus, a filter media with high durability and excellent performance is required to overcome this problem. Polyphenylene sulfide (PPS) nonwoven fabric filters having excellent chemical, thermal, and mechanical properties are one of the promising options to meet these criteria. A brief description of each chapter in this dissertation is shown below.

Chapter 1 provides the background and the motivation for current research on the fundamental study on the improvement of the performance and durability of filter media. The description of the filter media and a review of the previous studies were presented in both experimental and numerical simulations utilizing filter media.

At first, in **Chapter 2**, this dissertation focused on the degradation of polyphenylene sulfide (PPS) nonwoven bag filter media by NO_2 gas at high-temperature conditions. The durability test was examined based on the "Test method for evaluating the degradation of characteristics of cleanable filter media" which was specified in ISO16891:2016. The exposure time was varied to investigate the degradation process on the PPS filter. It is found that NO_2 gas at high temperature reduced the tensile strength and elongation of the PPS filter in both transverse direction (TD) and machine direction (MD) with increasing exposure time. Some damage was also found in the morphological appearance of the PPS fiber which led to reduce the tensile strength of PPS filter media. A model to estimate the change in the NO_2 gas concentration in the exhaust gas and the change in the tensile strength was proposed. Our model successfully estimated the degradation of tensile strength in both MD and TD direction, regardless of NO_2 concentration in the exhaust gas.

Numerical simulation was utilized to perform the permeation of gas through a fibrous filter in **Chapter 3** by coupling computational fluid dynamics and immersed boundary method. The realistic geometry of polyphenylene sulfide (PPS) and polyimide (PI) fibrous filter were re-constructed using X-ray computed tomography (CT) images. The simulated pressure drop of each filter media was then compared with the experimental data and existing empirical equation to validate our numerical method. Our simulated pressure drops were in good agreement with the experimental and empirical equation results. Our numerical method

was also useful to investigate flow characteristics in a fibrous filter, where the permeability of the PI filter was lower than the PPS filter under the same porosity conditions.

In **Chapter 4**, numerical simulation of permeation of particles through PPS fibrous filter was performed by utilizing signed distance function. We proposed a method to calculate the signed distance function around complex geometry of filter microstructure by using the Phase-field model and the Level set method. By this method, we could reasonably describe the contact behavior between particles and fiber. Our result showed that the permeation behavior of particles was significantly affected by porosity and the structure of the filter media such as the arrangement and fiber orientation. It was found that the particles tend to contact the perpendicular orientation fibers than parallel orientation fibers because the projected contact area of the perpendicular orientation fiber was larger.

General conclusions of all topics are listed in **Chapter 5**. Suggestions for further research utilizing nonwoven filter media are also proposed.

Contents

List of Figures

List of Tables

Chapter 1

Introduction

Air pollution is a global problem for much of the developing country which become our concerns nowadays. Airborne particulate matter (PM) is detrimental to health, and has been estimated to cause between 3 and 7 million deaths every year, primarily by creating or worsening cardiorespiratory disease[1–3]. The electric power plants, industrial facilities, automobiles, and biomass burning are the sources of the particulates matter. Currently, there are several air pollution control device that commonly used to reduce the air pollution i.e., scrubbers, bag filter, cyclones, and electrostatic precipitator (EP). Bag filter system and electrostatic precipitator have been increasingly to be used in the industrial plant to meet air pollutant emission standards, which have become stricter because the urgent need to improve the air quality and reduce the emission contaminant that harmful to human health[4]. By using special fabric for special separation purpose, the high efficiency of the bag filter system can be guaranteed.

1.1 Nonwoven fabrics filter media

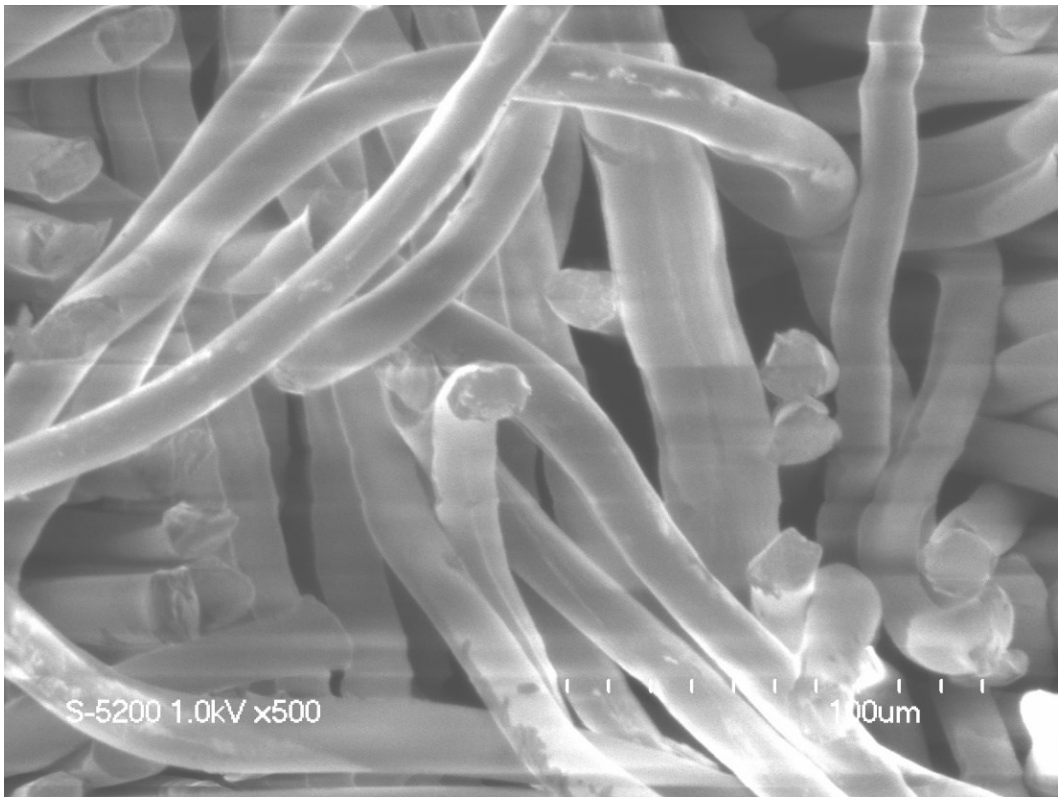

Figure 1.1 Scanning electron microscope (SEM) image of poly-phenylene sulfide fibrous filter

Nonwoven fabric filter is one of most used filtration media. This type of filter is typically composed of randomly packed arrays of fibers, which may be composed of molten plastic, stainless steel, glass fiber, or various polymers, and typically have very low densities. They are flat or tufted porous sheets and they are not made by weaving or knitting and do not require converting the fibers to yarn. Generally, they are called fibrous filters[5,6]. **Figure 1.1** shows a scanning electron microscope (SEM) image of polyphenylene sulfide (PPS) fibrous filter.

In comparison with woven fabric filters, nonwoven offers many unique technical characteristics including greater permeability, greater specific surface area, and controllable pore size distribution as well as smaller pore sizes. This type of filters also has the advantages of greater filtration efficiency, lower energy consumption, and better cake discharge properties over woven filtration media.

Various types of fibers could be used in making nonwoven fabric filter, they include glass fibers, synthetic fibers, cellulosic fibers (e.g., natural wood pulp fibers, viscose fibers and lyocell fibers), wool fibers, metal fibers, ceramic fibers, high-performance fibers (e.g., inherently fire-resistant fibers, chemical resistance fibers, high strength, and high modulus fibers), microfibers and nanofibers.

Nonwoven filters have diverse applications in many sectors in air, gas, and liquid filtrations. Air and gas filtrations consume approximately 65–70 % of the nonwoven filtration media, with liquid filtration accounts for the remaining 30–35 % [7]. The examples of their bulk applications include air and water filtrations in heating, ventilation, and air-conditioning (HVAC) applications in residential, office, and commercial space. Nonwoven elements are also widely used in coalescing filters in the oil and gas sectors to remove entrained droplets form gases and mist, as well as employed in gases and blood filtrations for medical applications, and wastewater filtration in environmental industries.

1.2 Polyphenylene-sulfide

Polyphenylene sulfide (PPS) as a byproduct of chemical reactions was discovered by Charles Friedel and James Mason Crafts in the 1888s for the first time[8,9]. PPS is a thermoplastic polymer consisting of benzene and sulfide atoms and its glass transition temperature (T_g) is 85 ºC and melting temperature (T_m) is 285 ºC [10–12]. A commercially important preparation procedure of PPS involves the polycondensation of 1,4-dichlorobenzene and sodium sulfide in polar solvent, such as *N*-methyl pyrrolidone, at high temperature and pressure [13]. **Figure 1.2** illustrate the chemical structure of PPS.

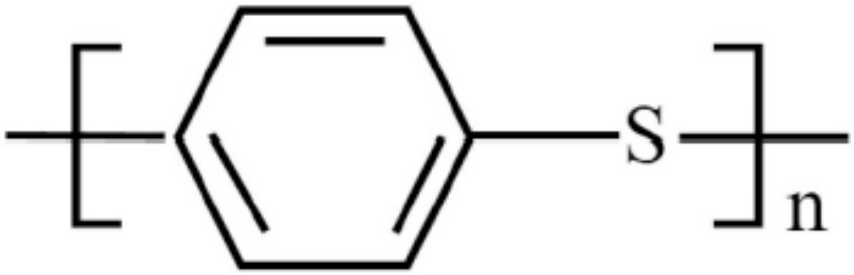

Figure 1.2 Chemical structure of PPS

PPS possesses high temperature resistance combined with good mechanical properties, exceptional chemical, and solvent resistance, high dimensionally stability, and easy processing. PPS has been increasingly used owing to its excellent chemical, thermal, and mechanical properties [14–18]. Several researchers have been investigated the effect of harmful materials on the degradation of PPS filter media.

In 2006, Tanthapanichakoon et al. investigated degradation of semi-crystalline PPS bag-filter materials by NO and O_2 at high temperature [19]. Their results showed that the relation between strength and crystallinity is based on two things: strength is dominated by crystallinity, and strength is dependent on the defect in amorphous regions and some parts of crystalline regions. The annealing effect leads to re-crystallization, resulting in a higher crystallinity thus increase the strength of the fabrics. An increase in NO concentration has a potential to increase the deterioration rates of amorphous and crystalline phases, but the crystallization process is unaffected. An increase in O_2 concentration leads to enhancement of both crystallization and deterioration.

Tanthapanichakoon continued their study by investigating mechanical degradation of PPS polymer filter materials. They checked the durability of PPS nonwoven fabrics to HNO_3, H_2SO_4, and HCl [20]. Their results showed that PPS nonwoven fabrics has high resistance to acid exposures by hydrochloric and sulfuric acids while significant degradation of PPS was induced by nitric acid, especially at high concentration of HNO_3 because of the polyarylene sulfoxide formation. Even though the HCl and H_2SO_4 are not harmful to PPS filter materials, they accelerate degradation of HNO_3 in the binary and tertiary mixtures, leading to lower retention of strength than the sum of their individual effects. They also recommend using PPS nonwoven fabrics in the incineration plant below 200 ºC and at NO concentration far below 1000 ppm to avoid the faster degradation of PPS nonwoven fabrics [21]. Chang et al. then studied the effect of SO_2 in flue gas on PPS filter media used in baghouse [22]. Their results showed that PPS filter media had good corrosion resistance to

SO_2 and was competent in disposal of flue gas which contains SO_2. However, SO_2 still had an effect on PPS filter media where the corrosion increased with the increase of SO_2 concentration and exposure time. When the temperature was above 210 ºC, the breaking strength of PPS filter media declined greatly. Mao et al. also experimentally studied the effect of SO_2 and NO on the durability of PPS filter media[23–25]. They proposed a new testing method of filter media durability for corrosive gas proof performance. Both experiments were performed under 1000 ppm of SO_2 and NO at 200 ºC. Their results showed that both SO_2 and NO gas increasing the warp strength and weft strength at the beginning and then gradually decreased with increasing exposure time. The change for both strength and elongation is higher than the warp.

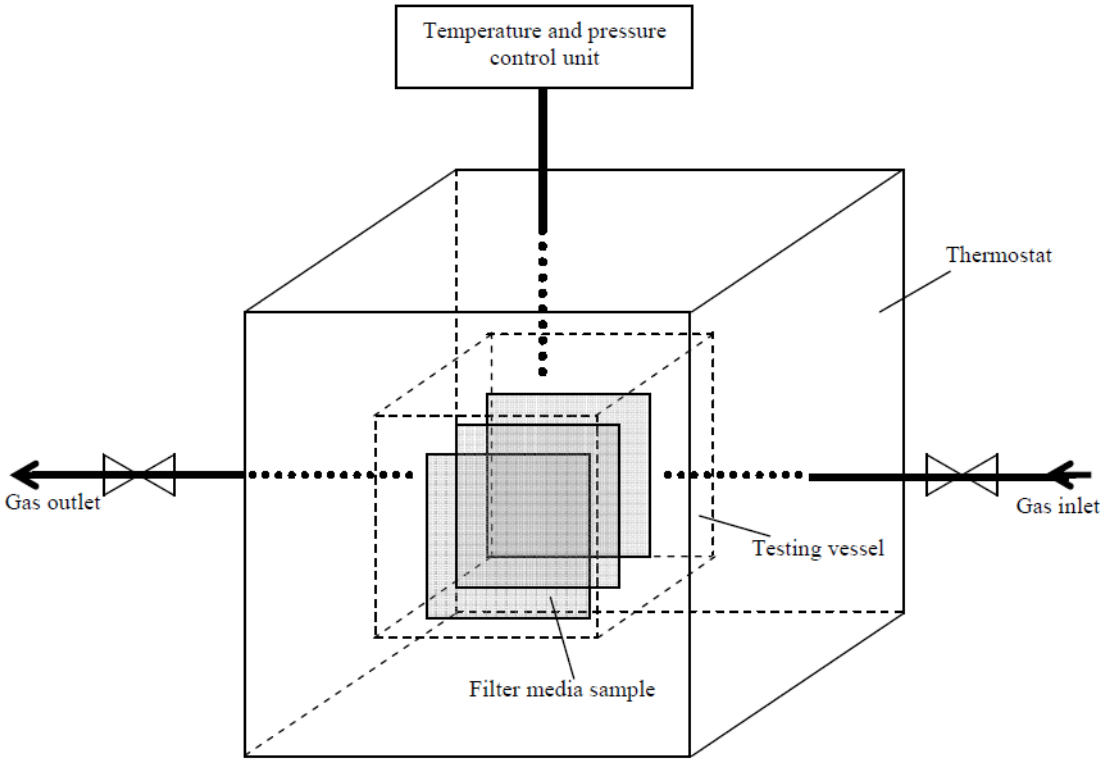

Figure 1.3 The schematic diagram of the corrosive gas proof performance testing rig for filter media durability proposed by Mao. [19]

Cai and Hu studied the oxidation degradation of PPS needle felt at different sulfuric acid dew point temperature [26]. They predict the oxidation reaction mechanism using Fourier transform infrared (FTIR) analysis. Their results showed that the degradation starts with S atoms in the PPS molecular chain. The thioether bond was broken, followed by sulfonation of benzene, and finally concluding with the carbonization of PPS. They also confirmed that H_2SO_4 dew point temperature determines the degree and the route for the oxidation reaction

between PPS needle felt and H_2SO_4. Recently, Wang et al. investigated the thermal aging performance of two kinds of PPS composites reinforced by glass fiber (GF) in high temperature [27]. They compared the tensile strength, oxidation layer thickness, color, crystallization and melting behavior of aged GF/PPS composites. Their results revealed that tensile strength of GF/PPS composites was significantly decreased with increasing of aging time below 200 h. The thermal aging results in the formation of crystal with higher melting point to increase the melting temperature of GF/PPS composites. They found that addition of epoxy resin can increase the mechanical property and the thermal aging performance of GF/PPS composites. The tensile strength of GF/PPS composite modified by resin was higher than the original GF/PPS composite. The oxidation layer thickness of modified GF/PPS composite was significantly thinner than that of original GF/PPS composite.

1.3 Application of polyphenylene sulfide nonwoven filter

1.3.1 Application in air filtration system

Suspended particulate matter (PM) pollution has becoming an urgent problem with the rapid development of the industry [28]. PM pollution mainly result from resources and energy combustion like petroleum industry, metallurgical industry, iron and steel industry, waste incinerator as well as coal-fired power plants, which seriously affected the living environments in terms of air quality ecological environment, atmospheric visibility, and traffic safety. Moreover, PM has characteristics of large surface area, high activity, and easy to carry a large number of toxic substances which are detrimental to human health [29,30].

Bag filter is one of the system to control the particulate matter and harmful material using fibrous filter. Bag filter has been used as filtration system in widely industrial field such as incineration plants because it has high collection efficiency and good economic aspects[31,32]. PPS filter is one of the most widely used material for bag filter because its thermal and chemical resistance. The melt-blown PPS fiber possesses superior thermal and chemical resistance. At high temperature, this filter material maintains excellent air permeability, and the filtration efficiency for fine particles is over 99%, which significantly improved compared to other filter.

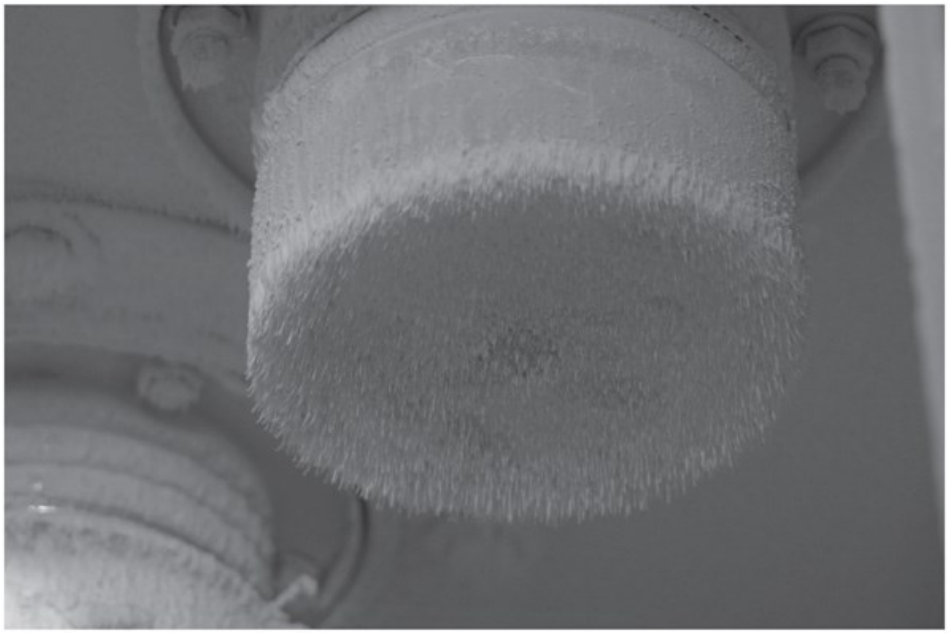

Figure 1.4 A camera image of the population of agglomerates observed in the filter housing [33].

Saleem et al. investigated the influence of operating parameters such as upper limit of pressure drop (ΔP_{max}), filtration velocity, and dust concentration on cake formation in pilot scale pulse-jet bag filter utilizing PPS and polyimide (PI) filters [33]. They found that the filtration velocity had a pronounced effect on pressure drop as well as on cake properties, cake density and specific cake resistance. Cake density and specific resistance increase with increasing filtration velocity at constant dust concentration. Specific resistance of filter media was increasing linearly while the specific resistance of filter cake was decreasing on aging. Nurnadia et al. investigated the effect of filter aids on pressure drop and permeability of PPS and PTFE filter media under various air flow rates [34]. Filter aids material is newly developed filtration aids consisting of a combination of precoating material and activated carbon. Their filter aids was formulated by mixing adsorbent activated carbon with the pre-coating material PreKot. They found that their filter aids could reduce the pressure drop and enhance the permeability across the filter cake. In all cases, the polyphenylene sulfide (PPS) filter media had a lower pressure drop compared to PTFE filter media, which indicated that PPS filter media had a better filtration performance and suitable for air filtration system. Yan-Ru et al. coated polyphenylene sulfide (PPS) fibrous felt with a conductive polymer polyaniline (PANI) via *in situ* polymerization [35]. Based on their ageing experiments indicated that PPS/PANI fiber has better heat resistance and mechanical properties than the pristine PPS fiber. The tensile strength and elongation at break also improved which the

PPS/PANI composite fiber would show longer service life. PANI layer also offered the fiber conductivity, which would be used as a pressure sensor for PPS bag filter when running.

PPS filters were utilized not only filtering substrate to get rid of the fine dust in the high temperature gas exhaust, but also catalyst supporting material for the selective catalytic reduction (SCR) to increases the filtration performances. Liu et al. fabricated MnO_x-CeO_2/PPSN by loaded MnO_x-CeO_2 catalyst to nitric acid treated PPS filter using ultrasonic method [36]. The effects of catalyst temperature, NH_3 volume fraction, O_2 volume fraction, catalyst loading on the NO removal efficiency were studied. The found that MnO_x-CeO_2/PPSN denitration efficiency showed an increasing trend with increasing reaction time. They found the best condition to reach higher NO removal efficiency when the catalytic temperature was 130 – 160 ºC, NH_3/NO ratio was slightly higher than 1 and O_2 volume fraction was about 5%. The NO removal efficiency increased with increasing catalyst loading. Zheng et al. uniformly decorated MnO_2 catalyst on the surface of PPS filter felt by a polypyrrole (PPy)-assisted method to fabricated catalytic filter felt for the removal of NO_x from flue gas [37]. The high adhesive strength between MnO_2/PPy nanocoating and the PPS filter felt contributed to the greater than 70% NO conversion obtained when using the catalytic filter felt. A too high or too low a concentration of $KMnO_4$ was unsuitable for the preparation of a highly efficient catalytic filter felt. The catalytic filter felt prepared using a highly acidic $KMnO_4$ solution showed only weak adhesion between the MnO_2/PPy nanocoating and the PPS filter fiber. Yang et al. then prepared catalytic filter by coating PPS filter media using Mn–La–Ce–Ni–O_x catalysts [38]. They tend investigated the influencing factors on low temperature denitration performance of catalytic filters applied for cement kiln. Their results showed that the catalytic filter had highly removal efficiency in a temperature range of 100 – 200 ºC and had the maximum value at 200 ºC. NH_3/NO molar ratio was also significant for removal efficiency of catalytic filter and NH_3/NO = 1 was the best value. Even in low concentration of oxygen 4 – 5 % in the flue gas, removal of NO by the developed catalyst loaded PPS filter media was sufficiently high. They also poisoned the applied catalyst of using Mn–La–Ce–Ni–O_x loaded on PPS filter media and compared to Mn-based catalyst. The removal efficiency of catalytic filter media still above 85% at reaction time 200 ºC and concentration of 300 ppm. Their results suggested that Mn–La–Ce–Ni–O_x/PPS catalytic filter was promising to achieve the expectation of simultaneously removing particulate and NO_x for cement kiln. Zheng fabricated Mn–CeO_x/PPS catalytic for denitration filter materials[39]. The activity test were evaluated in a fixed-bed quartz reactor

with the gas composition of 440 ppm NH_3, 440 ppm NO, and 5% O_2. Their result showed that the 0.4, 0.6, and 0.8 Mn–CeO_x/PPS denitration filter materials possessed outstanding denitration activity in test temperature (80 – 180 ºC). The denitration activity of 0.8 Mn–CeO_x/PPS is optimum in the test temperature and could achieve 100% NO conversion at 140 ºC. However, the 0.6 Mn–CeO_x/PPS sample exhibits the optimal low-temperature denitration activity, which was benefited from its good low-temperature reducibility, weak crystallinity, and highly dispersed properties. Chen et al. also loaded Mn and Ce oxides onto the PPS needle-punching fibrous felts (NPFF) to remove the fine dust[40]. Mn and Ce oxides were used as catalyst for selective catalytic reduction of NO_x with NH_3. They employed two different pretreatment methods: i.e., sodium alginate (SA) deposition and plasma treatment, to modify the PPS NPFF before the traditional impregnation and thermal treatment processes during the catalyst loading. Their results showed that both two pretreatment methods were afforded the PPS NPFF with the enhanced loading rate and stability of Mn/Ce oxides. Both pretreatments also presented excellent dust-removal properties and the filtration efficiency could reach 100% when the particle size of the fine particulates was above 4 μm. Ju et al. used PPS needle punching fibrous felt (NPFF) as catalyst-supporting material to load MnO_2 catalyst for selective catalytic reduction (SCR) of NO_x with NH_3 using an in-situ deposited method [41]. They low-temperature plasma treatment was used to pretreat PPS NPFFs and investigated how the pretreatment method influences the loading rate and stability of MnO_2 catalysts. Their results showed that the PPS/MnO_2 NPFFs prepared by combination of plasma pretreatment and in-situ deposition exhibited significantly higher NO_x reduction activities compared with those without plasma pretreatment. Plasma pretreatment was demonstrated to effectively improve the load rate and fastness of MnO_2 catalyst on PPS NPFFs. All the PPS/MnO_2 NPFFs presented obviously enhanced dust removal performance than the pure PPS NPFFs. Recently, Su et al. prepared sulfur-doped porous carbon materials from waste polyphenylene sulfide for efficient adsorption removal of Cd^{2+} from wastewater [42]. Their result shown that the porous material prepared at 450 ºC have the best adsorption performance of cadmium ion. When the concentration of cadmium ion was 250 ppm, the removal cadmium was 98.74% under the optimal adsorption conditions. They found that the number of acid groups and the sulfur content of the materials had a close relationship with the removal of cadmium.

1.3.2 Application in oil-water separation

The separation of a mixture of oil and water has been attracting widely attention worldwide because of a growing problem of water pollutions resulting from discharging of the industrial oily wastewaters (e.g., automotive, aviation, mechanical, and petrochemical industries) which seriously threaten human health and the ecological environment security[43–45]. Several conventional approaches have been put forward to address this problem, such as centrifuges, chemical demulsifies, magnetic separations, oil absorbing material and bioremediation[46–49]. However, some challenge including a complex operation process, high energy cost, low separation efficiency and emitting secondary pollutions. Alternatively, the membrane separation technique based on microfiltration membrane (MF) or ultrafiltration membrane (UF) has been used to be an effective strategy with easy operation process, relatively low cost and higher efficiency[50,51].

PPS fiber attract widely attention due to its properties including wettability, chemical resistance, separation flux and separation efficiency [52]. Wettability and chemical behavior are crucial factors both for super hydrophilic and super hydrophobic separation membrane [53,54]. Huang et al. prepared a superhydrophobic and super oleophilic PPS microfiber membrane by a simple and effective spray-coating method [55]. They successfully created superhydrophobic PPS microfiber membrane possessed good resistance to acid, alkali, and salt solutions. Importantly, their membrane was effective for separating a wide range of oil/water mixtures by gravity and could still retain high oil flux and separation efficiency even after many cycles. They then modified their superhydrophobic PPS membrane by added chitosan (CTS) [56]. They fabricated a superhydrophilic and underwater superoleophobic microfiber membrane with high porosity and diminutive pore size by applying a simple dip-coating following by a hot-pressing approach. The CTS/PPS microfiber membrane were displayed superior performance for separating oil-in-water both for surfactant-free emulsions (SFEs) and surface-stabilized emulsions (SSEs). In addition, the excellent antifouling performance and significant antibacterial activity endowed the membrane with robust performance for long-term separation. Qin et al. prepared polytetrafluoroethylene-polyphenylene sulfide composite by a simple layered transitional spray-plasticizing method on a stainless-steel mesh [57]. Their mesh showed both super-hydrophobic and super-oleophilic properties with a contact angle of 156.3º for water and close to 0º for diesel and kerosene. An oil-water separator with six stages was designed with the mesh film as the separation element. The oil removal rate of their oil-water separator

reached about 99%. PPS improved the adhesive force and hardness of film effectively. Wang prepared super-amphiphobic PPS/PTFE coating by a simple spraying technique [58]. The contact angles of water, crude oil and oilfield produced water on PPS/PTFE coating were 172º, 151º, and 168º, respectively, indicating excellent superamphiphobic properties. The wear rate of the superamphiphobic PPS/PTFE coating in oilfield produced water was lower than that of pure PPS and commercial coating, showing outstanding wear resistance. Yang et al. Fabricated a PPS porous membrane with a rough concave topographic via thermally induced phase separation (TIPS) process [59]. They successfully prepared a PPS membrane with an excellent superoleophilicity and a highly under oil superhydrophobicity, which made it capable for separating the surfactant stabilized emulsions, especially of some strong polar oil emulsions. The purities of all oils after separation were above 99.97% with a high flux, implying its high separation efficiency. Gao et al. fabricated superhydrophilic PPS membrane via modifying the PPS membrane by nitric acid, and –S–, $–SO_2–$, C=O, $–NH_2$, and $–NO_2$ hydrophilic groups were introduced onto the surface of membrane without change its texture to improve the hydrophilicity of PPS membrane [60]. Their result showed that PPS-50 membrane was superhydrophilic with the contact angle at 0º, and its pure water flux achieves at 154.95 $L/m^2 \cdot h$. For the separation of oil in water emulsions, the interception of the supper surface of membrane can effectively intercept the oil drops with the separation efficiencies above 95.0%. For the separation efficiency of chlorobenzene/water emulsion achieves at 98.98%. Their membrane could effectively separate oil-in-water emulsions with high separation efficiency under the effect of gravity conditions and possesses great cycle performance.

1.4 Simulation of filter media

Numerical simulations are a cost-cutting and useful tools for investigating fluid motion within a porous material. In the numerical simulations, the motion of fluid within a porous material can be easily observed, and various parameters can be independently evaluated. Over the past few decades, a number of numerical studies involving porous materials such microfiltration, air filtration, and oil-in-water coalescence have been increased.

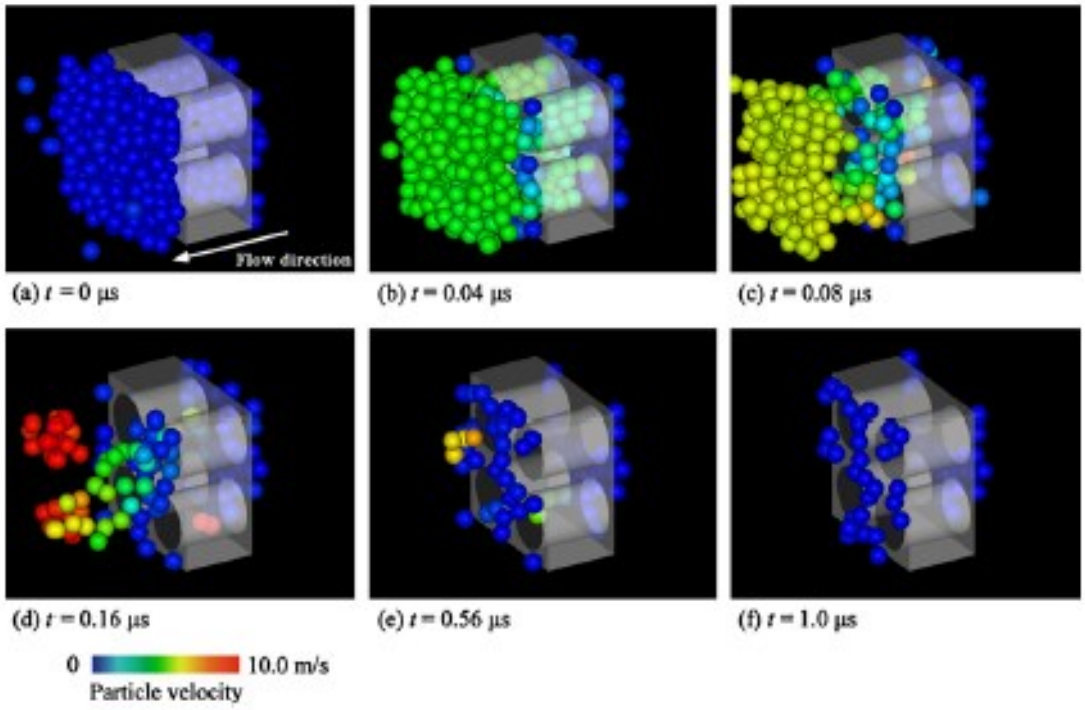

Figure 1.5 Snapshots of backwash operation for 1 μs. [57]

Ando et. al., carried out simulations of pressure-driven dead-end microfiltration with a backwash operation [61]. Their simulation was performed using Structure of Nano Particles (SNAP) which was developed by Fujita et al. [62,63]. This model is based on the discrete element method (DEM) [64] for particle motions and computational fluid dynamics (CFD) for solvent flow and considers the particle-particle and particle-membrane physiochemical interaction and hydrodynamics interactions between particle motions and fluid flow. They numerically modeled membranes with regularly spaced straight pores, which are assumed to be track-etched pores. They found there are two modes for particle fouling: one is that initially particles fill the pore and form a cake layer on the surface of membrane, and another is that particles are accumulated on the surface of the membrane without filling the pore and a cake layer grows across the entire filtration. After the backwash operation, the particles remaining on the membrane decrease the effective pore area and cause a charge in fouling conditions from pore blockage to cake formation. Ishigami et al. simulated permeation of dispersed particles through a pore in dead-end constant flux microfiltration [65]. They investigated the effects of fluid and particle motions on transmembrane pressure behavior during dead-end constant flux filtration using two-way coupled scheme combining DEM and direct numerical simulation (DNS) in two-dimensional simulation. The transmembrane

pressure increases with increasing volume fraction of the feedwater because of an increase in the number of particles inside pore.

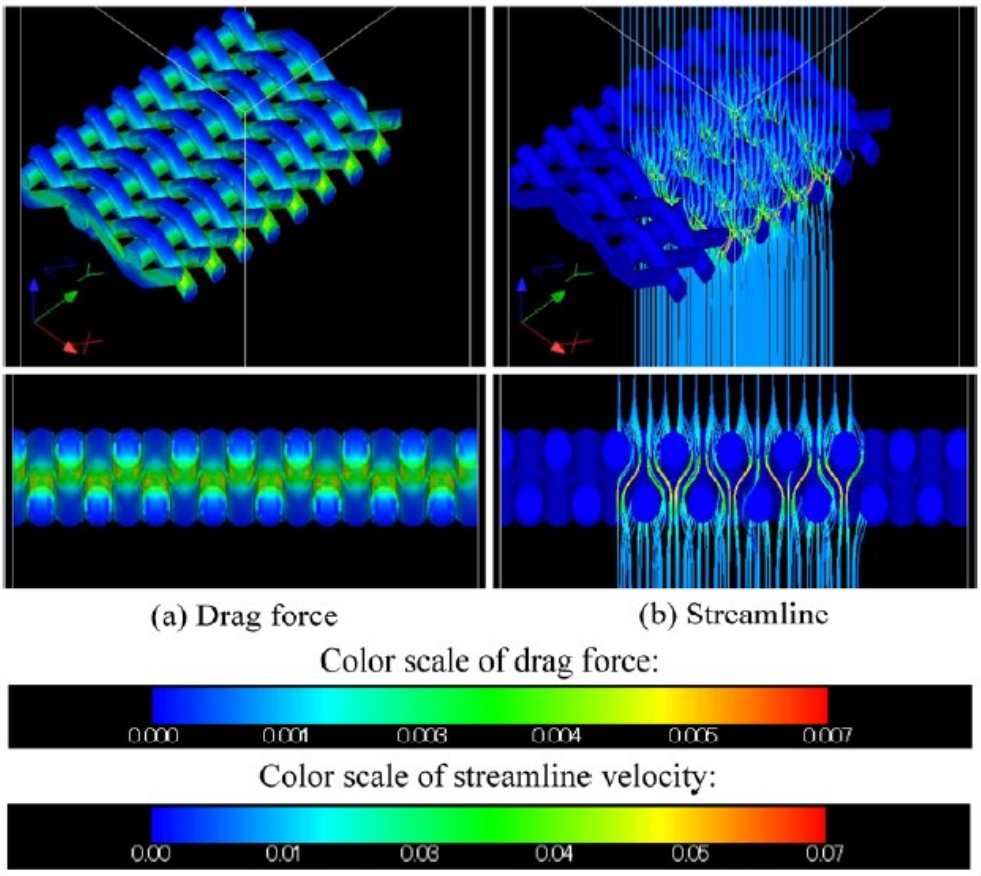

Figure 1.6 Flow state around a plain Dutch weave mesh[62]

Yoshida et al. investigated the effect of aperture structure of Dutch weave mesh on flow resistivity [66]. They proposed a calculation model for estimating the aperture size of a Plain Dutch weave and twilled Dutch weave meshes. Their simulation results showed that drag force increased at the inside aperture with different peak for plain Dutch weave mesh and twilled Dutch weave mesh. The also applied the Kozeny-Carman equation to represent the flow resistivity and derived an equation for estimating the pressure drop of the filter media. The Kozeny constant of the plain Dutch weave mesh remained almost constant, while the Kozeny constant of twilled Dutch weave mesh was varied with local torsion. Akamatsu et al. simulated particle rejection by microfiltration membranes with straight cylindrical pore during pressure driven dead-end filtration [67]. They utilized mesoscale simulations with SNAP to demonstrate the effect of surface porosity and the ratio of particle diameter to pore diameter on the movement of particles and rejection behavior. Their results showed that those two parameters strongly affect particle transport and rejection properties, resulting in

two different fouling modes and flux profiles. When the surface porosity was low and ratio of particle diameter to pore diameter is large, the particles will cover the entrance at the front surface of the membrane and the cake layer was develops and flux subsequently slowly decreased. When the surface porosity was high and ratio of particle diameter to pore diameter is small, particles will pass through the pore entrance initially, but then trapped at the back surface of the membrane. The pore clogging progresses from the back towards the front surface of the membrane. Tao et al. performed the filtration performance of fiber arrays with different types of geometrical arrangements using 3D adhesive DEM-CFD coupling simulation [68]. The effect of fiber arrays were investigated by comparing parallel array and staggered array. Their results showed that the staggered array entered the clogging stage in a much shorter time than parallel arrays and had a relative low pressure drop at the same number of captured particles. The filtration efficiency of the staggered array in the initial clean filter stage also higher than parallel array which indicating that staggered array has better overall filtration. They then compared the different types of densification in the staggered array. They found that the front densified array has best filtration performance compared to back densified array and regular array.

Tao et al. also investigated the effect of adhesion on clogging of microparticles in fiber filtration [69]. A two-way multiscale time-step coupling of adhesive DEM and CFD was utilized to investigate the occurrence of clogging of microparticles in a two cylindrical fiber filtration system. The clogging was occurred due to the growth of particle chains and the lodging of particles chains bridging the two fibers. The time for particle chains to grow increases dramatically as adhesion parameter (Ad) increases, leading to the delay of clogging. The particles tend to be mainly distributed to the foreside of fibers with high Ad, which restrains the bridging of lodged particle chains and delays the clogging. Fotovati et al. have been studied the influence of fiber orientation distribution on performance of aerosol filtration media [70]. They found that the pressure drop, and submicron particle capture efficiency of a fibrous medium are independent of the in-plane fiber orientation, which mean the in-plane fiber orientation has a little effect on performance of the filter medium. On the other hand, increasing the fiber's through-plane orientation improves the performance of a filter medium when challenged with nanoparticle aerosols. The fiber's in-plane orientation becomes important when the size of the particles is comparable to that of the fibers, for example the influence of fiber's in-plane orientation with a fiber's diameter of 10 μm can be observed when the particles are greater than 1 μm. Chen et al. investigated the clogging behavior of charged microparticles using DEM-CFD simulation [71]. The effect of long-

range Coulomb repulsion on clogging is characterized in term of bulk permeability, the number of penetrating particles, particle capture efficiency, and the distribution of the local volume fraction. Their results showed that the repulsion could delayed or totally prevented the clog formation. They also found that long-range Coulomb repulsion among particles has a significant effect on particle capture only when the number of deposited particles was moderated, and a critical state was identified as a clogging – non-clogging criterion for repulsive particles. The distribution of the local volume fraction was determined mainly by short-range adhesion. With relatively strong adhesion, a loose clog would be formed which made particles easier to penetrate. Qian et al. established a 3-D mimic model of fibrous filter which could create fibrous filter which more similar with actual condition based on the stochastic control algorithm [72]. They then utilized the CFD-DEM coupled model to investigate the dust loading filtration in the created fibrous filter. The porosity of fibrous filter, face velocity and particle size were used to investigate the filtration performance. Their results showed that the filtration efficiency of fibrous media increases with the porosity, face time, and particle size in dust loading filtration. The pressure drops increases with the porosity and face velocity but decreases with the particle size. Furthermore, the pressure drop increases linearly with particle deposition mass per unit area.

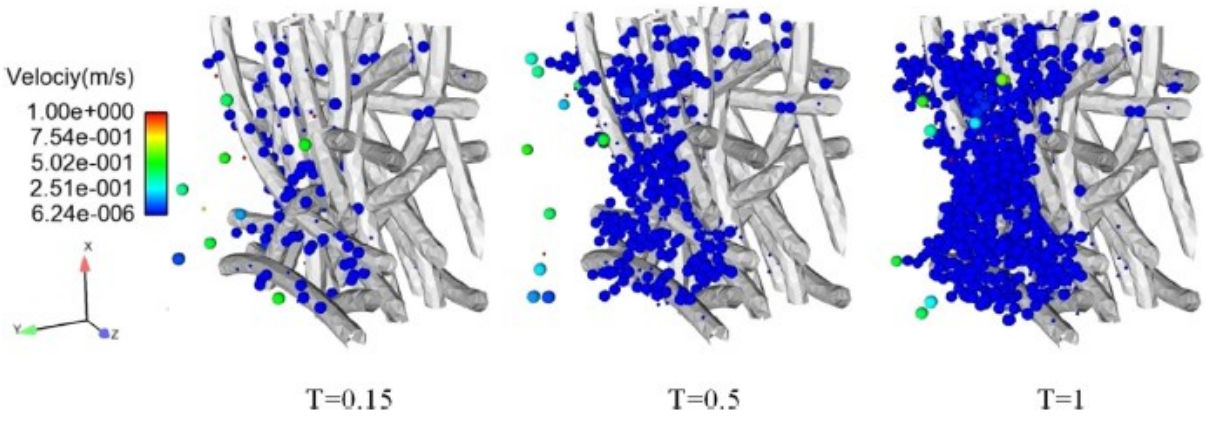

Figure 1.7 The deposition process of particles.[69]

Yue et al. established the three-dimensional random structure of fibrous filter with fiber diameter in the range of 10 to 20 μm and solid volume fraction (SVFs) in the range of 12 to 19% [73]. They used non-uniform rational B-splines (NURBS) to form curved fibers. They assumed that fiber arrangement was three-dimensionally random, and all fibers had the in-plane fiber orientation in random angle and the same diameter in each case. They successfully showing particle collision and aggregation phenomena, as well as particle detachment from fiber in their simulation. At the beginning of the filtration, particles were

captured by fibers and gradually formed particle dendrites, and the most particles were captured on the surface of the filter, but small particles were easier to penetrate fibers and dendrites. With the filtration going on, the filter was blocked by more deposited particles and dendrites, resulting in the velocity of particles at the upstream decreased and the pressure drop increased significantly with time. They also found that the filtration efficiency could be improved by increasing the solid volume fraction (SVFs), decreasing fiber diameter, and also decreasing the inlet velocity. Li et al. studied the optimization of the filtration performance of multi-fiber filter using ANSYS-Fluent with a discrete phase model (DPM) [74]. They created a simple three-dimensional model of the parallel and staggered filters using the software Gambit. All of their fibers were in perpendicular orientation to the main flow direction. Both filtration efficiency and pressure drop of the staggered filter was higher than parallel filter. They then modified the staggered filter by replacing fibers of the first layer with smaller fibers. This model could achieve higher filtration efficiency but also increasing the pressure drop. Hosseini simulated particle filtration in electro spun nanofibrous filter [75]. In this study, they presented algorithm for generating virtual 3-D fibrous media based on the randomness algorithm and simulated the pressure drop and collection efficiency of nanofibrous media in the Fluent environment with customized C++ subroutines. Their results showed good general agreement with the existing correlations, and they demonstrated that the popular correlation of Davies fails to accurately predict the pressure drop of nanofiber media. Bacchin et al. combined experiments and simulations in a microfluidic chip to investigate the influence of tortuosity and connectivity on the fouling [76]. They prepared three kinds of microchannels geometries: straight microchannels, connected microchannels, and staggered square pillars. The clogging process were varied in each geometries. With straight parallel channels at high velocity, the clogging is the consequence of arches formation at the channel entrance leading to cake formation. For lower fluid velocity, only accumulation on pillars were observed. With tortuous porous media (staggered pillars), a progressive plugging of the internal spaces occurred, and the plugging progresses toward the upstream zone and led to the blocking of the channels entrance and the formation of a dense superficial deposit later on. With connected channels, an intermediate clogging behavior was observed. Because of the initial capture of particles at the pore entrance, the distribution of the flow inside the channel was modified, then the dead connection zone between pores could be flowed. The deviation of streamline toward the connection zone could then led to the capture of particles inside the porous media as it has been observed with tortuous porous media. Lohaus et al. carried out numerical

simulations of a fouling process in a microfluidic membrane mimic using CFD-DEM numerical simulation[77]. They prepared three kinds of microfluidic membrane geometries as same as Bacchin study. Their simulation results were show good agreement with the experimental work of Bacchin et al[76]. They found that interparticle interactions have a strong effect on the clogging dynamics. Adsorbed particles could re-entrain form the inner membrane surface or they could glide downstream. The inner structure of the porous membrane could significantly affect the clogging process. In particular the re-entrainment of particle clusters and their reattaching to the inner surface could lead to a complete blockage of the flow channel.

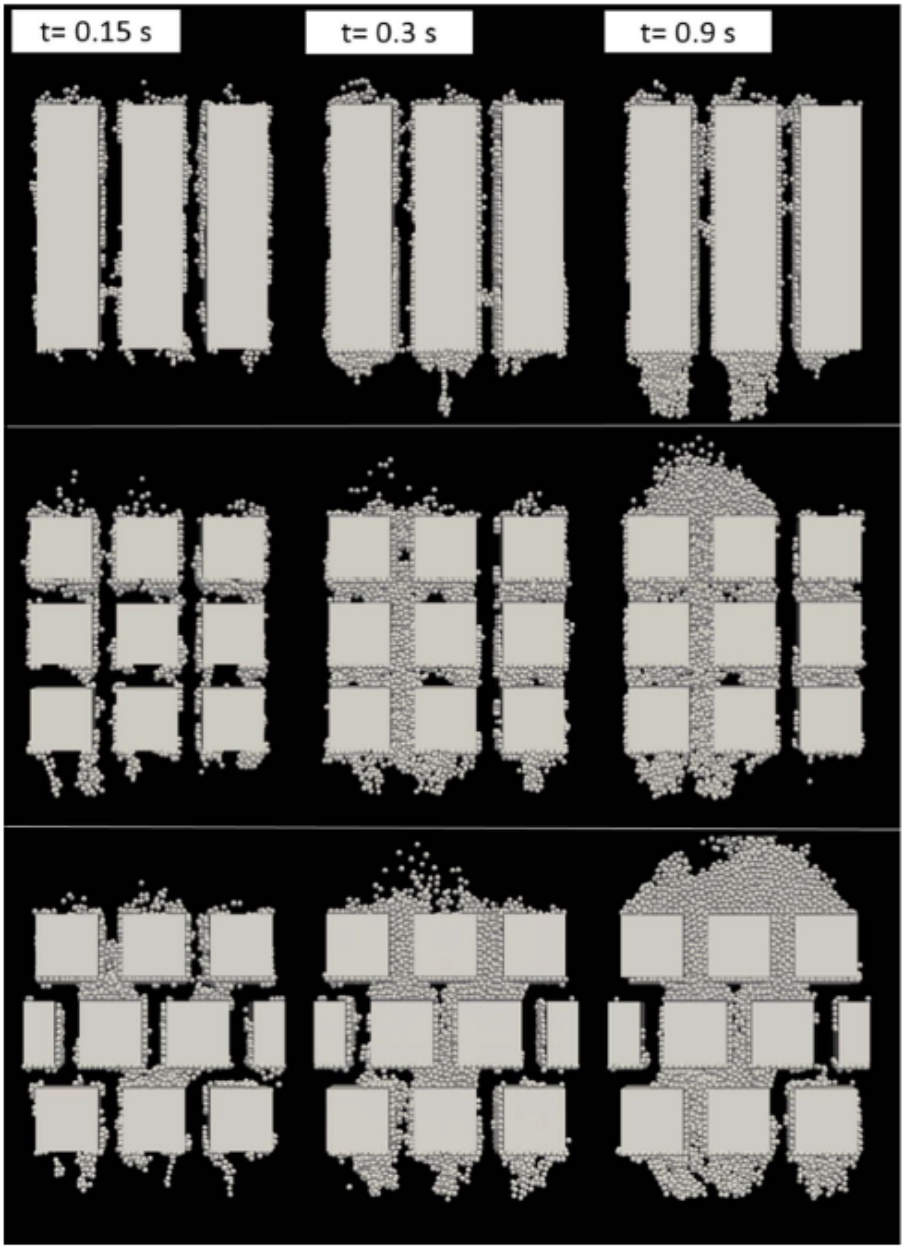

Figure 1.8 Clogging development in the staggered, connected and straight geometries[77]

Lohaus et al. continued their study by investigating the microscopic events of the membrane backwash of a clogged pore using both experiments and numerical CFD-DEM simulations [78]. The backwash was conducted with gradually increased velocities. During the backwash, they found three phenomena: detachment of individual particles, breakage of clusters and orientation of attached particle clusters/bridges in the region of lower drag, and fragmentation of a cluster and partial removal of particle agglomerates from the pore structure. The detachment of individual particles was predominantly observed at the beginning of the backwash process. They revealed that particle-membrane interactions dominantly control backwash efficiency, and the influence of particle-particle interactions was comparatively small.

For multiphase flow simulation, Kagawa et al. simulated permeation of concentrated oil-in-water emulsions through membrane pore [79]. They carried out two-dimensional numerical simulation based on the coupled level set method and volume of fluid (CLSVOF) [80] method to observe the behavior of concentrated oil-in-water (O/W) emulsions through a pore. The effects of the wettability on the pore surface, filtration flux, and pore size on the motion of concentrated O/W emulsions and demulsification efficiency were investigated. They found that the wetting of oil droplets on the membrane surface led to coalescence. The coalescence was significantly increased at the outlet of the membrane surfaces when the wettability of the membrane surface was high, and the fluid velocity was low. The wettability, filtration flux and pore size were significantly affecting the demulsification efficiency. Mino et al. was continuing the study carried out by Kagawa with simulated the permeation of O/W emulsions through a membrane with a single straight pore using the same method. But they focused on the effects of basic physical factors of O/W emulsions on the demulsification behavior [81]. The physical-chemical factors, such as the interaction of droplets and droplet-membrane and the adsorption of surfactants on the interfaces were neglected in this study. Their results showed that the oil droplets attached to membrane and mainly coalesced on the permeation-side surface of the membrane. In the case of low droplet volume fraction and the size ratio of the oil droplet and pore was also low, initially oil droplets will be passed through the membrane without attaching to its surface and the growth of the droplets was slow. After the coalescence progressed steadily on the permeation-side of the membrane surface, the oil droplets grew to form a large droplets. The maximum size of oil droplets greatly depended on the pore size because the growing droplets blocked the flow path in the case of small pore size. Mino et al. also simulated permeation of O/W emulsion through a modeled fibrous filter using 2D numerical simulation model based on the phase-field model [82]. They investigated

the effects of wettability, permeation flux, and fiber diameter on coalescing behaviors of O/W emulsions. They demonstrated that the wettability of the fiber is one of the most important factors determining coalescence mode. For hydrophobic filters, oil droplets attached to the fibers and coalesced, forming bridging structures between fibers. The bridging structures then promoted droplet coalescence unless the structures blocked the entire flow path. This coalescence-promoting effect of bridging structures was observed under the large permeation flux and large fiber diameter when the number of fibers per unit filter volume was fixed. Chen et al. numerically studied the dynamics behaviors of water-in-oil emulsified droplets on single coalescence fiber and two coalescence fiber system [83]. They investigated the motion, coalescence, and detachment behaviors of emulsified droplets on fibers surface using 3D simulation model based on phase-field method. In the single-fiber simulation, they found that the droplets will move downstream along the fiber surface under the fluid shear, and their moving velocity was proportional to the fluid speed and the contact angle of the fiber, whereas it decreased with the increase of the fibers' tilt angle and droplet size. In the case of two-fiber simulation, the emulsified droplets would directionally transport to the intersection of two angled fibers under the drive of asymmetric Laplace pressure. They also observed that the droplets could be removed from the surface of the fiber when their size was larger than a critical value. In addition, their results reveal that a fiber with better wettability could inhibit the droplet from detaching, and a large fluid speed could promote the detachment droplets. The two closely attached fiber system have a larger area of low velocity at their backside could further inhibit the detachment of the droplet compared to the single-fiber system. They concluded that the emulsified droplets tend to coalesce and grow at the intersection of fibers during the process of emulsions permeating through a coalescing fibrous filter.

Although there are many studies about filter media that have been carried out by previous researchers through both experimental and numerical studies. There are still several remaining issues that still unclear. As already mentioned in this chapter, the durability of PPS filter media against several harmful materials have been tested. However, the mechanism of the degradation of PPS filter by NO_2 gas, which was speculated to act as the main species that degrade the PPS, has not been sufficiently clarified. In the numerical simulations, despite there are many numerical simulations involving porous materials with various shapes, ranging from simple shapes to complex filter structures, both 2D and 3D, none of them use realistic geometry of the filter media which has the most important role in the filtration process. Therefore, a further method to create a realistic geometry of filter

media is necessarily needed so that the numerical studies carried out are more effective and reliable.

1.5 Objectives and outline of the dissertation

Bearing in mind the nonwoven filter media is very useful for processing harmful materials in many industries, we aimed to improve the performance and durability of filter media. Therefore, in this dissertation, we investigated the durability and performances of poly-phenylene sulfide fibrous filter media. At first, we performed the durability test of PPS nonwoven filter media against various concentration of NO_2 gas at high temperature condition. Second, we proposed a method to create complex geometry of fibrous filter using numerical simulation. Permeation of air and particles through realistic fibrous filter were carried out. Several parameters such as fiber orientation and porosity of the filter have been investigated to find the best condition to improve the performance of the filter media.

At first, we investigate the effect of NO_2 gas at high temperature on the degradation of PPS nonwoven bag filter media, as described later in **Chapter 2**. The durability of the PPS fabric filter was examined using "Test method for evaluating the degradation of characteristics of cleanable filter media" which specified in ISO16891:2016. The exposure time were varied to evaluate the degradation of the PPS filter. We proposed a novel model to estimate the change in concentration of NO_2 in the exhausted gas and the tensile strength of PPS filter based on the chemical reaction between PPS and NO_2 gas with the assumption that no structural change of the fiber packed bed occurred.

Chapter 3 describes the direct numerical simulation and experimental validation of flow resistivity of nonwoven fabric filter. We proposed a filter image processing method to construct a realistic geometry of fibrous filter utilizing X-ray computed tomography (CT) images. In this study, commercial PPS and PI nonwoven fabric filters were utilized. The simulation of single-phase flow through realistic geometry of fibrous filter was performed. An experiment was performed to measure the pressure drop across the fibrous filter. Then, we compared the simulated pressure drop with the experimental results and existing empirical equations proposed by previous researchers to validate our method. Based on the simulation results, we calculated the permeability and the Kozeny constant of the fibrous filter using Darcy's law and the Kozeny-Carman equation to investigate the flow resistivity during permeation of a gas though PPS and PI filters.

In the **Chapter 4**, we propose a new method to create a signed distance function (SDF) from the microstructure of an actual bag filter obtained from X-ray CT images by utilizing

a phase-field model and a level set method to calculate contact force between particles and filter. To demonstrate our simulation method, a direct numerical simulation of the permeation of particles through the realistic microstructure created from X-ray CT images of the PPS filter were performed. The effect of fiber orientation and filter porosity were studied to analyze the permeation behavior of particles through PPS filter.

Chapter 5 contains the summary of all chapters and the guideline for further investigation.

References

[1] World Health Organization, WHO methods and data sources for country-level causes of death 2000-2012, Global Health Estimates Technical Paper WHO/HIS/HSI/GHE/2014.7. (2014). https://www.who.int/healthinfo/global_burden_disease/GlobalCOD_method_2000_2012.pdf.

[2] World Health Organization, Burden of disease from the joint effects of Household and Ambient Air Pollution for 2012, WHO Technical Report. (2012). https://www.who.int/phe/health_topics/outdoorair/databases/AP_jointeffect_BoD_results_March2014.pdf.

[3] G. Yang, Y. Wang, Y. Zeng, G.F. Gao, X. Liang, M. Zhou, X. Wan, S. Yu, Y. Jiang, M. Naghavi, T. Vos, H. Wang, A.D. Lopez, C.J.L. Murray, Rapid health transition in China, 1990-2010: Findings from the Global Burden of disease study 2010, Lancet. 381 (2013) 1987–2015. https://doi.org/10.1016/S0140-6736(13)61097-1.

[4] C.W. Purnomo, W. Budhijanto, M. Alfisyah, Triyono, Improvement of cement plant dust emission by bag filter system, IOP Conf. Ser. Mater. Sci. Eng. 316 (2018). https://doi.org/10.1088/1757-899X/316/1/012031.

[5] R. Mead-Hunter, A.J.C. King, B.J. Mullins, Aerosol-mist coalescing filters - A review, Sep. Purif. Technol. 133 (2014) 484–506. https://doi.org/10.1016/j.seppur.2014.06.057.

[6] S. Abishek, A.J.C. King, R. Mead-Hunter, V. Golkarfard, W. Heikamp, B.J. Mullins, Generation and validation of virtual nonwoven, foam and knitted filter (separator/coalescer) geometries for CFD simulations, Sep. Purif. Technol. 188 (2017) 493–507. https://doi.org/10.1016/j.seppur.2017.07.052.

[7] E. Gregor, Primer on nonwoven fabric filtration, Textitle World. (2009).

https://www.textileworld.com/textile-world/nonwovens-technical-textiles/2009/03/primer-on-nonwoven-fabric-filtration/.

[8] Y.F. Wang, A.S. Hay, A facile synthesis and the polymerization of macrocyclic 1,4-phenylene sulfide (PPS) oligomers, Macromolecules. 29 (1996) 5050–5053. https://doi.org/10.1021/ma9602740.

[9] A.S. Rahate, K.R. Nemade, S.A. Waghuley, Polyphenylene sulfide (PPS): State of the art and applications, Rev. Chem. Eng. 29 (2013) 471–489. https://doi.org/10.1515/revce-2012-0021.

[10] J. Seppälä, M. Heino, C. Kapanen, Injection-moulded blends of a thermotropic liquid crystalline polymer with polyethylene terephthalate, polypropylene, and polyphenylene sulfide, J. Appl. Polym. Sci. 44 (1992) 1051–1060. https://doi.org/10.1002/app.1992.070440614.

[11] D. Lu, Y.W. Mai, R.K.Y. Li, L. Ye, Impact strength and crystallization behavior of Nano-SiO x/poly(phenylene sulfide) (PPS) composites with heat-treated PPS, Macromol. Mater. Eng. 288 (2003) 693–698. https://doi.org/10.1002/mame.200300088.

[12] P. Zuo, R.C. Benevides, M.A. Laribi, J. Fitoussi, M. Shirinbayan, F. Bakir, A. Tcharkhtchi, Multi-scale analysis of the effect of loading conditions on monotonic and fatigue behavior of a glass fiber reinforced polyphenylene sulfide (PPS) composite, Compos. Part B Eng. 145 (2018) 173–181. https://doi.org/10.1016/j.compositesb.2018.03.031.

[13] W. Koch, W. Heitz, Models and mechanism of the formation of poly(thio-1,4-phenylene), Die Makromol. Chemie. 184 (1983) 779–792. https://doi.org/10.1002/macp.1983.021840412.

[14] G.F.L. Ehlers, K.R. Fisch, W.R. Powell, Thermal degradation of polymers with phenylene units in the chain. IV. Aromatic polyamides and polyimides, J. Polym. Sci. Part A-1 Polym. Chem. 8 (1970) 3511–3527. https://doi.org/10.1002/pol.1970.150081213.

[15] R.L. Elsenbaumer, L.W. Shacklette, J.W. Sowa, R.H. Baughman, Electrically Conducting Polyaromatic Sulfides., Mol. Cryst. Liq. Cryst. 83 (1982) 229–238. https://doi.org/10.1080/00268948208072172.

[16] F. Bertinelli, P.C. Bizzarri, C. Della Casa, S. Saltini, Poly(m-phenylene disulfide): Antimony pentafluoride doping and infrared spectroscopy, J. Polym. Sci. Part B

Polym. Phys. 24 (1986) 2197–2208. https://doi.org/10.1002/polb.1986.090241004.

[17] L.D. Kispert, L.A. Files, J.E. Frommer, L.W. Shacklette, R.R. Chance, An EPR study of the reaction between poly(p -phenylene sulfide) and electron-acceptor dopants, J. Chem. Phys. 78 (1983) 4858–4861. https://doi.org/10.1063/1.445395.

[18] W.K. Son, H.K. Sang, S.G. Park, Synthesis and exchange properties of sulfonated poly(phenylene sulfide) with alkali metal ions in organic solvents, Bull. Korean Chem. Soc. 22 (2001) 53–58.

[19] W. Tanthapanichakoon, M. Furuuchi, K. hei Nitta, M. Hata, S. Endoh, Y. Otani, Degradation of semi-crystalline PPS bag-filter materials by NO and O2 at high temperature, Polym. Degrad. Stab. 91 (2006) 1637–1644. https://doi.org/10.1016/j.polymdegradstab.2005.12.008.

[20] W. Tanthapanichakoon, M. Hata, K. hei Nitta, M. Furuuchi, Y. Otani, Mechanical degradation of filter polymer materials: Polyphenylene sulfide, Polym. Degrad. Stab. 91 (2006) 2614–2621. https://doi.org/10.1016/j.polymdegradstab.2006.05.005.

[21] W. Tanthapanichakoon, M. Furuuchi, K.-H. Nitta, M. Hata, Y. Otani, Degradation of bag-filter non-woven fabrics by nitric oxide at high temperatures, Adv. Powder Technol. 18 (2007) 349–354. https://doi.org/10.1163/156855207780860264.

[22] D. Chang, J. Liu, N. Mao, H. Zhang, B. Chen, Study on the Effect of SO2 in Flue Gas on PPS Filter Media Used in the Baghouse, in: 2010 Asia-Pacific Power Energy Eng. Conf., IEEE, 2010.

[23] N. Mao, J.X. Liu, X. Sun, Effect of SO_2 on PPS by a New Durability Testing Method for Filter Media, Appl. Mech. Mater. 71–78 (2011) 3052–3055. https://doi.org/10.4028/www.scientific.net/AMM.71-78.3052.

[24] N. Mao, J. Liu, X. Sun, Effect of NO on PPS by a new durability testing method for filter media, Appl. Mech. Mater. 71–78 (2011) 1079–1082. https://doi.org/10.4028/www.scientific.net/AMM.71-78.1079.

[25] N. Mao, D.Q. Chang, J.X. Liu, X. Sun, Experimental study on the durability performance of PPS filter media, Appl. Mech. Mater. 300–301 (2013) 1077–1080. https://doi.org/10.4028/www.scientific.net/AMM.300-301.1077.

[26] W. Cai, G. Hu, Oxidation degradation of polyphenylene sulfide needle felt at different sulfuric acid dew point temperatures, High Perform. Polym. 27 (2015) 94–99. https://doi.org/10.1177/0954008314540311.

[27] W. Wang, X. Wu, C. Ding, X. Huang, N. Ye, Q. Yu, K. Mai, Thermal aging

performance of glass fiber/polyphenylene sulfide composites in high temperature, J. Appl. Polym. Sci. (2021) 1–10. https://doi.org/10.1002/app.50948.

[28] E.P. Petkova, D.W. Jack, N.H. Volavka-Close, P.L. Kinney, Particulate matter pollution in African cities, Air Qual. Atmos. Heal. 6 (2013) 603–614. https://doi.org/10.1007/s11869-013-0199-6.

[29] K.H. Kim, E. Kabir, S. Kabir, A review on the human health impact of airborne particulate matter, Environ. Int. 74 (2015) 136–143. https://doi.org/10.1016/j.envint.2014.10.005.

[30] P. Hou, S. Wu, Long-term Changes in Extreme Air Pollution Meteorology and the Implications for Air Quality, Sci. Rep. 6 (2016) 1–9. https://doi.org/10.1038/srep23792.

[31] J. Steffens, J.R. Coury, Collection efficiency of fiber filters operating on the removal of nano-sized aerosol particles: I-Homogeneous fibers, Sep. Purif. Technol. 58 (2007) 99–105. https://doi.org/10.1016/j.seppur.2007.07.011.

[32] H.C. Wang, D.H. Jiang, Y. Liu, Life Problem Analysis on PPS Filter Application of Bag Dedusters in Coal-Fired Power Plants, Adv. Mater. Res. 236–238 (2011) 2464–2470. https://doi.org/10.4028/www.scientific.net/AMR.236-238.2464.

[33] M. Saleem, G. Krammer, R.U. Khan, M.S. Tahir, Influence of operating parameters on cake formation in pilot scale pulse-jet bag filter, Powder Technol. 224 (2012) 28–35. https://doi.org/10.1016/j.powtec.2012.02.016.

[34] A. Nurnadia, M. Rashid, S. Hajar, M.R. Ammar, Effect of Filter Aids on Pressure Drop and Permeability of Two Different Filter Media, Adv. Mater. Res. 1125 (2015) 245–249. https://doi.org/10.4028/www.scientific.net/amr.1125.245.

[35] Y.R. Lv, H.W. He, F.X. Chen, J. Yu, X. Ning, R. Zhou, Polyphenylene sulfide (PPS) fibrous felt coated with conductive polyaniline via in situ polymerization for smart high temperature bag-filter, Mater. Res. Express. 6 (2019). https://doi.org/10.1088/2053-1591/ab15f1.

[36] Q. Liu, Y.Y. Zheng, X. Wang, Research on de-NO by low-temperature SCR based on MnOx-CeO2/PPSN, Ranliao Huaxue Xuebao/Journal Fuel Chem. Technol. 40 (2012) 452–455. https://doi.org/10.1016/s1872-5813(12)60020-6.

[37] Y. Zheng, Y. Zhang, X. Wang, Z. Xu, X. Liu, X. Lu, Z. Fan, MnO2 catalysts uniformly decorated on polyphenylene sulfide filter felt by a polypyrrole-assisted method for use in the selective catalytic reduction of NO with NH3, RSC Adv. 4

(2014) 59242–59247. https://doi.org/10.1039/c4ra07168a.

[38] B. Yang, D.H. Zheng, Y.S. Shen, Y.S. Qiu, B. Li, Y.W. Zeng, S.B. Shen, S.M. Zhu, Influencing factors on low-temperature deNOx performance of Mn-La-Ce-Ni-Ox/PPS catalytic filters applied for cement kiln, J. Ind. Eng. Chem. 24 (2015) 148–152. https://doi.org/10.1016/j.jiec.2014.09.022.

[39] W. Zheng, Y. Zheng, J. Chen, Y. Zhang, Fabrication of Mn-CeOx/polyphenylene sulfide functional composites by an in situ reaction for low-Temperature NO reduction with NH3, MRS Commun. 7 (2017) 933–937. https://doi.org/10.1557/mrc.2017.120.

[40] Y. Chen, H. He, S. Wu, X. Ning, F. Chen, Y. Lv, J. Yu, R. Zhou, Mn/Ce oxides decorated polyphenylene sulfide needle-punching fibrous felts for dust removal and denitration application, Polymers (Basel). 12 (2020) 1–13. https://doi.org/10.3390/polym12010168.

[41] L. Ju, F. Li, R. Zhou, H. He, F. Chen, Q. Liu, X. Ning, G. Qi, C. Song, Manganese Oxides Decorated Polyphenylene Sulfide Needle-punching Fibrous Felts: A New Composite for Dust Removal and Denitration Application, Fibers Polym. 0 (2021) 1–8. https://doi.org/10.1007/s12221-021-1153-0.

[42] W. Su, W. Tang, Z. Zhu, Y. Liu, Sulfur-doped porous carbon derived from waste polyphenylene sulfide for efficient adsorption removal of Cd2+from simulated wastewater, J. Phys. Conf. Ser. 1639 (2020). https://doi.org/10.1088/1742-6596/1639/1/012094.

[43] T.R. Annunciado, T.H.D. Sydenstricker, S.C. Amico, Experimental investigation of various vegetable fibers as sorbent materials for oil spills, Mar. Pollut. Bull. 50 (2005) 1340–1346. https://doi.org/10.1016/j.marpolbul.2005.04.043.

[44] H. Zhu, S. Qiu, W. Jiang, D. Wu, C. Zhang, Evaluation of electrospun polyvinyl chloride/polystyrene fibers as sorbent materials for oil spill cleanup, Environ. Sci. Technol. 45 (2011) 4527–4531. https://doi.org/10.1021/es2002343.

[45] J. Lin, Y. Shang, B. Ding, J. Yang, J. Yu, S.S. Al-Deyab, Nanoporous polystyrene fibers for oil spill cleanup, Mar. Pollut. Bull. 64 (2012) 347–352. https://doi.org/10.1016/j.marpolbul.2011.11.002.

[46] M.O. Adebajo, R.L. Frost, J.T. Kloprogge, O. Carmody, S. Kokot, Porous Materials for Oil Spill Cleanup: A Review of Synthesis and Absorbing Properties, J. Porous Mater. 10 (2003) 159–170. https://doi.org/10.1023/A:1027484117065.

[47] A. Bayat, S.F. Aghamiri, A. Moheb, G.R. Vakili-Nezhaad, Oil spill cleanup from sea water by sorbent materials, Chem. Eng. Technol. 28 (2005) 1525–1528. https://doi.org/10.1002/ceat.200407083.

[48] W. Lei, D. Portehault, D. Liu, S. Qin, Y. Chen, Porous boron nitride nanosheets for effective water cleaning, Nat. Commun. 4 (2013) 1–7. https://doi.org/10.1038/ncomms2818.

[49] J.B. Fan, Y. Song, S. Wang, J. Meng, G. Yang, X. Guo, L. Feng, L. Jiang, Directly Coating Hydrogel on Filter Paper for Effective Oil-Water Separation in Highly Acidic, Alkaline, and Salty Environment, Adv. Funct. Mater. 25 (2015) 5368–5375. https://doi.org/10.1002/adfm.201501066.

[50] F.L. Hua, Y.F. Tsang, Y.J. Wang, S.Y. Chan, H. Chua, S.N. Sin, Performance study of ceramic microfiltration membrane for oily wastewater treatment, Chem. Eng. J. 128 (2007) 169–175. https://doi.org/10.1016/j.cej.2006.10.017.

[51] S. Zhang, F. Lu, L. Tao, N. Liu, C. Gao, L. Feng, Y. Wei, Bio-inspired anti-oil-fouling chitosan-coated mesh for oil/water separation suitable for broad ph range and hyper-saline environments, ACS Appl. Mater. Interfaces. 5 (2013) 11971–11976. https://doi.org/10.1021/am403203q.

[52] Y. Yu, S. Xiong, H. Huang, L. Zhao, K. Nie, S. Chen, J. Xu, X. Yin, H. Wang, L. Wang, Fabrication and application of poly (phenylene sulfide) ultrafine fiber, React. Funct. Polym. 150 (2020) 104539. https://doi.org/10.1016/j.reactfunctpolym.2020.104539.

[53] H.C. Yang, K.J. Liao, H. Huang, Q.Y. Wu, L.S. Wan, Z.K. Xu, Mussel-inspired modification of a polymer membrane for ultra-high water permeability and oil-in-water emulsion separation, J. Mater. Chem. A. 2 (2014) 10225–10230. https://doi.org/10.1039/c4ta00143e.

[54] Z.X. Wang, C.H. Lau, N.Q. Zhang, Y.P. Bai, L. Shao, Mussel-inspired tailoring of membrane wettability for harsh water treatment, J. Mater. Chem. A. 3 (2015) 2650–2657. https://doi.org/10.1039/c4ta05970k.

[55] H. Huang, M. Liu, Y. Li, Y. Yu, X. Yin, J. Wu, S. Chen, J. Xu, L. Wang, H. Wang, Polyphenylene sulfide microfiber membrane with superhydrophobicity and superoleophilicity for oil/water separation, J. Mater. Sci. 53 (2018) 13243–13252. https://doi.org/10.1007/s10853-018-2546-3.

[56] H. Huang, Y. Li, L. Zhao, Y. Yu, J. Xu, X. Yin, S. Chen, J. Wu, H. Yue, H. Wang, L.

Wang, A facile fabrication of chitosan modified PPS-based microfiber membrane for effective antibacterial activity and oil-in-water emulsion separation, Cellulose. 26 (2019) 2599–2611. https://doi.org/10.1007/s10570-019-02274-7.

[57] F. Qin, Z. Yu, X. Fang, X. Liu, X. Sun, A novel composite coating mesh film for oil-water separation, Front. Chem. Eng. China. 3 (2009) 112–118. https://doi.org/10.1007/s11705-009-0149-x.

[58] H. Wang, L. Yan, D. Gao, D. Liu, C. Wang, L. Sun, Y. Zhu, Tribological properties of superamphiphobic PPS/PTFE composite coating in the oilfield produced water, Wear. 319 (2014) 62–68. https://doi.org/10.1016/j.wear.2014.07.012.

[59] C. Yang, N. Han, W. Wang, W. Zhang, C. Han, Z. Cui, X. Zhang, Fabrication of a PPS Microporous Membrane for Efficient Water-in-Oil Emulsion Separation, Langmuir. 34 (2018) 10580–10590. https://doi.org/10.1021/acs.langmuir.8b02393.

[60] Y. Gao, Z. Li, B. Cheng, K. Su, Superhydrophilic poly(p-phenylene sulfide) membrane preparation with acid/alkali solution resistance and its usage in oil/water separation, Sep. Purif. Technol. 192 (2018) 262–270. https://doi.org/10.1016/j.seppur.2017.09.065.

[61] T. Ando, K. Akamatsu, S. ichi Nakao, M. Fujita, Simulation of fouling and backwash dynamics in dead-end microfiltration: Effect of pore size, J. Memb. Sci. 392–393 (2012) 48–57. https://doi.org/10.1016/j.memsci.2011.11.051.

[62] M. Fujita, Y. Yamaguchi, Multiscale simulation method for self-organization of nanoparticles in dense suspension, J. Comput. Phys. 223 (2007) 108–120. https://doi.org/10.1016/j.jcp.2006.09.001.

[63] M. Fujita, Y. Yamaguchi, Simulation model of concentrated colloidal nanoparticulate flows, Phys. Rev. E - Stat. Nonlinear, Soft Matter Phys. 77 (2008) 1–14. https://doi.org/10.1103/PhysRevE.77.026706.

[64] P.A. Cundall, O.D.L. Strack, A discrete numerical model for granular assemblies, Géotechnique. 29 (1979) 47–65. https://doi.org/10.1680/geot.1979.29.1.47.

[65] T. Ishigami, H. Fuse, S. Asao, D. Saeki, Y. Ohmukai, E. Kamio, H. Matsuyama, Permeation of Dispersed Particles through a Pore and Transmembrane Pressure Behavior in Dead-End Constant-Flux Microfiltration by Two-Dimensional Direct Numerical Simulation, Ind. Eng. Chem. Res. 52 (2013) 4650–4659. https://doi.org/10.1021/ie302448x.

[66] Y. Yoshida, Y. Inoue, A. Shimosaka, Y. Shirakawa, J. Hidaka, Effect of aperture

structure of Dutch weave mesh on flow resistivity, J. Chem. Eng. Japan. 48 (2015) 730–741. https://doi.org/10.1252/jcej.14we168.

[67] K. Akamatsu, S. Kanasugi, T. Ando, O. Koike, M. Fujita, S.I. Nakao, Mesoscale simulations of particle rejection by microfiltration membranes with straight cylindrical pore during pressure-driven dead-end filtration, J. Chem. Eng. Japan. 49 (2016) 452–459. https://doi.org/10.1252/jcej.15we133.

[68] R. Tao, M. meng Yang, S. qing Li, Filtration of micro-particles within multi-fiber arrays by adhesive DEM-CFD simulation, J. Zhejiang Univ. Sci. A. 19 (2018) 34–44. https://doi.org/10.1631/jzus.A1700156.

[69] R. Tao, M. Yang, S. Li, Effect of adhesion on clogging of microparticles in fiber filtration by DEM-CFD simulation, Powder Technol. 360 (2020) 289–300. https://doi.org/10.1016/j.powtec.2019.09.083.

[70] S. Fotovati, H. Vahedi Tafreshi, B. Pourdeyhimi, Influence of fiber orientation distribution on performance of aerosol filtration media, Chem. Eng. Sci. 65 (2010) 5285–5293. https://doi.org/10.1016/j.ces.2010.06.032.

[71] S. Chen, W. Liu, S. Li, Effect of long-range electrostatic repulsion on pore clogging during microfiltration, Phys. Rev. E. 94 (2016) 1–11. https://doi.org/10.1103/PhysRevE.94.063108.

[72] F. Qian, N. Huang, J. Lu, Y. Han, CFD-DEM simulation of the filtration performance for fibrous media based on the mimic structure, Comput. Chem. Eng. 71 (2014) 478–488. https://doi.org/10.1016/j.compchemeng.2014.09.018.

[73] C. Yue, Q. Zhang, Z. Zhai, Numerical simulation of the filtration process in fibrous filters using CFD-DEM method, J. Aerosol Sci. 101 (2016) 174–187. https://doi.org/10.1016/j.jaerosci.2016.08.004.

[74] W. Li, S. Shen, H. Li, Study and optimization of the filtration performance of multi-fiber filter, Adv. Powder Technol. 27 (2016) 638–645. https://doi.org/10.1016/j.apt.2016.02.018.

[75] S.A. Hosseini, H.V. Tafreshi, 3-D simulation of particle filtration in electrospun nanofibrous filters, Powder Technol. 201 (2010) 153–160. https://doi.org/10.1016/j.powtec.2010.03.020.

[76] P. Bacchin, Q. Derekx, D. Veyret, K. Glucina, P. Moulin, Clogging of microporous channels networks: Role of connectivity and tortuosity, Microfluid. Nanofluidics. 17 (2014) 85–96. https://doi.org/10.1007/s10404-013-1288-4.

[77] J. Lohaus, Y.M. Perez, M. Wessling, What are the microscopic events of colloidal membrane fouling?, J. Memb. Sci. 553 (2018) 90–98. https://doi.org/10.1016/j.memsci.2018.02.023.

[78] J. Lohaus, F. Stockmeier, P. Surray, J. Lölsberg, M. Wessling, What are the microscopic events during membrane backwashing?, J. Memb. Sci. 602 (2020). https://doi.org/10.1016/j.memsci.2020.117886.

[79] Y. Kagawa, T. Ishigami, K. Hayashi, H. Fuse, Y. Mino, H. Matsuyama, Permeation of concentrated oil-in-water emulsions through a membrane pore: Numerical simulation using a coupled level set and the volume-of-fluid method, Soft Matter. 10 (2014) 7985–7992. https://doi.org/10.1039/c4sm00705k.

[80] M. Sussman, E.G. Puckett, A Coupled Level Set and Volume-of-Fluid Method for Computing 3D and Axisymmetric Incompressible Two-Phase Flows, J. Comput. Phys. 162 (2000) 301–337. https://doi.org/10.1006/jcph.2000.6537.

[81] Y. Mino, Y. Kagawa, T. Ishigami, H. Matsuyama, Numerical simulation of coalescence phenomena of oil-in-water emulsions permeating through straight membrane pore, Colloids Surfaces A Physicochem. Eng. Asp. 491 (2016) 70–77. https://doi.org/10.1016/j.colsurfa.2015.11.059.

[82] Y. Mino, Y. Kagawa, H. Matsuyama, T. Ishigami, Permeation of oil-in-water emulsions through coalescing filter: Two-dimensional simulation based on phase-field model, AIChE J. 62 (2016) 2525–2532. https://doi.org/10.1002/aic.15206.

[83] C. Chen, L. Chen, D. Weng, X. Li, Z. Li, J. Wang, Simulation Study on the Dynamic Behaviors of Water-in-Oil Emulsified Droplets on Coalescing Fibers, Langmuir. 36 (2020) 14872–14880. https://doi.org/10.1021/acs.langmuir.0c02948.

Chapter 2

A continuous-flow exposure method to determine degradation of poly-phenylene sulfide non-woven bag-filter media by NO_2 gas at high temperature

2.1 Introduction

Flue gas from waste incineration facilities and coal-fired power plants are primary sources of air pollution. To control dust emission, including some harmful gases (e.g., NO_x, SO_x, dioxin and HCl), bag filter systems [1–5] have been installed in these facilities since they are more economical and effective than other dust collection systems[6,7].

Polyphenylene sulfide (PPS) has been increasingly used as a filter medium owing to its excellent chemical, thermal, and mechanical properties [8–10]. PPS nonwoven fabric is also one of the most cost-effective filter media used in processing the flue gas of waste incinerator facilities and coal-fired power plants [11]. PPS filter media can be used at high temperatures (e.g., 140 – 200 °C) and in the presence of acid gases. In general, though the service life of a PPS filter can reach several years provided that it is maintained and used properly, the degradation and deterioration of its mechanical and chemical properties progresses gradually throughout the lifetime of the filter [12,13].

Flue gas discharged from industrial plants often contains some corrosive gases (e.g., NO, NO_2, SO_2, SO_3, and Cl_2). Oxidation and acid-base corrosion are the main factors causing the degradation of PPS filters [14–16]. Therefore, effects of a single or mixture of gas components on the degradation of PPS fabric filter media have been investigated. Tanthapanichakoon et al. examined the effect of NO, and mixtures of NO and O_2 at high temperatures [17,18]. They also studied the durability of a PPS nonwoven fabric filter against several chemicals, and identified that HNO_3 caused severe degradation of the PPS filter, while remaining highly resistant against HCl and H_2SO_4 [19]. Cai and Hu investigated the oxidation degradation of PPS filter media at different sulfuric acid dew point temperatures [20]. Although the influence of several chemical species on PPS filters has been determined to a certain extent, the influence of NO_2 and SO_3 gases has not been sufficiently studied.

NO_2 gas has been speculated to act as the main species which degrades PPS fabric filters [21]. It was reported that corona discharge enhances the degradation of PPS by forming NO_2 gas. However, the effects and mechanism of NO_2 gas on the PPS filter were not sufficiently determined, since NO_2 was produced in O_2 and NO atmospheres, which can also cause deterioration of the PPS filter [22]. Furthermore, almost all investigations focus on the degradation of the filter media using batch or semi-batch types of exposure chambers, whereby the test gas does not pass through the filter media [17–19].

In this study, the durability of the PPS fabric filter media toward NO_2 gas was examined in detail with a continuous-flow type exposure chamber where the gas was forced to permeate the filter media. This method is specified in ISO16891:2016 "Test methods for evaluating the degradation of characteristics of cleanable filter media" [23]. Since this method measures the change in the gas composition discharged from the exposure chamber with time, the reaction rate between PPS and NO_2 gas can be assessed. Hence, we proposed a novel model to estimate the change in concentration of NO_2 in the exhausted gas and the tensile strength of PPS filter media based on the chemical reaction between PPS fiber and NO_2 gas with the assumption that no structural change of the fiber packed bed occurred. These findings are useful for proper utilization of PPS fabric filters in industrial settings.

2.2 Materials and methods

PPS nonwoven filter media (Toyobo, Procon®; 500 g/m^2 and 1.76 mm thickness) was used as the test material. The properties of the filter media and its fiber are listed in **Table 2-1**.

Table 2-1 Physical properties of tested PPS filter and fiber

PPS filter	Basis weight	500 g/cm^2
	Thickness	1.76 mm
	Melting point	285 ºC
PPS fiber	Diameter	15 μm
	Density	1.34 g/cm^2
	Cross-sectional shape	round

A simple exposure system was employed to investigate degradation of the filter media by an acid gas at high temperatures. NO_2 was used as the acid gas, which is among the

components contained in the flue gas from coal-fired power plants and waste incineration facilities and is thought to promote the deterioration of the filter media.

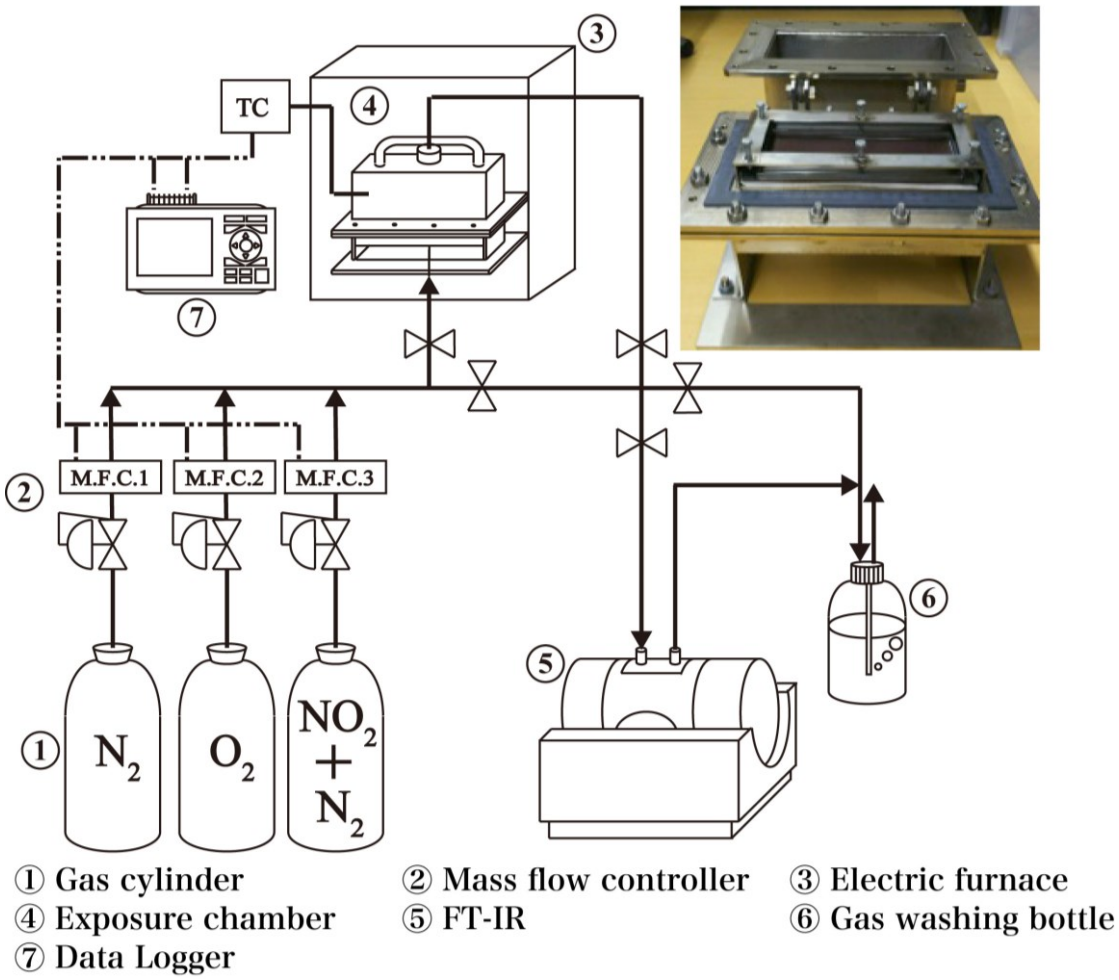

Figure 2.1 Schematic diagram of the experimental setup and photo of the exposure chamber.

Figure 2.1 shows the schematic diagram of the experimental set-up, which was constructed in accordance with ISO16891:2016 "Test methods for evaluating degradation of characteristics of cleanable filter media" [23]. This exposure system consisted of a gas supply unit, heating and exposure unit, gas analyzer unit, and exhaust gas cleaning unit. The test gases were supplied continuously to a stainless-steel exposure chamber kept at 200 °C in an electric furnace at 1.0 L/min through mass flow controllers (KOFLOC, 8500MC) from gas cylinders. The composition of the test gas was adjusted by controlling the flow rate from each gas cylinder. Test gas I contained 1000 ppm of NO_2, 10% O_2, and N_2 as a balance gas, while test gas II included 10% O_2 and 90% N_2. The gas discharged from the exposure chamber was exhausted into a draft chamber through a gas washing bottle because the acid

gas used in this experiment is harmful even at low concentrations. NO_2 concentration in the supplied and exhausted gases was measured intermittently by monitoring the infrared absorption peak at 1628 cm^{-1} by Fourier-transform infrared (FT-IR) spectroscopy (Thermo Scientific, Nicolet iS5).

Test specimens in the machine direction (MD) and transverse direction (TD) with dimensions of 250 mm × 105 mm were prepared from the filter media. The MD is the direction parallel to the direction of the movement of the fabric. The TD is also known as the cross-machine direction. To prevent direct interaction between fibers in different specimens, two pairs of MD and TD specimens alternately layered with a non-cohesive PTFE separator sheet (1.0 mm thickness) were set tightly in the exposure chamber. The test gas passed sequentially through 2 pairs of MD and TD specimens without leakage. The exposure time was varied from 50 to 200 h.

The test specimens were taken out from the exposure chamber after cooling, and then they were used for further testing and analysis. The thickness was measured by using a digital thickness gauge (TECLOCK, J type PG–15) according to JIS L1096. The specimens were cut into small pieces with dimensions of 200 mm × 25 mm to analyze the mechanical properties. The tensile test was performed by a tensile tester (Shimadzu, SBL–500K–350) for both MD and TD. Here, the tensile rate was set at 100 mm/min, and the gap between the grippers of the specimen was 100 mm. The tensile strength τ was defined as in Eq. (2-1) with the maximum load $P_{\max}$ and the specimen width W.

$$\tau = \frac{P_{\max}}{W} \tag{2-1}$$

The morphology of the specimen was observed by a field-emission scanning electron microscope (FE-SEM, Hitachi High-Technologies, S-5200). Elemental analysis was performed using a CHNS analyzer (Perkin Elmer, CHNS/O 2400II) and energy dispersive X-ray spectroscopy (EDS; Edach Japan, Genesis XM 2). Infrared absorption was measured by attenuated total reflection (ATR) FT-IR spectroscopy (Thermo Scientific, Nicolet iS5).

2.3 Results and Discussion

2.3.1 Effect on physical properties

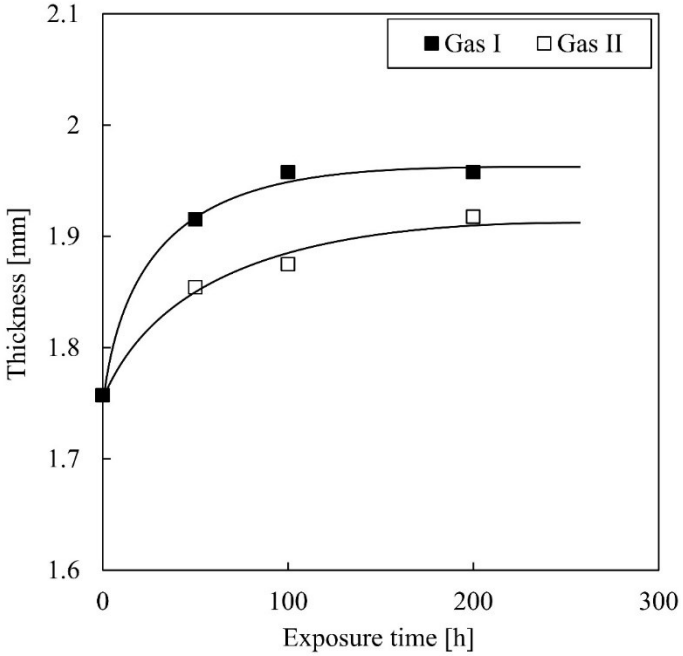

Figure 2.2 Change in the filter thickness of PPS filter media as a function of exposure time.

The physical changes of the PPS filter media, such as filter thickness, filter appearance, and tensile strength were used as the primary indicators for degradation. The filter thickness as a function of exposure time is shown in **Figure 2.2**. Both gases showed similar trends in the filter thickness, which increased to reach a constant value with increasing exposure time. However, the PPS filter exposed by Gas I was thicker than that by Gas II. These results suggest that the gaps between fibers in the filter media expanded upon exposure to NO_2 gas during the heating process.

Figure 2.3 Appearance of filter media: (a) original; (b) exposed to Gas I (NO_2 + heat) for 200 h; and (c) exposed to Gas II (heat) for 200 h.

Figure 2.3 shows the appearance of the original PPS specimen and the specimens after exposure to Gas I and Gas II for 200 h. Compared with the original specimen that is white, both exposed specimens were brown, but the specimen exposed to Gas I was much darker than that of Gas II. The difference in the appearance suggests that NO_2 gas reacted with PPS, resulting in a color change.

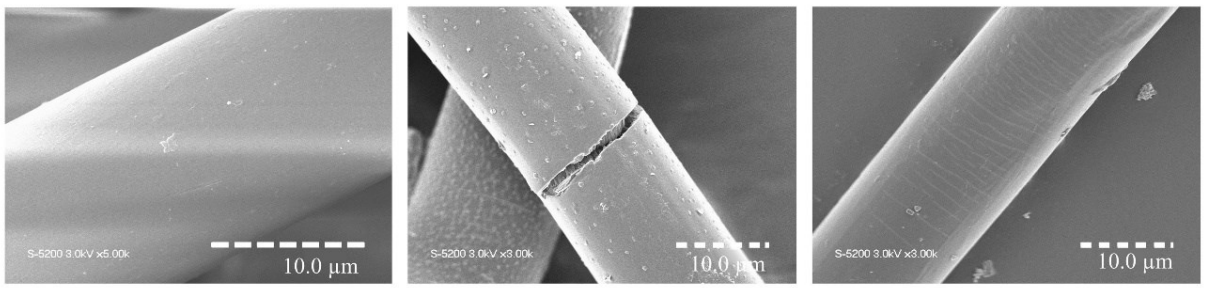

(a) (b) (c)

Figure 2.4 Morphology of PPS filter fibers: (a) original; (b) exposed to Gas I (NO_2 + heat) for 200 h; and (c) exposed to Gas II (heat).

SEM images of PPS single fibers are shown in **Figure 2.4**. The original PPS fiber is cylindrical in shape with a smooth surface. Though few scratches could be found on the surface of the PPS fiber exposed to Gas II, severe damage could be observed on the fiber

exposed to Gas I. Many protrusions cover the entire surface of the fiber with cracking and splitting, as shown in **Figure 2.4(b)**. This finding suggests that NO_2 gas enhances degradation of the filter media, since the morphological damage of filter fibers directly results in a decrease in the strength of the filter media.

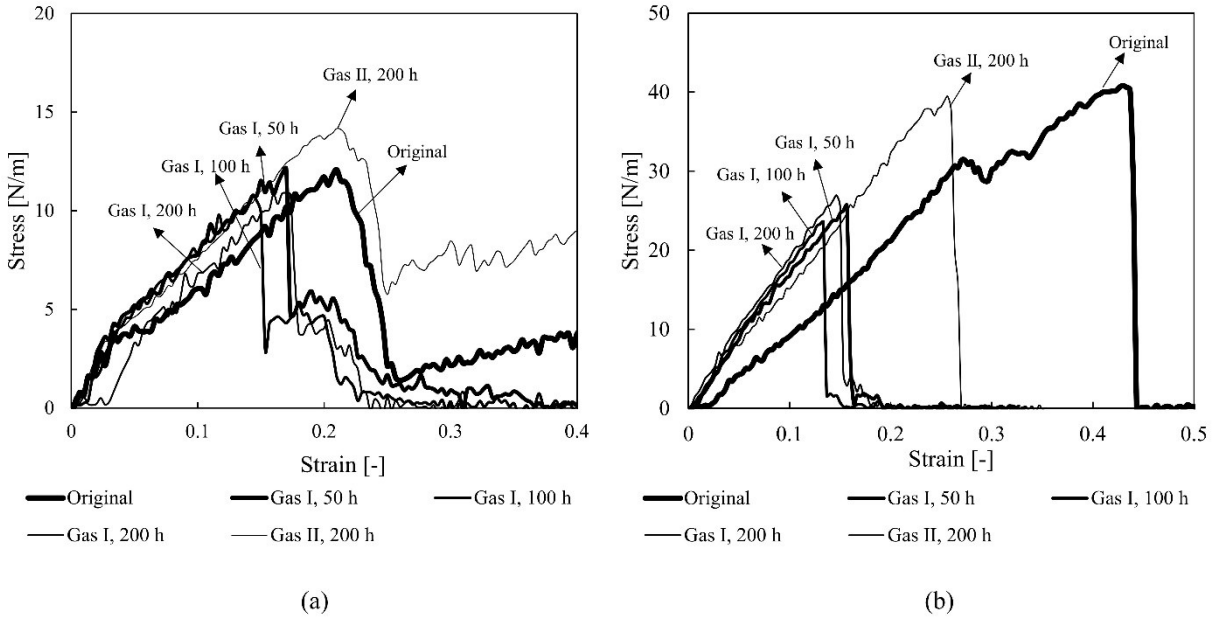

Figure 2.5 Stress-strain curves for PPS filter media: (a) MD and (b) TD.

The stress-strain curves for the PPS filter media in the machine and transverse directions (MD, TD) are shown in **Figure 2.5(a)** and **2.5(b)**, respectively. In the case of both directions, the exposure to Gas II for 200 h increased the elastic modulus of the PPS filter media, and it could not be clearly found the difference in the elastic modulus between Gas I and Gas II. These facts revealed that only high temperature without NO_2 gas, annealing effect, could reduce the elastic deformation of the PPS filter media [17,18]. This tendency was more prominent in the TD.

The retention of tensile strength and elongation in the MD and TD are the mechanical properties of the PPS filter media that were monitored. From **Figure 2.5**, the tensile strength of the original PPS filter media in the MD was 12.3 N/mm and that in the TD was 39.9 N/mm. The tensile strength in the TD was higher than that in the MD since the nonwoven fabric contained more fibers oriented in the TD than in the MD. Elongation of the original PPS filter media in the MD was 22.04 mm and that in the TD was 42.34 mm.

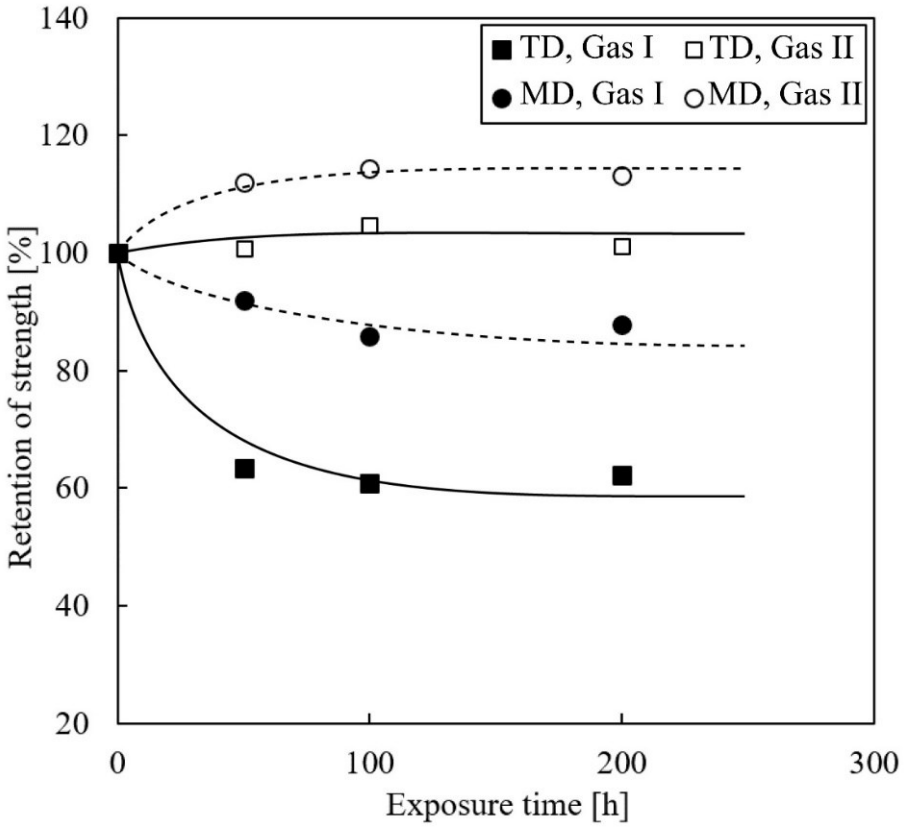

Figure 2.6 Change in the retention of the tensile strength of the PPS filter media as a function of exposure time to Gas I and Gas II.

Figure 2.6 shows the retention of strength as a function of exposure time. Both kinds of exposure gases provide similar changes of the tensile strength in the MD as well as in the TD. In the case of Gas II, the tensile strength in the MD and the TD initially increased up to 100 h and then decreased very gradually. Namely, the crystallization of the amorphous region and the degradation of the crystalline and amorphous regions occurred simultaneously in the fiber. In general, the crystallization process increases the fiber strength whereas degradation decreases the strength of the fibers [22]. Since the crystallization process in the fiber was thought to be dominant initially, this increase in tensile strength is considered to be due to the improvement in the crystallinity of the PPS fiber by the annealing effect under a high temperature oxygen atmosphere [17]. However, this trend was more pronounced in the TD than in the MD. On the other hand, in the case of Gas I, the tensile strength decreased rapidly to reach a constant value. An increase in tensile strength did not occur in either direction due to NO_2 gas accelerating the degradation of the crystalline and amorphous regions in the PPS fibers. The tensile strength for the TD and MD at 200 h were 62.3 % and 87.8 %, respectively. The decrease in tensile strength was greater in the TD because this fiber orientation has more laid fibers than in the MD. The deterioration of filter strength is

hypothesized to be caused by the change of fiber strength from faults in the morphology of the fibers, as mentioned above.

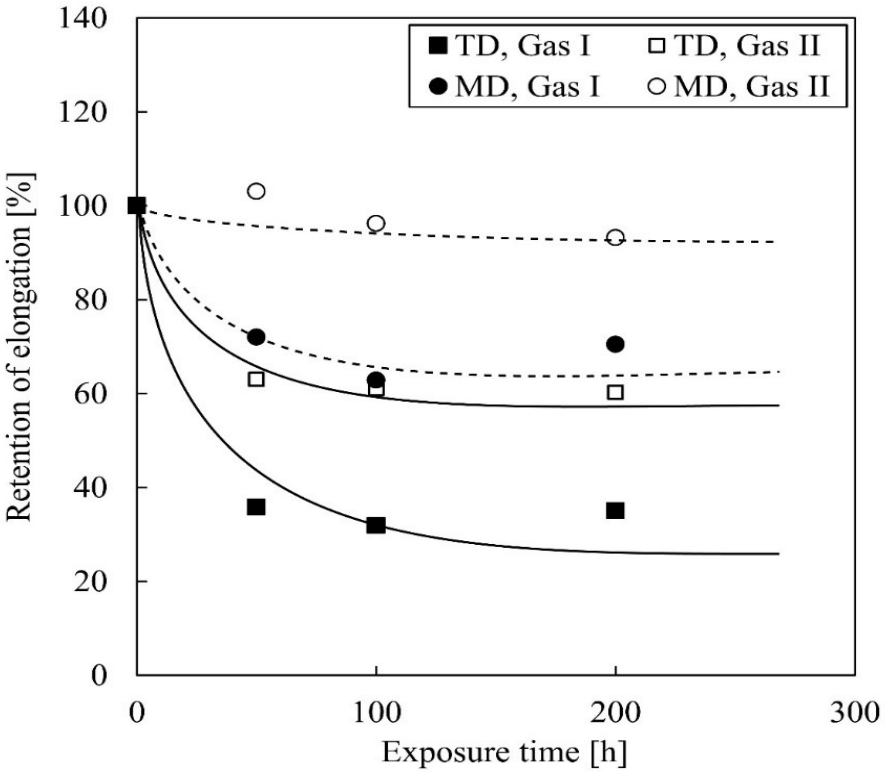

Figure 2.7 Change in the retention of the elongation of the PPS filter media as a function of exposure time to Gas I and Gas II.

Figure 2.7 represents the change in retention of elongation of the PPS filter as a function of exposure time. When the PPS filter was exposed to Gas II, elongation in the MD gradually and slightly decreased, whereas in the TD, elongation initially decreased drastically. On the other hand, when exposed to Gas I, elongation in both the MD and the TD initially decreased considerably, then plateaued. Moreover, this trend was observed more clearly in the TD than in the MD, independent of the kind of gas used. Reduction of the tensile strength shown in Figure 5 could also be caused by a decrease in the maximum elongation [18]. As the filter media exposed to NO_2 gas always has a lower retention of elongation than that exposed to Gas I, chemical degradation is thought to occur from NO_2 gas in addition to thermal degradation.

2.3.2 Effect on chemical properties

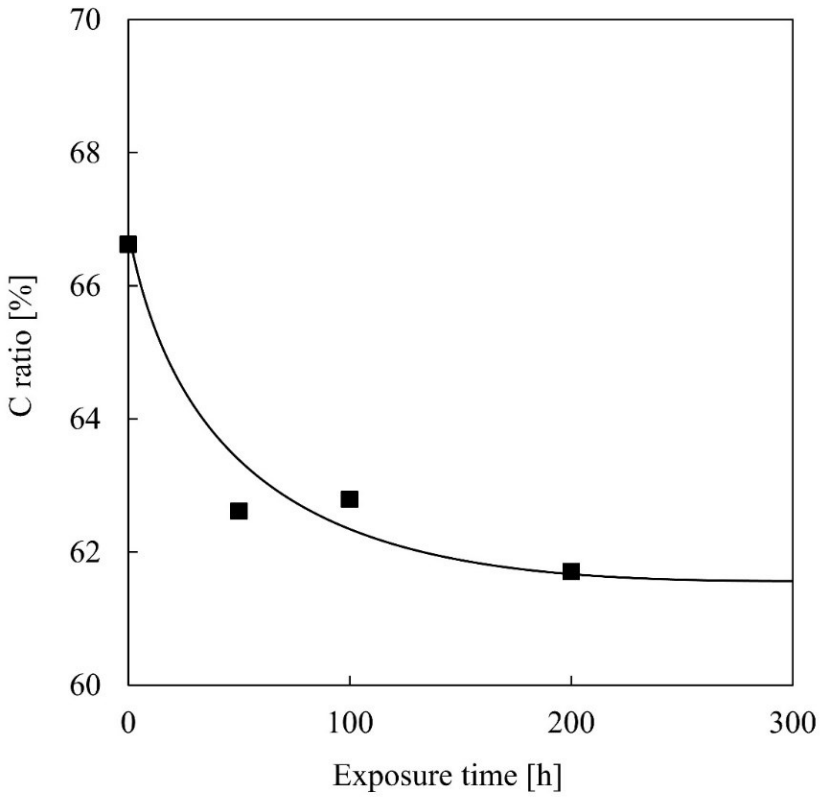

Figure 2.8 Atomic ratio of C in the PPS filter media as a function of exposure time to Gas I.

The relationship between exposure time and the ratio of carbon in the PPS filter media by CHNS analysis is shown in **Figure 2.8**. The ratios of other elements by CHNS analysis of Gas I and Gas II are listed in **Table 2.2**. In the case of Gas I, the atomic ratio of C in the PPS filter drastically decreased with increasing exposure time during the first 50 h, then slightly decreased and remained constant. This trend is in good agreement with the change in tensile strength of the PPS filter. It has been reported that the change in strength of the filter media is almost proportional to that in the atomic ratio of C in PPS [19]. However, since the reduction of the atomic ratio of C in this experiment was much less than in the previous paper [19], it may not be appropriate to evaluate the strength with the atomic ratio of C. Further, it was also confirmed that the atomic ratios of H and S slightly increased and decreased, respectively. The increasing atomic ratio of H and decreasing atomic ratios of C and S are thought to be mainly due to the formation of polyarylene sulfoxide and diphenyl sulfone [24]. This also suggests that oxidizing corrosion occurred during NO_2 gas exposure. On the other hand, it could not be found the substantial change in the CHNS analysis results

of the PPS filter exposed to Gas II for 200h. These facts mean that oxidizing corrosion could not occur without NO_2 gas.

Table 2-2 Result of CHNS elemental analysis of PPS filter media.

Gas Type	Time [h]	C [%]	H [%]	S [%]
	0	66.62	3.73	29.65
Gas I	50	62.61	3.98	28.76
	100	62.79	4.01	28.83
	200	61.71	3.98	28.45
Gas II	200	65.24	3.93	29.59

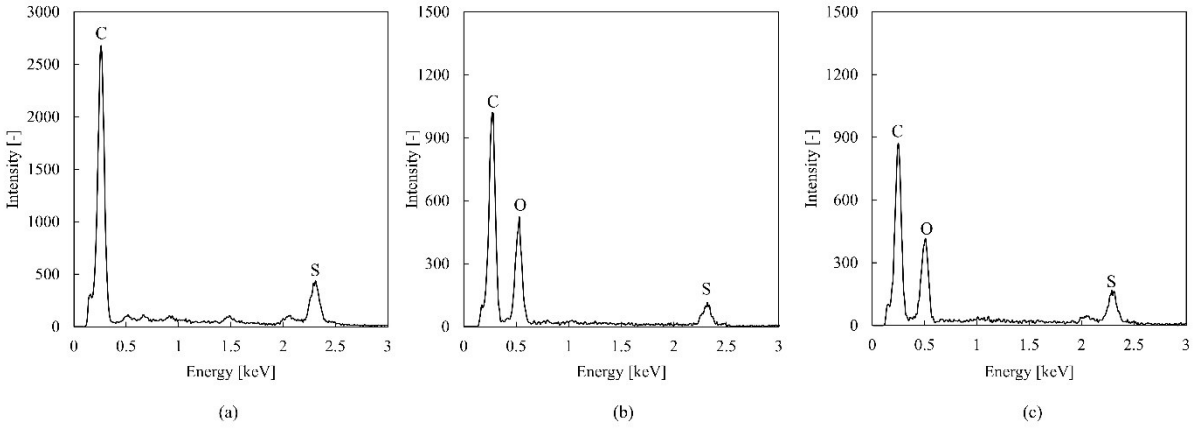

Figure 2.9 EDS spectra of PPS filter media: (a) original; (b) exposed to Gas I for 50 h; and (c) exposed to Gas I for 200 h.

EDS spectra of the PPS filter media are shown in **Figure 2.9**. The peaks of C and S were detected in all filters. However, though the peak of O could not be detected at 0.51 keV in the original filter and one exposed to Gas II, it could be found only in the filters after NO_2 gas exposure. Moreover, the peak intensity ratio of O/C initially increased considerably with increasing exposure time for Gas I. This finding also reveals that oxidizing corrosion proceeds due to NO_2 gas.

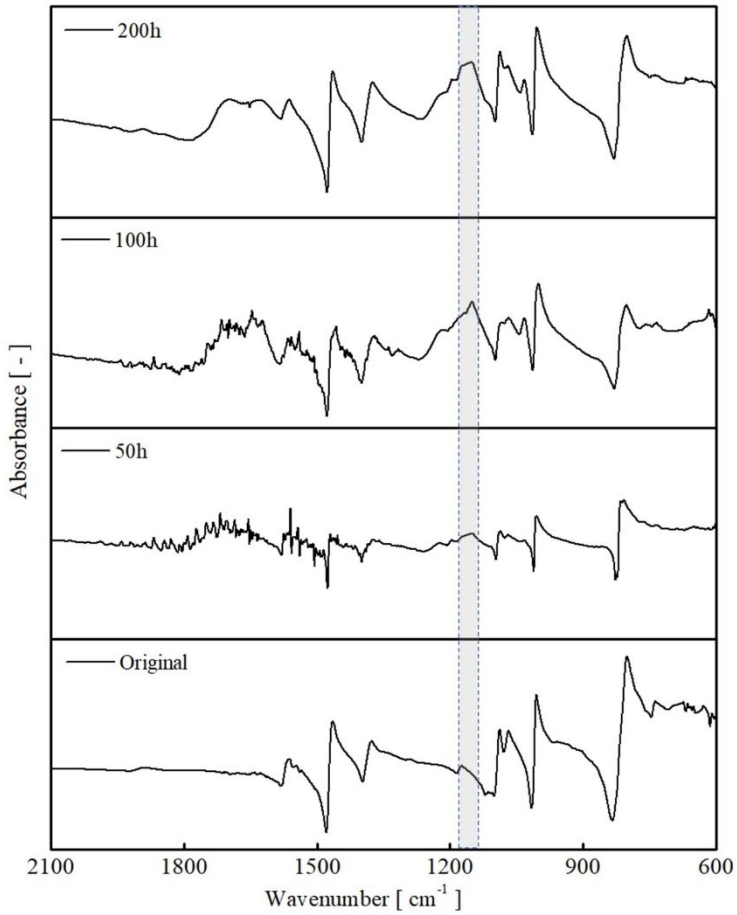

Figure 2.10 Infrared absorbance of PPS filter media exposed to Gas I at select exposure times (0, 50, 100, and 200 h).

Figure 2.10 shows the FTIR spectrum of the PPS filter media exposed to Gases I and II. The spectrum of the original PPS filter showed characteristic peaks at 1397 cm^{-1}, 1481 cm^{-1}, and 1579 cm^{-1}, which are attributed to the C–C in-plane stretching vibration of the phenyl ring. The peak at 1092 cm^{-1} is due to the in-plane C–S stretching vibration, and the peak at 830 cm^{-1} corresponds to the C–H vibration of the benzene skeleton, arising from surface deformation [25]. New absorption peaks are observed at 1024 cm^{-1} and 1153 cm^{-1} in PPS after exposure to NO_2 gas, of which the intensity increased with increasing exposure time. These new absorption peaks correspond to –SO– and O=S=O stretching vibrations [20,26]. This finding indicates that the S atoms in PPS were oxidized and that the structure of PPS changed. This proves that a reaction occurred between PPS and NO_2 gas. Ultimately, new oxygen-containing functional groups were introduced into the PPS molecular structure. On the other hand, new absorption peaks could not be also detected on the FTIR spectrum of the filter media exposed to Gas II for 200 h. This result strengthens that PPS could not be oxidized and changed structurally without NO_2 gas under high temperature condition.

Under long-term exposure in a corrosive and oxidative atmosphere at high temperature, cross-linking and oxidation occurred in PPS molecules [16]. Oxidation occurred at the thio-ether bond and the oxygen linked to the main chain of PPS in the form of sulfide, resulting in the formation of sulfoxide and sulfone groups in PPS molecules. Radical reactions with different transition states formed diphenylsulfone as the final product [27]. It has been reported that a chain of molecules becomes connected to each other and forms a network with a dense molecular arrangement [28]. PPS molecules could be oxidized into compounds with phenolic and carbonyl groups by cleavage of the benzene-sulfur bonds and through other free-radical reactions [24].

2.3.3 Effect of NO_2 gas concentration

SEM images of the fibers that constitute the PPS filters exposed to test gases of various NO_2 concentrations and exposure times are shown in **Figure 2.11**. The original PPS fiber was cylindrical and had a smooth surface. At a relatively low NO_2 concentration of 250 ppm, protrusions, and mottles on the surface of the fiber increased with increasing exposure time, but severe damage (e.g., cracks) were not detected on the surface, even after 200 h of exposure. On the contrary, exposure to the relatively high NO_2 concentration of 1500 ppm resulted in severe damage, such as cracking and splitting, that occurred on the entire surface of the fiber, even at a short exposure time. As the exposure time increased, the extent of damage became more severe, and the number of cracks and delamination increased. These findings suggest that increasing NO_2 gas concentration promotes degradation of the mechanical properties of the PPS filter, because the morphological damage of filter fibers directly results in a decrease in the tensile strength of the PPS filter.

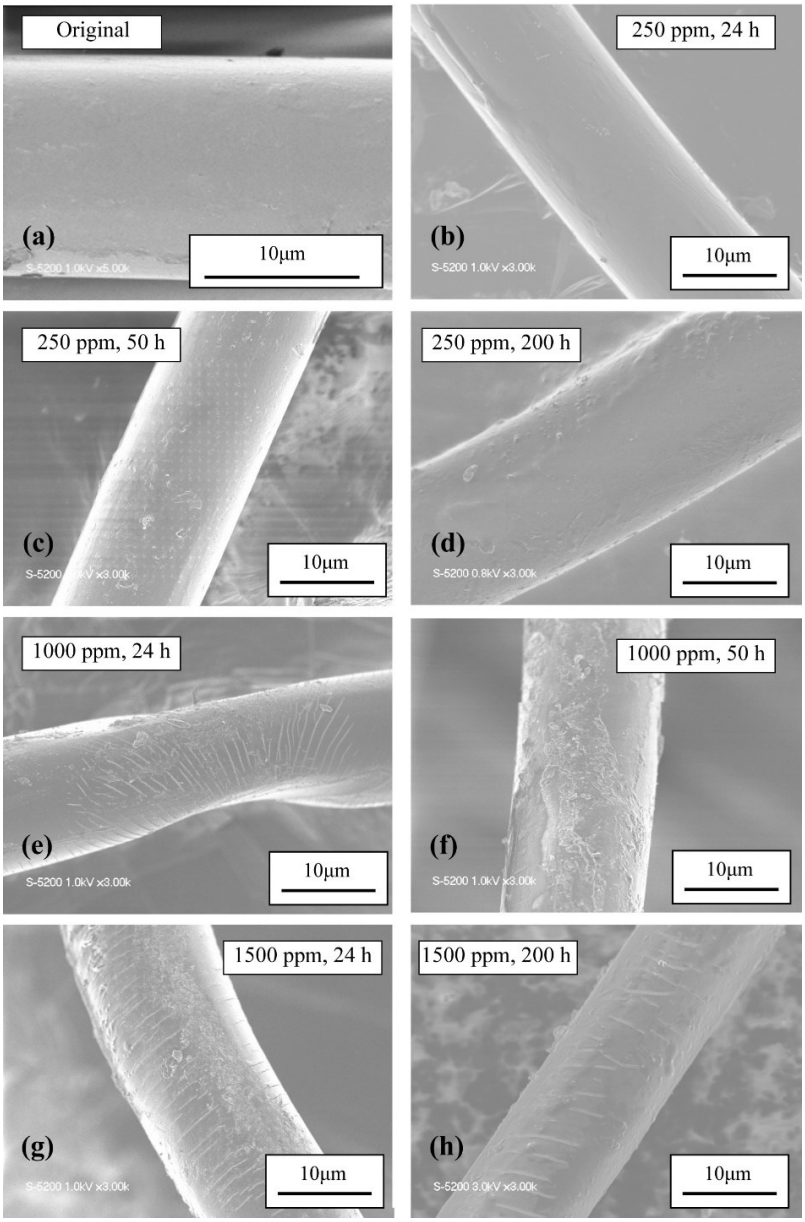

Figure 2.11 SEM images of PPS filter fibers: (a) original; (b) 250 ppm NO_2 for 24 h; (c) 250 ppm NO_2 for 50 h; (d) 250 ppm NO_2 for 200 h; (e) 1000 ppm NO_2 for 24 h; (f) 1000 ppm NO_2 for 200 h; (g) 1500 ppm NO_2 for 24 h; and (h) 1500 ppm NO_2 for 200 h.

The change in the retention of the tensile strength of the PPS filter in the MD and TD with increasing exposure time for various NO_2 concentrations is shown in **Figure 2.12(a)** and **2.12(b)**, respectively. All NO_2 concentrations resulted in similar changes in the tensile strength in the MD and TD. Tensile strength decreased rapidly at the beginning of exposure, especially within the initial 24 h, gradually reaching a constant value. An increase in tensile strength was not observed in either direction; this occurred because of the improved crystallinity of PPS induced by the annealing effect upon exposure to the atmosphere at high temperature [17]. Hence, NO_2 gas is thought to accelerate degradation of both the crystalline

and amorphous regions in the PPS. Furthermore, the PPS filter exposed to higher NO_2 concentrations always exhibited lower tensile strength. As the NO_2 concentration increased, the decrease in tensile strength occurred more rapidly, which was more pronounced in the TD because more fibers were oriented in the TD than in the MD. It has been reported that the degradation of PPS filter tensile strength is caused by both a reduction in the tensile strength of PPS fibers due to fiber damage, as described above, and by a change in the friction coefficient, which represents contributions from fiber friction and entanglement to the tensile strength of the PPS filter [19]. Accordingly, both influences should be considered when estimating tensile strength degradation of the PPS filter. No fiber damage was observed by SEM in the fibers within 24 h of exposure at low NO_2 concentration, which suggests that tensile strength degradation in the early stage of exposure is mainly due to a change in the friction coefficient, whereas degradation in the latter stage is due to fiber damage.

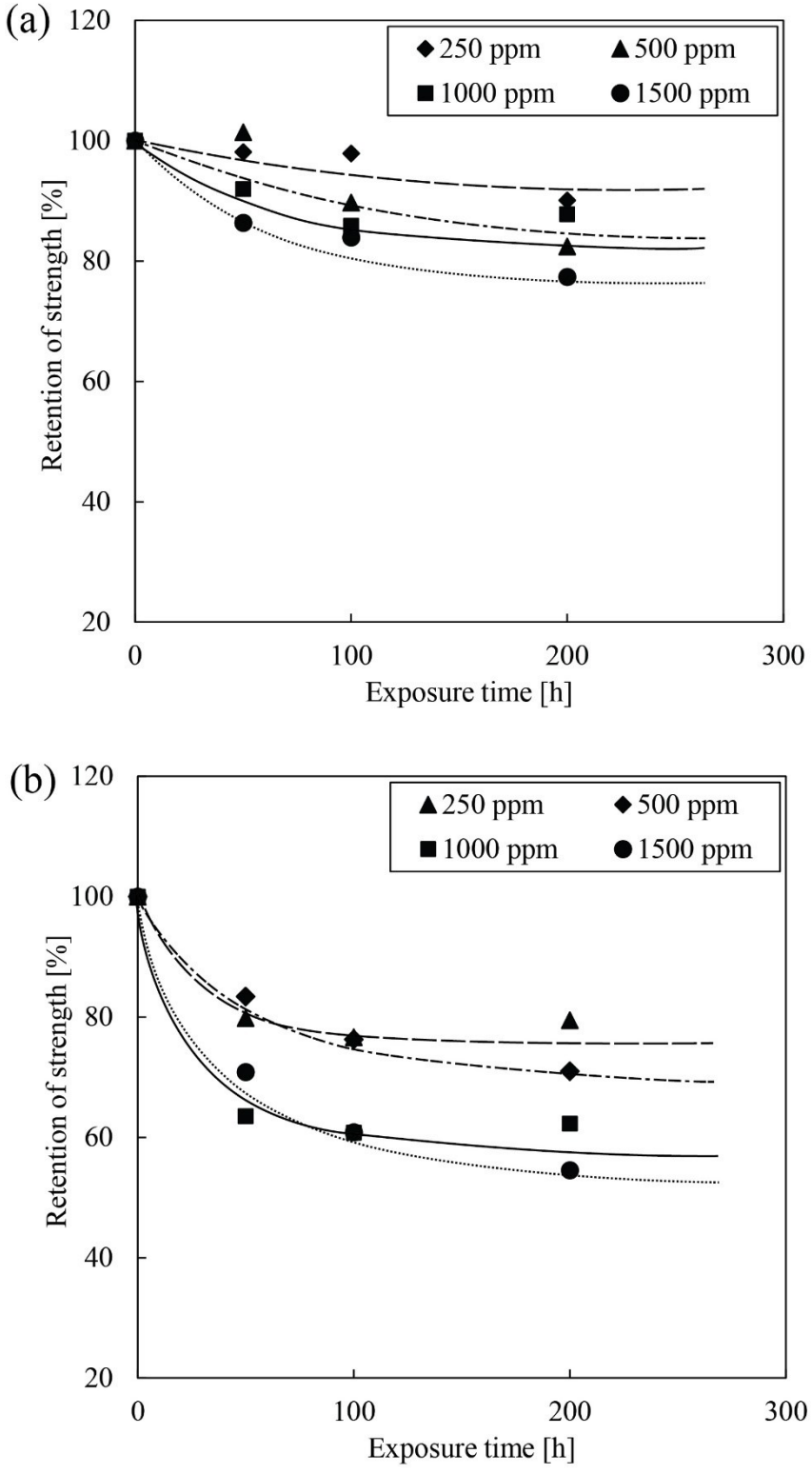

Figure 2.12 Change in the retention of the tensile strength of the PPS filter media as a function of exposure time: (a) MD and (b) TD direction.

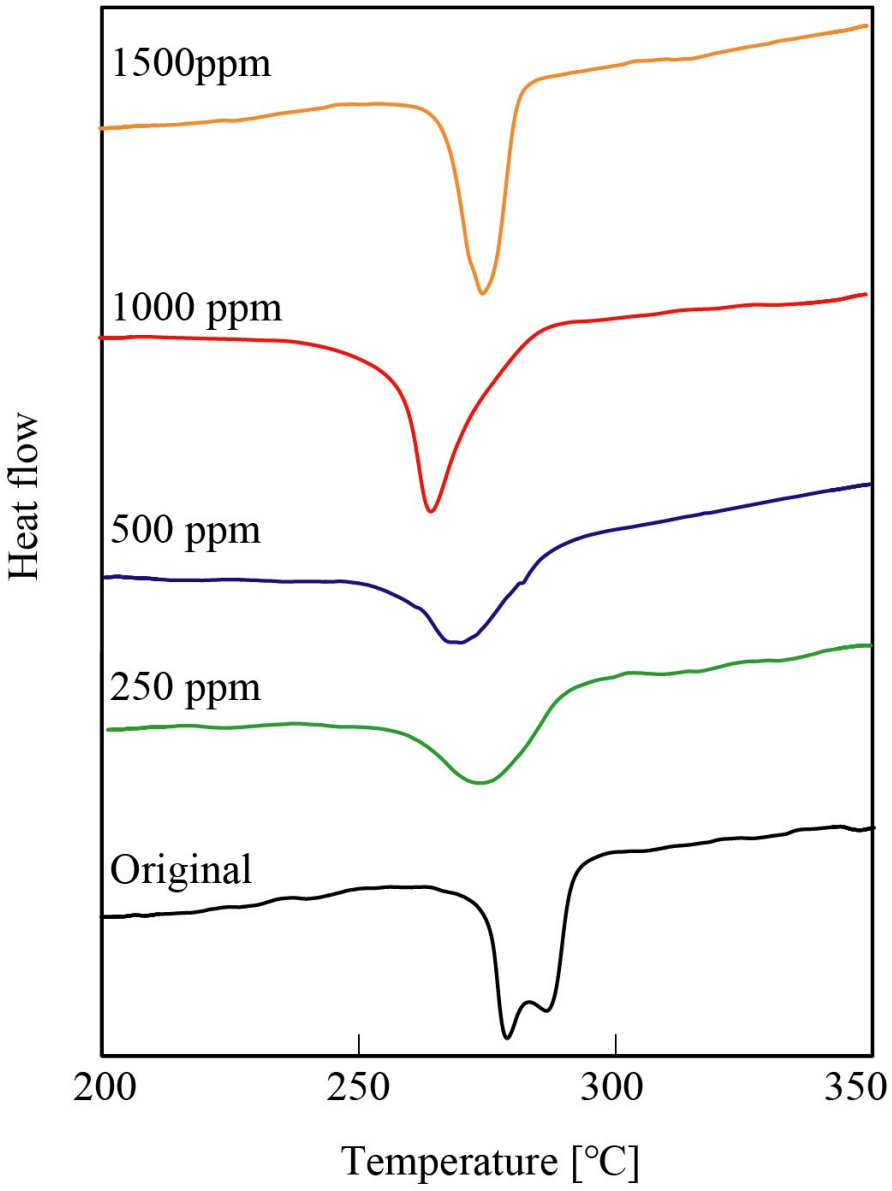

Figure 2.13 DSC analysis curves of the original PPS filter and filters exposed to test gases with various NO_2 concentrations.

DSC analysis of the original PPS filter and filters exposed to test gases of various NO_2 concentrations for 200 h are shown in **Figure 2.13**. Regardless of the NO_2 concentration in the test gas, each filter exhibited only an endothermic peak around the melting point of PPS (285 °C). **Table 2-3** lists the degree of crystallinity of each PPS calculated from **Figure 2.13** using the heat of fusion of completely crystallized PPS (146.2 J/g). Assuming that the change in the molecular structure of PPS induced by NO_2 does not affect the heat of fusion, the degree of crystallinity of all PPS exposed to test gases containing NO_2 is nearly the same as that of the original PPS. The filter exposed to the test gas without NO_2 exhibited higher crystallinity than the original filter, which implies that NO_2 gas may inhibit crystallization

of PPS or amorphized the crystalline part of PPS. In other words, regardless of the NO_2 concentration in the test gas, the crystallization of PPS hardly progressed even at high temperature. Furthermore, a reduction in the diffusion coefficient of the gas into PPS due to crystallization did not occur for PPS exposed to test gases containing NO_2 [29].

Table 2-3 Degree of crystallinity of the original PPS filter and filters exposed to test gases of various NO_2 concentrations for 200h.

NO_2 concentration [ppm]	Degree of crystallinity [%]
Original	22
0	38
250	18
500	19
1000	25
1500	21

2.3.2 ***Estimation with reaction model***

As described in sections 3.1 and 3.2, the chemical reaction between NO_2 gas and PPS changes the molecular structure, which is thought to reduce the tensile strength of the PPS filter media. Modeling the gas-solid reaction can be used to investigate the oxidation of PPS by NO_2 gas because the oxidation process is fundamentally a type of gas-solid reaction [30]. Therefore, in order to propose a simple model to estimate the change in tensile strength of the PPS filter media with exposure time, the reaction rate was analyzed with a gas-solid reaction model based on the change in the NO_2 concentration in the gas exhausted from the exposure chamber.

To simplify the reaction model, the chemical reaction between NO_2 gas and PPS was assumed to proceed as a NO_2 gas diffusion-controlled reaction with the following stoichiometric formula:

$$a\ NO_2 + PPS \rightarrow b\ PPS' + c\ NO + d\ N_2$$

This means that NO_2 gas diffuses from the fiber surface through the annular product PPS' layer and reacts on the surface of the unreacted cylindrical PPS remaining in the center of the fiber. According to the unreacted core model in the cylindrical coordinate system, the

relationship between the conversion of PPS x_{PPS} and the reaction time t can be given by Eq. (2-2) [30]:

$$\frac{t}{t^*} = x_{PPS} + (1 - x_{PPS})\ln(1 - x_{PPS}) \quad (2\text{-}2)$$

where t^* is the reaction completion time, which is the time when $x_{PPS} = 1$ and can be defined by the following equation:

$$t^* = \frac{a\,R^2\,\rho_{PPS}}{4\,D_e\,C_{NO2-in}} \quad (2\text{-}3)$$

Here, D_e is the effective diffusion coefficient of NO_2 gas in the product PPS', ρ_{PPS} is the density of PPS, R is the radius of the PPS fiber, and $C_{NO2\text{-}in}$ is the NO_2 molar concentration in the supplied test gas.

Hence, the NO_2 concentration in the exhausted gas $C_{NO2\text{-}out}$ can be obtained from the following equations, with t^* and K as fitting parameters.

$$C_{NO2-out} = C_{NO2-in}\left(1 - K\frac{1}{t^*\ln(1 - x_{PPS})}\right) \quad (2\text{-}4)$$

$$K = \frac{V\,C_{PPS}}{a\,v} \quad (2\text{-}5)$$

Here, V and v are the volume of the PPS fiber and the flow rate of supplied gas, respectively. C_{PPS} represents the molar density of PPS.

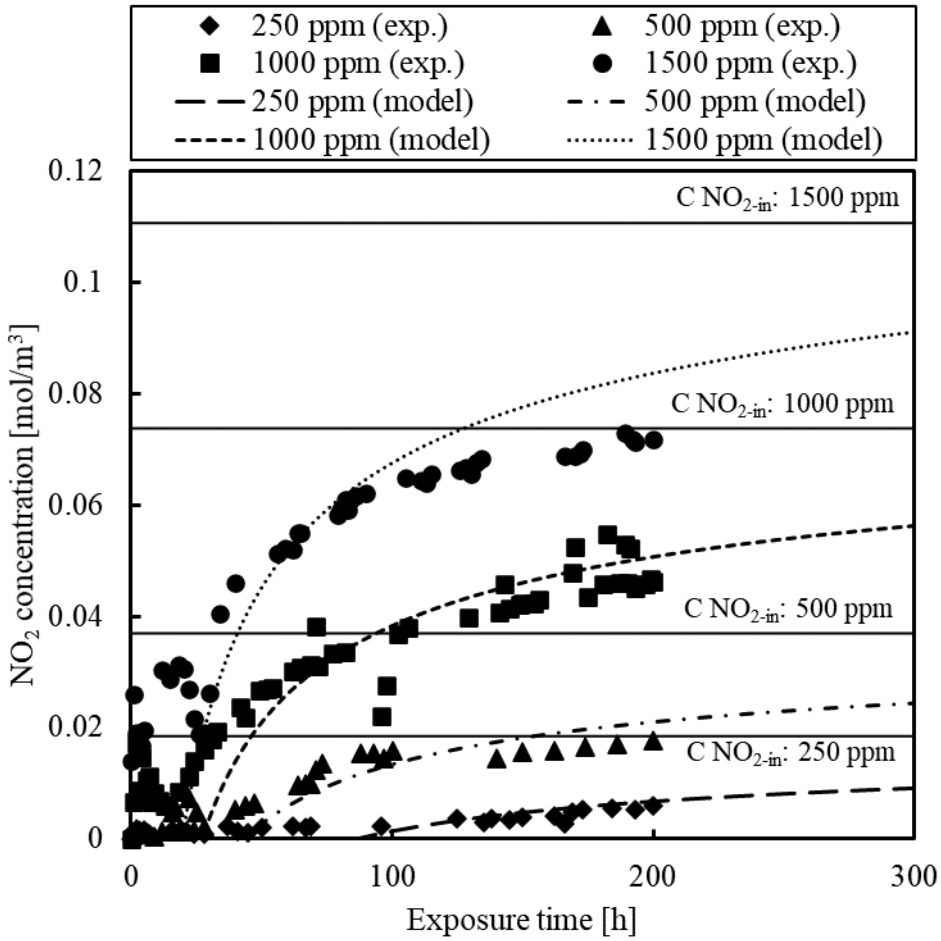

Figure 2.14 NO_2 concentration in exhausted gas as a function of exposure time.

Figure 2.14 shows the change in the NO_2 concentration in the exhaust gas as a function of the exposure time. The solid lines in the figure represent the NO_2 concentrations in the supplied test gas. The NO_2 concentration in the exhausted gas initially remained constant at almost zero; lower NO_2 concentrations in the supplied test gas resulted in the exhaust gas remaining at nearly zero concentration for a longer duration. Then, the NO_2 concentration in the exhausted gas increased monotonically over time toward that of the supplied gas, and the slope decreased with increasing exposure time. The correlated curves shown in **Figure 2.14** represent the fitted results obtained from Eq. (2-2) – (2-5) using the optimized fitting parameters listed in **Table 2-4**. In any case, the optimum value of one fitting parameter, K, was found to be 23 mol·h/m^3 constant, which gave a = 20.3 in the stoichiometric formula. The optimum value of the other fitting parameter, t^*, decreased as the NO_2 concentration in the supplied gas increased. A lower NO_2 concentration in the supplied gas gave a slightly larger value of D_e derived from t^*, suggesting that the diffusion rate of NO_2 gas into the PPS fiber is slightly faster for lower concentrations of NO_2 in the supplied gas. This may be

caused by differences in the extent of physical damage of the PPS fibers, as the crystallinity of PPS was not affected by exposure to NO_2 gas at high temperature (**Table 2-3**), and higher NO_2 concentrations led to more severe damage of the PPS fibers (**Figure 2.11**).

Table 2-4 Optimal parameters used for fitting and calculation of physical properties

$C_{NO2\text{-}in}$ [ppm]	K [mol·h/m^3]	t^* [h]	a	D_e [m^2/h]
250	23	8000	20.3	3.1×10^{-5}
500		4000		3.1×10^{-5}
1000		1500		4.1×10^{-5}
1500		1000		4.1×10^{-5}

Because the theoretical correlated curve obtained from the proposed model agreed well with the experimental data for all test gases, this model is a reliable representation of the system for all NO_2 concentrations. However, a little larger errors at the initial stage of exposure, particularly in the case of higher NO_2 concentrations, imply that the diffusion coefficient may increase with exposure time. This is further supported by the observation that fiber surface damage grew more severely with increasing exposure time and NO_2 concentration.

Next, a model to estimate the change in the tensile strength of the PPS filter media was proposed. The tensile strength $\sigma(t)$ of the PPS fiber was assumed to be the linear sum of the tensile strength of the unreacted part and that of the completely reacted part. It has been reported that the tensile strength of the PPS filter can be expressed by the tensile strength of the PPS fiber and the overall friction coefficient for fiber friction and entanglement in the filter [19]. Therefore, the tensile strength of the filter is obtained as follows:

$$\sigma_{filter,i}(t) = f_i\left[(1 - x_{PPS})\sigma_{i,original} + x_{PPS}\sigma_i(t^*)\right] \qquad (2\text{-}6)$$

where, f_i and $\sigma_{filter,i}(t)$ are the overall friction coefficient and the tensile strength of the PPS filter in the i direction (MD or TD), $\sigma_{i,original}$ is the tensile strength of the original PPS fiber (i.e., that of the unreacted part), and $\sigma_i(t^*)$ is the tensile strength of the PPS' fiber at the completion time, which represents that of the completed reaction part.

Based on the above discussion related to **Figures 2.12 (a)** and **2.12 (b)**, the sudden decrease in the tensile strength of the PPS filter observed within the first 3 h of exposure may be attributed primarily to a decrease in the overall friction coefficient, whereas the

subsequent decrease in strength over a prolonged period is primarily attributed to a reduction in the tensile strength of the PPS fiber. Tanthapanichakoon et al. reported that fiber orientation in the filter media barely changed during exposure to an acid [19]. Therefore, assuming that $\sigma_{i,\text{original}}$ is almost equal to the tensile strength of the PPS fiber in the *i* direction at 3 h, and that f_i is constant after 3 h of exposure, $\sigma_{\text{filter},i}(t)$ (t > 3 h) can be expressed by following equation:

$$\sigma_{filter,i}(t) = (1 - x_{PPS})\sigma_{filter,i}(3\ hour) + x_{PPS}\sigma_{filter,i}(t^*) \qquad (2\text{-}7)$$

Hence, $\sigma_{\text{filter},i}(t)$ (t > 24 h) can be obtained using Eq. (2-2) and (2-7) with $\sigma_{\text{filter},i}(t^*)$ as a fitting parameter because $\sigma_{\text{filter},i}$(3 h) and x_{PPS} were previously acquired from the measurement and model calculations.

The relationship between the exposure time and the tensile strength of the PPS filter in both MD and TD directions is shown again with the fitted correlated curves in **Figure 2.15 (a)** and **2.15 (b)**, respectively. Independent of the NO_2 concentration, all correlated curves could be determined using optimal constant fitting parameters for both directions, where $\sigma_{filter,MD}(t^*)$ = 12 N/mm and $\sigma_{filter,TD}(t^*)$ = 9 N/mm, thus demonstrating the validity of this model. This developed evaluation model can adequately predict the change in the tensile strength of the PPS filter with increasing exposure time for any NO_2 concentration. For both the machine and transverse directions, the predicted fit line accurately reproduced the experimental results.

The present prediction model for tensile strength change of the PPS filter is practically useful, since it may also be adapted to bag filters operated on an industrial scale in real severe environments. Therefore, bag filter lifetime can be estimated to control dust emissions in industrial facilities [32].

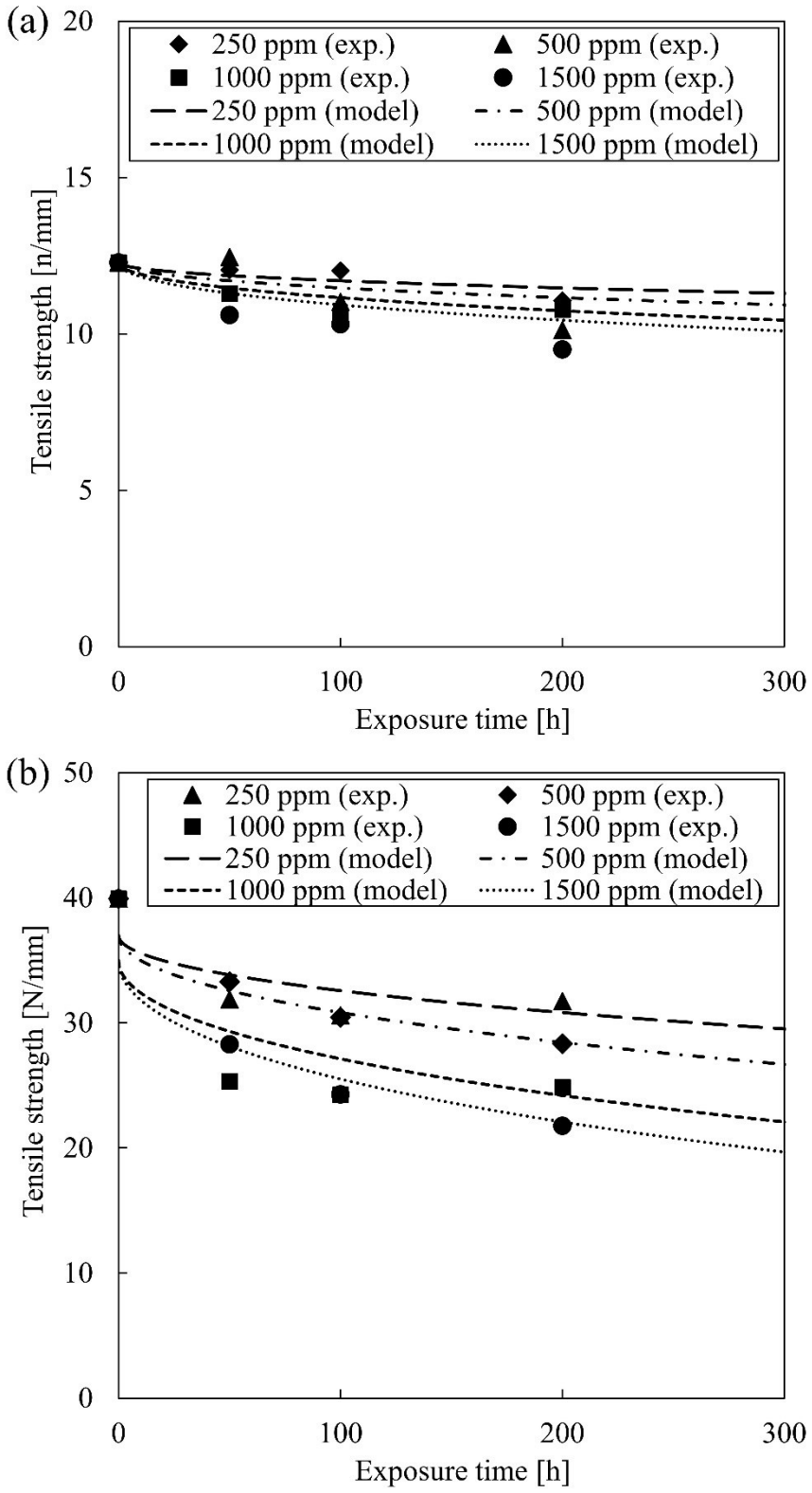

Figure 2.15 Change in the tensile strength of PPS filter media with exposure time for Gas I: (a) MD and (b) TD.

2.4 Conclusions

The degradation of the PPS filter media by NO_2 gas at high temperature was clarified using a continuous-flow exposure method. Moreover, a method to evaluate the decrease in the mechanical strength of the PPS filter media by NO_2 gas exposure was proposed through modeling the progress of a chemical reaction between the PPS fiber and NO_2 based on the unreacted core model of reaction engineering. The results obtained can be summarized as follows:

1. As the exposure time to NO_2 gas increased, the tensile strength and elongation of the PPS filter media for both the machine and transverse directions decreased. These reductions were observed in the TD more markedly than in the MD.
2. SEM images revealed that the exposure to NO_2 gas severely damaged the PPS fiber through many protrusions on the surface, cracking, and splitting, which ultimately reduce the tensile strength of the filter media.
3. The atomic ratio of C in the PPS filter media exposed by gas I measured by CHNS analysis drastically decreased with increasing exposure time, then slightly decreased to remain constant. This trend is in good agreement with the change in tensile strength of the filter media.
4. SEM-EDS analysis clarified that the only filter media after NO_2 gas exposure contained O, which the original PPS did not contain.
5. The exposure to NO_2 gas enhanced the oxidation of S in PPS and introduced new oxygen-containing functional groups such as –SO– and O=S=O into the PPS molecular structure.
6. The increasing NO_2 gas concentration promotes more degradation of the mechanical properties of the PPS filter because the morphological damage of filter fiber increased.
7. Assuming that the chemical reaction between PPS and NO_2 gas is diffusion-controlled by NO_2, an unreacted core model in the cylindrical coordinate system can be applied as a model to estimate the change in NO_2 concentration in the exhaust gas, which successfully reproduced the experimental data.
8. A model that evaluates the change in the tensile strength of the filter media with the conversion of PPS and the tensile strength of the PPS fiber was also proposed, which could express experimental data in both the MD and TD direction.

References

[1] J. Steffens, J.R. Coury, Collection efficiency of fiber filters operating on the removal of nano-sized aerosol particles: I-Homogeneous fibers, Sep. Purif. Technol. 58 (2007) 99–105. https://doi.org/10.1016/j.seppur.2007.07.011.

[2] N. Mao, Y. Otani, Y. Yao, C. Kanaoka, Modeling the filtration process with a flat-type fabric filter, Adv. Powder Technol. 17 (2006) 237–256. https://doi.org/10.1163/156855206777213357.

[3] N. Mao, Y. Yao, M. Hata, M. Wada, C. Kanaoka, Comparison of filter cleaning performance between VDI and JIS testing rigs for cleanable fabric filter, Powder Technol. 180 (2008) 109–114. https://doi.org/10.1016/j.powtec.2007.03.017.

[4] H. Mizukoshi, M. Masui, N. Namiki, J.C. Kim, Y. Otani, Suppression of solidification of calcium-rich incinerator fly ash during thermal treatment for decomposition/detoxification of dioxins, Adv. Powder Technol. 18 (2007) 143–154. https://doi.org/10.1163/156855207780208574.

[5] S. Li, F. Zhou, F. Wang, B. Xie, Application and research of dry-type filtration dust collection technology in large tunnel construction, Adv. Powder Technol. 28 (2017) 3213–3221. https://doi.org/10.1016/j.apt.2017.10.003.

[6] A.N. Huang, N. Maeda, S. Sunada, T. Fukasawa, H. Yoshida, H.P. Kuo, K. Fukui, Effect of cold air stream injection on cyclone performance at high temperature, Sep. Purif. Technol. 183 (2017) 293–303. https://doi.org/10.1016/j.seppur.2017.04.012.

[7] T. Oshitari, K. Yamamoto, K. Fukui, H. Yoshida, Classification characteristics of a cyclone type classifier with improved collection boxes for separating particles near the wall surface, J. Chem. Eng. Japan. 50 (2017) 492–500. https://doi.org/10.1252/jcej.16we267.

[8] L.W. Shacklette, R.L. Elsenbaumer, R.R. Chance, H. Eckhardt, J.E. Frommer, R.H. Baughman, Conducting complexes of polyphenylene sulfides, J. Chem. Phys. 75 (1981) 1919–1927. https://doi.org/10.1063/1.442217.

[9] F. Bertinelli, P.C. Bizzarri, C. Della Casa, S. Saltini, Poly(m-phenylene disulfide): Antimony pentafluoride doping and infrared spectroscopy, J. Polym. Sci. Part B Polym. Phys. 24 (1986) 2197–2208. https://doi.org/10.1002/polb.1986.090241004.

[10] W.K. Son, H.K. Sang, S.G. Park, Synthesis and exchange properties of sulfonated

poly(phenylene sulfide) with alkali metal ions in organic solvents, Bull. Korean Chem. Soc. 22 (2001) 53–58.

[11] L.R. Yao, J.Y. Kim, The Microstructure and Mechanical Property of Meta-Aramid Nanofiber Web for High Temperature Filter Media, Adv. Mater. Res. 175–176 (2011) 318–322. https://doi.org/10.4028/www.scientific.net/AMR.175-176.318.

[12] A. Mukhopadhyay, V. Pandit, K. Dhawan, Effect of high temperature on the performance of filter fabric, J. Ind. Text. 45 (2014) 1587–1602. https://doi.org/10.1177/1528083714567240.

[13] B. Yu, J. Han, Q. Zhang, X. He, G. Xu, Effect of finishing on the structure and filtration property of PPS filter, High Perform. Struct. Mater. Eng. Pts 1 2. 217–218 (2011) 1272–1276. https://doi.org/10.4028/www.scientific.net/AMR.217-218.1272.

[14] V.C. Vives, J.S. Dix, D.G. Brady, Polyphenylene Sulfide (PPS) in Harsh Environments, in: 1983: pp. 65–85. https://doi.org/10.1021/bk-1983-0229.ch006.

[15] M. Zhang, X. Wang, C. Li, Y. Bai, B. Cheng, Z. Li, Effects of hydrogen bonding between MWCNT and PPS on the properties of PPS/MWCNT composites, RSC Adv. 6 (2016) 92378–92386. https://doi.org/10.1039/c6ra19119c.

[16] R.T. Hawkins, Chemistry of the Cure of Poly(p-phenylene sulfide), Macromolecules. 9 (1976) 189–194. https://doi.org/10.1021/ma60050a001.

[17] W. Tanthapanichakoon, M. Furuuchi, K. hei Nitta, M. Hata, S. Endoh, Y. Otani, Degradation of semi-crystalline PPS bag-filter materials by NO and O_2 at high temperature, Polym. Degrad. Stab. 91 (2006) 1637–1644. https://doi.org/10.1016/j.polymdegradstab.2005.12.008.

[18] W. Tanthapanichakoon, M. Furuuchi, K.-H. Nitta, M. Hata, Y. Otani, Degradation of bag-filter non-woven fabrics by nitric oxide at high temperatures, Adv. Powder Technol. 18 (2007) 349–354. https://doi.org/10.1163/156855207780860264.

[19] W. Tanthapanichakoon, M. Hata, K. hei Nitta, M. Furuuchi, Y. Otani, Mechanical degradation of filter polymer materials: Polyphenylene sulfide, Polym. Degrad. Stab. 91 (2006) 2614–2621. https://doi.org/10.1016/j.polymdegradstab.2006.05.005.

[20] W. Cai, G. Hu, Oxidation degradation of polyphenylene sulfide needle felt at different sulfuric acid dew point temperatures, High Perform. Polym. 27 (2015) 94–99. https://doi.org/10.1177/0954008314540311.

[21] H.C. Wang, D.H. Jiang, Y. Liu, Life Problem Analysis on PPS Filter Application of Bag Dedusters in Coal-Fired Power Plants, Adv. Mater. Res. 236–238 (2011) 2464–2470. https://doi.org/10.4028/www.scientific.net/AMR.236-238.2464.

[22] Y. Ye, Z. Wang, Effect of Corona Discharge on Polyphenylene Sulfide Filter Material of Electrostatic-Bag Composite Precipitators, Ind. Eng. Chem. Res. 57 (2018) 1319–1330. https://doi.org/10.1021/acs.iecr.7b03829.

[23] ISO16891:2016, Test methods for evaluating degradation of charateristics of cleanable filter media, (2016).

[24] R.M. Black, C.F. List, R.J. Wells, Thermal stability of p-phenylene sulphide polymers, J. Appl. Chem. 17 (1967) 269–275. https://doi.org/10.1002/jctb.5010171001.

[25] G. Zhang, Q. Wang, X. Yu, D. Su, Z. Li, G. Zhang, FTIR-PAS investigation on polyphenylene sulphide, Spectrochim. Acta Part A Mol. Spectrosc. 47 (1991) 737–741. https://doi.org/10.1016/0584-8539(91)80144-8.

[26] A.M. Díez-Pascual, M. Naffakh, Synthesis and characterization of nitrated and aminated poly(phenylene sulfide) derivatives for advanced applications, Mater. Chem. Phys. 131 (2012) 605–614. https://doi.org/10.1016/j.matchemphys.2011.10.025.

[27] L.H. Perng, Thermal decomposition characteristics of poly(phenylene sulfide) by stepwise Py-GC/MS and TG/MS techniques, Polym. Degrad. Stab. 69 (2000) 323–332. https://doi.org/10.1016/S0141-3910(00)00077.

[28] Y. Yang, G. Zhang, J. Liu, S. Long, X. Wang, J. Yang, Thermal cross-link behavior of an amorphous poly (para-arylene sulfide sulfone amide), Polymer (Guildf). 52 (2011) 1013–1018. https://doi.org/10.1016/j.polymer.2011.01.001.

[29] V. Compañ, L.F. Del Castillo, S.I. Hernández, M. Mar López-González, E. Riande, Crystallinity effect on the gas transport in semicrystalline coextruded films based on linear low density polyethylene, J. Polym. Sci. Part B Polym. Phys. 48 (2010) 634–642. https://doi.org/10.1002/polb.21932.

[30] Z. Xu, X. Sun, M.A. Khaleel, A generalized kinetic model for heterogeneous gas-solid reactions, J. Chem. Phys. 137 (2012). https://doi.org/10.1063/1.4740242.

[31] O. Levenspiel, Chemical Reaction Engineering, in: Chem. React. Eng., Wiley, New York, 1999: pp. 566–586.

[32] A. Patnaik, R.D. Anandjiwala, Reasons for Filter Bag Failure and Method Development to Improve its Life Span, Chem. Eng. Technol. 39 (2016) 529–534. https://doi.org/10.1002/ceat.201500282.

Chapter 3

Direct numerical simulation and experiment validation of flow resistivity of nonwoven fabric filter

3.1 Introduction

Bag filter systems are increasingly being installed in incinerators and coal fired power plants to control the emissions of dust and harmful materials because of their economic appeal and collection efficiency[1,2]. Polyphenylene sulfide (PPS) and polyimide (PI) filters have been increasingly used in these systems owing to their excellent chemical, thermal, and mechanical properties[3–7]. PPS filters can be used at temperatures ranging from 160 °C to 240 °C[8], while PI filters can be used at a higher temperature range, from 200 °C to 400 °C[9,10].

The pressure drop across fibrous filter media is a key factor in estimating filtration life and required operating power, and this pressure should be as low as possible. Flow resistivity is one of the main parameters that causes a pressure drop in a fibrous filter. However, both PPS and PI filters have high flow resistivity as a consequence of their complex structure, because commercial filters are commonly formed using nonwoven fabric prepared from long fibers. Thus, it is necessary to further investigate the flow resistivity of PPS and PI filters. Several researchers have constructed empirical equations for the prediction of the pressure drop across a fibrous filter. However, the effects of the random orientation of the fibers were neglected because of the assumption that the fiber arrangement was either perpendicular or parallel to the main flow direction[11]. Very recently, Yang et al. examined the pressure drop across a randomly generated fiber network by applying a direct numerical simulation approach[12]. The results indicated that their model could be used to predict the pressure drop. However, the actual structure of commercial filters, such as PPS and PI filters, is more complicated, and it may be difficult to predict the pressure drop.

Numerical simulations are useful for investigating fluid motion within a porous material. In numerical simulations, the motion of fluid within a porous material can be easily observed, and various parameters can be independently evaluated. In recent years, in addition to the Yang et al. study[12], several studies involving membrane or filter simulations have been reported by other researchers. Ando et al.[13] and Ishigami et al.[14] conducted numerical

simulations of dead-end microfiltration using a direct numerical simulation technique. Kagawa et al.[15] and Mino et al.[16] simulated permeation through a coalescing filter. These studies used membranes and filters with pores and fibers modeled with the simplest geometries, that is, straight and cylindrical pores and fibers. Yoshida et al.[17] applied a combination of the lattice Boltzmann and immersed boundary methods to investigate the effect of the aperture structure of metal woven mesh on flow resistivity. They mathematically created a well-arranged mesh geometry. Ishigami and Mino[18] simulated the permeation of colloidal particle dispersion flow in a microfiltration membrane. The coordination of microporous structure was calculated using a phase-field model in their study. However, the fibrous filter could not be re-created using mathematical or numerical simulation approaches owing to its complex structure.

X-ray computed tomography (CT) is an advanced imaging technique that allows nondestructive and noninvasive imaging of a specimen to depict the cross-sectional and three-dimensional internal structure of the material[19]. Using this technique, the realistic morphology of a fibrous filter can be depicted. Recently, a number of studies that simulate flow directly on an X-ray CT image of porous media have been conducted[20–25]. It is expected that direct numerical simulation that combines an X-ray CT image and the immersed boundary method will make it possible to clarify the relationship between the pressure drop and the flow resistivity of a fibrous filter.

In the present study, a direct numerical simulation model was constructed to investigate the permeation of gas through a fibrous filter by coupling the immersed boundary method[26] and X-ray CT images. Because this model recreated the geometry of the fibrous filter realistically, the investigation of the permeation process was more accurate. In this study, commercial PPS and PI nonwoven fabric filters were utilized. An experiment was performed to measure the pressure drop across the fibrous filter. Then, we compared the simulation results with the experimental results and existing models proposed by previous researchers to validate our model. Based on the simulation results, we calculated the permeability and the Kozeny constant of the fibrous filter using Darcy's law[27] and the Kozeny–Carman equation[28,29] to investigate the flow resistivity during permeation of a gas through PPS and PI filters.

3.2 Numerical method

3.2.1 Governing equations

The governing equations of fluid flow are the continuity and the Navier–Stokes equations, respectively defined as follows:

$$\nabla \cdot \mathbf{u} = 0 \tag{3-1}$$

$$\rho \frac{\partial \mathbf{u}}{\partial t} + \rho \mathbf{u} \cdot \nabla \mathbf{u} = -\nabla p + \mu \nabla^2 \mathbf{u} + \mathbf{f} \tag{3-2}$$

where $\mathbf{u}$ denotes velocity, t is the time, and p is the pressure. The density ρ and viscosity μ of the fluid are assumed to be constant. $\mathbf{f}$ is the momentum exchange that expresses the interaction between a solid and fluid. The fluid is assumed to be incompressible and Newtonian. A Cartesian staggered grid system is used for the arrangement of the Eulerian variables.

3.2.2 Fractional steps method

There are several methods can be used to solve the Navier-Stokes equation, such as Marker and Cell (MAC) method, Semi-Implicit Method for Pressure-Linked Equation (SIMPLE) method, Fractional Step Method, Simplified MAC (SMAC) method, and Highly Simplified (HSMAC) method. In this study, we used the fractional step method [30].

The fractional step method solves the Navier-Stokes equation in a few steps as follows:

Step 1 (Convection term)

$$\frac{\mathbf{u}^{(1)} - \mathbf{u}^{\mathrm{n}}}{\Delta t} + \mathbf{u}^{\mathrm{n}} \cdot \nabla \mathbf{u}^{\mathrm{n}} = \mathbf{0} \tag{3-3}$$

Step 2 (Viscous term)

$$\frac{\mathbf{u}^{(2)} - \mathbf{u}^{(1)}}{\Delta t} = \frac{1}{\rho} \nabla \cdot \mu \nabla \mathbf{u}^{*} \tag{3-4}$$

Step 3 (Continuity equation and pressure gradient term)

$$\frac{\mathbf{u}^{\mathrm{n}+1} - \mathbf{u}^{(2)}}{\Delta t} = -\frac{1}{\rho} \nabla p \tag{3-5}$$

By dividing each term, the Navier-Stokes equation can be solved using a method which suitable for each term, and it is easy to modify or add another term to the program.

To solve the Eq. (3-4), fully implicit method is used. Time increment condition in the viscous term when the term is solved explicitly is expressed by the following equation.

$$\Delta t = \frac{\rho(\Delta x)^2 D}{\mu} \tag{3-6}$$

where D represents diffusion number, which the value less than 0.5. As a result, when the spatial increment becomes small, the time step depends on the square, and in the mesoscale calculation, the time increment condition of the viscous term will become rate limiting. In this research, to avoid this, the fully implicit method was used.

In this study, the central difference method was used to discretize the convection term and viscous term of the governing equation. In the central difference method, the point to be calculated is denoted by P, the points on the east and west sides of P are E and W, respectively. The boundary points of the area to be integrated by the finite volume method are e and w. The values of ϕ at points e and w are

$$\phi_{\mathrm{e}} = \frac{1}{2}(\phi_{\mathrm{P}} + \phi_{\mathrm{E}}) \tag{3-7}$$

$$\phi_{\mathrm{w}} = \frac{1}{2}(\phi_{\mathrm{W}} + \phi_{\mathrm{P}}) \tag{3-8}$$

By combining the Eq. (3-7) and Eq. (3-8), ϕ_P can be expressed as

$$\phi_{\mathrm{P}} = \phi_{\mathrm{e}} - \phi_{\mathrm{w}} \tag{3-9}$$

Next, the projection method was used to solve the continuity equation and pressure gradient term in this study. First, taking the divergence of Eq. (3-5).

$$\frac{\nabla \cdot \mathbf{u}^{\mathrm{n+1}} - \nabla \cdot \mathbf{u}^{(2)}}{\Delta t} = \nabla \cdot \left(-\frac{1}{\rho}\nabla p\right) \tag{3-10}$$

From the continuity equation we have

$$\nabla \cdot \mathbf{u}^{\mathrm{n+1}} = 0 \tag{3-11}$$

By Substituting Eq. (11), Eq. (10) become

$$\frac{0 - \nabla \cdot \mathbf{u}^{**}}{\Delta t} = \nabla \cdot \left(-\frac{1}{\rho}\nabla p\right) \tag{3-12}$$

$$\frac{\nabla \cdot \mathbf{u}^{**}}{\Delta t} = \nabla \cdot \left(\frac{1}{\rho}\nabla p\right) \tag{3-13}$$

This equation is Poisson equation. When matrixed, it becomes a triple-diagonal matrix, which can be used with the tridiagonal matrix algorithm (TDMA) and can be regarded as independent equations in x, y and z directions. The pressure can be obtained by the alternative direction implicit (ADI) method which repeats the calculation until the consistency of both side can be obtained. The calculated pressure is used to update the velocity as follows:

$$\mathbf{u}^{n+1} = \mathbf{u}^{**} - \frac{1}{\rho}\nabla p \Delta t \tag{3-14}$$

The spatial gradient of p is obtained using the central difference method.

3.2.3 Immersed boundary method

The Immersed Boundary (IB) method proposed by Kajishima et al. [26], was used to calculate hydrodynamics interaction between solid (filter) and fluid. The calculation in this method is done by modifying the fluid flow velocity based on solid volume fraction in the cell. The volume-averaged velocity **u** is defined as follows:

$$\mathbf{u} = \alpha \mathbf{u}_s + (1-\alpha)\mathbf{u}_f \tag{3-15}$$

where α represents the local volume fraction of solid in the computational cell, $\mathbf{u}_f$ is the fluid velocity, and $\mathbf{u}_s$ is the velocity inside the solid filter. The velocity inside the solid filter is set to be 0.

The time evolution difference equation for Eq. (3-2) is expressed as:

$$\mathbf{u}^{n+1} = \mathbf{u}^{n} + \Delta t\left(-\frac{1}{\rho}\nabla p - \mathbf{u}\cdot\nabla\mathbf{u} + \mu\nabla^2\mathbf{u} + \mathbf{f}\right) \tag{3-16}$$

Where n is the number of time step and Δt is the time increment. Despite the computational cell is located at the fluid (α = 0), solid (α = 1), or at the interface (0<α<1), the velocity is predicted as the fluid motion as the following equation.

$$\hat{\mathbf{u}} = \mathbf{u}^{n} + \Delta t\left(-\frac{1}{\rho}\nabla p - \mathbf{u}\cdot\nabla\mathbf{u} + \mu\nabla^2\mathbf{u}\right) \tag{3-17}$$

The force **f** is introduced to modify the calculated velocity to the desired velocity according to each phase, where **f** is defined as follows:

$$\mathbf{f} = \frac{\alpha(\mathbf{u}_s - \mathbf{u}^*)}{\Delta t} \tag{3-18}$$

where $\mathbf{u}^*$ is the fluid velocity temporarily obtained in each iteration. If the cell is located inside the solid region (α = 1), the velocity is equal to the velocity of the solid. Conversely, if the cell is located within the fluid region (α = 0), the velocity is equal to the local fluid velocity.

3.2.4 Validation of present method

Before conducting the simulation of permeation of air through the fibrous filter, several validation tests have been conducted to know the accuracy of the program. We conducted flow between parallel plates, Rayleigh flow, and flow around a cylinder.

3.2.4.1 Flow between parallel plates

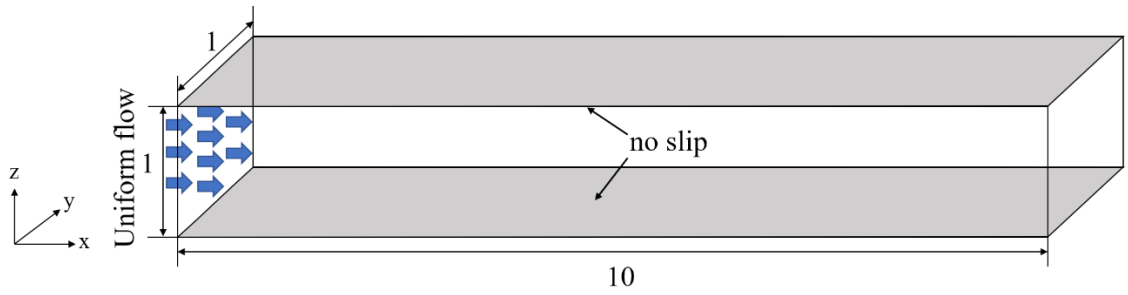

Figure 3.1 Computational domain of flow between parallel plates

Figure 3.1 shows the computational domain of flow between parallel plates in the 3D simulation model. Bottom (z=0) and upper (z=1) boundary were wall surfaces. As an initial condition, uniform flow and uniform pressure were set at the left side boundary (x=0). The value of initial velocity was 1 in the inlet part, the slip-free condition was applied in the wall surface and the value of the outflow was calculated using extrapolation. The Reynolds number was set to be 100. The velocity distribution at steady state condition is shown in **Figure 3.2**.

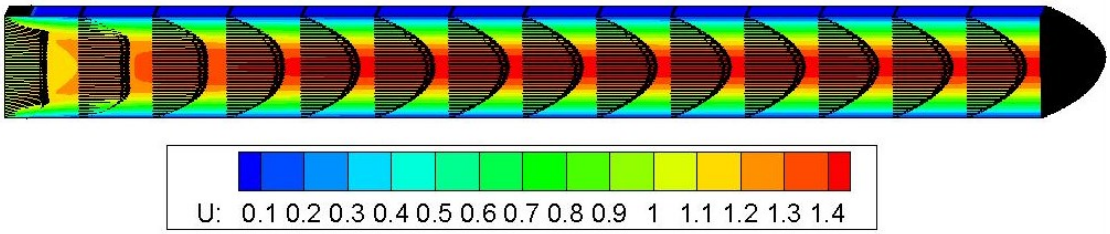

Figure 3.2 Velocity distribution of flow between parallel plates

From the **Figure 3.2**, the result is showing that the Poiseuille flow was formed from the distribution of the velocity vector arrows. It is shown that this program is qualitatively correct. Moreover, the theoretical result for the maximum velocity of the flow between parallel plates at the center of the cross-section is 1.5 times the average velocity of the cross-section. In this case, the average velocity of the cross-section is 1, so the maximum velocity

at the center of the cross-section should be 1.5. As shown in the figure, the velocity at the center of the computational domain is approximately to 1.5, as represent by red color. This result is quantitatively validated our model.

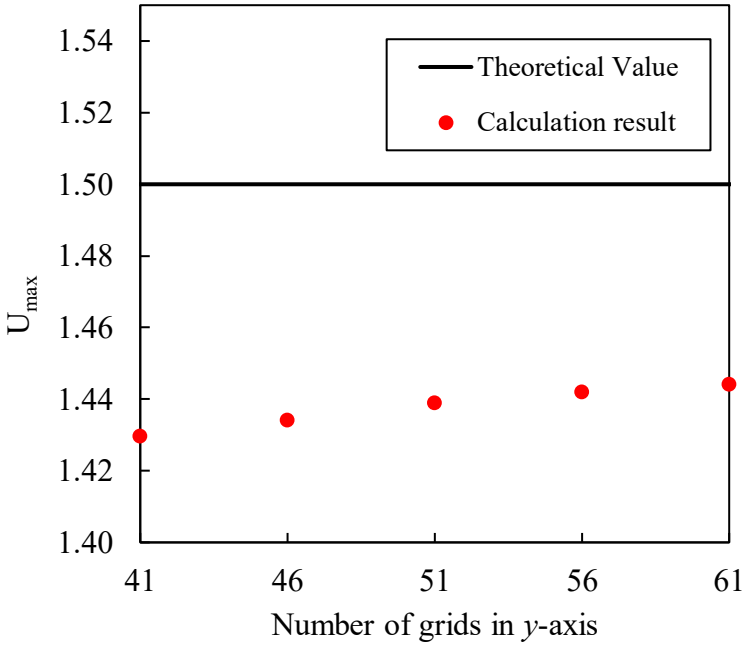

Figure 3.3 Relationship between the number of grids and U_{max}

Figure 3.3 shows the relationship between the number of grids vs the maximum velocity of the flow between parallel plates. From this figure, it shows that the error is decreased by increasing the number of grids until a certain number of grids. It can be concluded that there is almost no grid dependency on the program after a certain number of grids.

3.2.4.2 Rayleigh flow

To verify the unsteady calculation in single-phase flow, a simulation of Rayleigh flow was conducted. Rayleigh flow is a flow generated when a wall surface is instantly moved at a constant speed in a semi-finite region partitioned by one flat wall. Since we cannot deal with the semi-infinite region in computation, we set up a computational domain as shown in **Figure 3.4** and conducted numerical analysis in the non-stationary state.

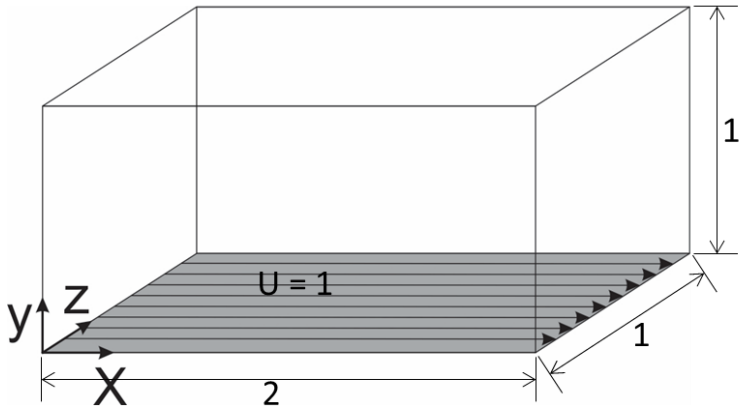

Figure 3.4 Computational domain of Rayleigh flow simulation

The length of the computational domain in the *x*, *y*, and *z* direction was 2×1×1 and equally divided into 80×40×40 grids. The Reynolds number was set to be 100. As the initial condition, velocity (U) at bottom wall ($y = 0$) was set equal to 1, and in another wall, the velocity and pressure were given at 0. The slip-free boundary condition was set at the bottom wall. The boundary conditions at inflow and outflow were applied 0^{th} order extrapolation.

Figure 3.5 shows the velocity distribution of Rayleigh flow simulation at steady state condition. The result showed that due to the influence of the viscosity, the momentum is transported from the wall surface in the direction of the *y*-axis positive direction. The flow has a velocity along the *y*-direction. This result was qualitatively validated our model.

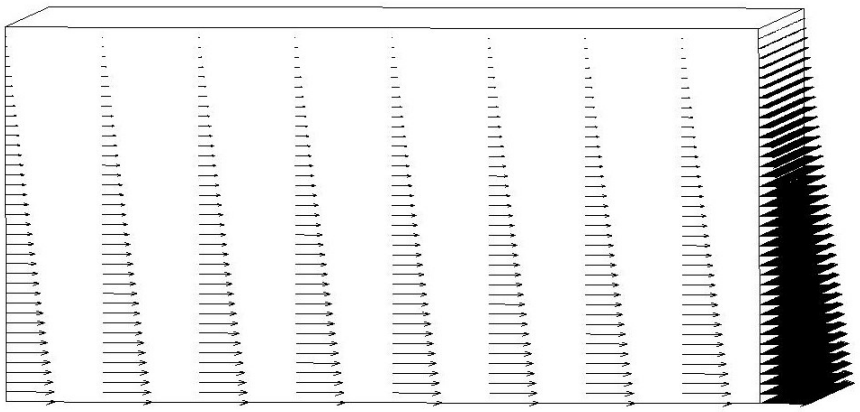

Figure 3.5 Velocity distribution at steady state condition

To carry out quantitative investigations, the temporal change of shear stress acting on the wall surface was compared with a theoretical solution. The results are shown in **Figure**

3.6. The theoretical solution of the shear stress acting on the wall surface is given by the following equation.

$$\mu\left(\frac{\partial u}{\partial y}\right)_{y=0} = -\frac{\rho\sqrt{\nu}U}{\sqrt{\pi}}\frac{1}{\sqrt{t}} \tag{3-19}$$

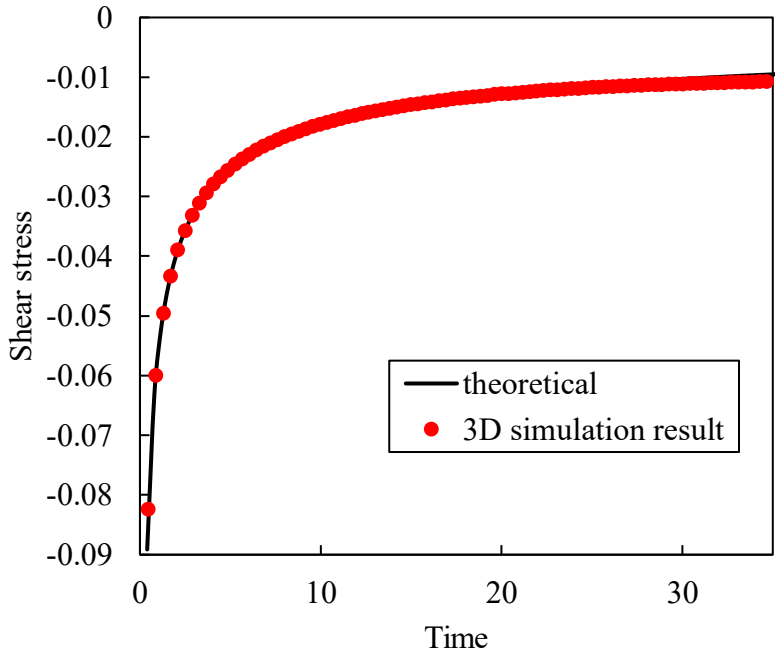

Figure 3.6 Time variation of shear stress acting on the wall

The result showed that calculation result of our model is in good agreement with the theoretical value. It is understood that the unsteady calculation in the CFD program is quantitatively appropriate. From the result, the reliability of unsteady calculation in single-phase flow was obtained.

3.2.4.3 Flow around a cylinder

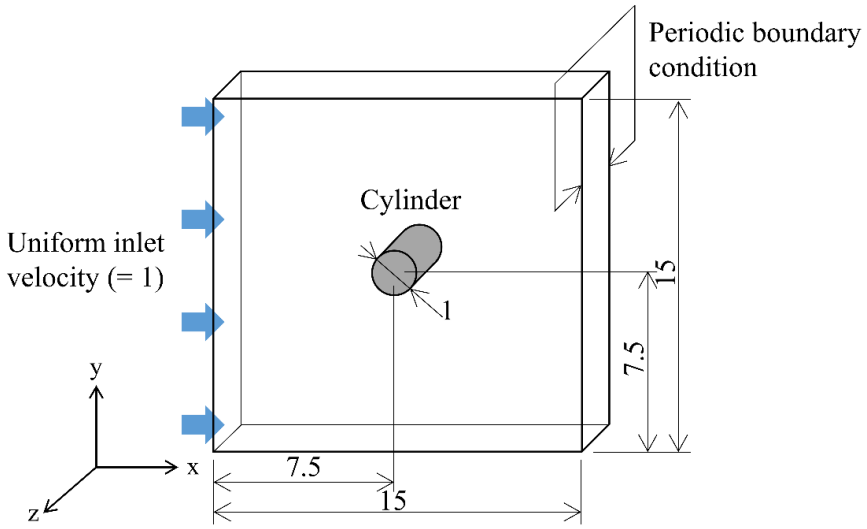

Figure 3.7 Computational domain for simulation of flow around cylinder

The simulation of flow around a single cylinder was also carried out to test the reliability of our numerical framework based on the immersed boundary method. A cylindrical shape was chosen to represent the shape of the fiber. **Figure 3.7** shows the computational domain for the validation. A cylinder with diameter d = 1 was placed in the center of the computational domain. The length of the computational domain in the x and y direction was 15. The number of grids in the x, y, and z-direction were 132, 132, and 67, respectively (n_x = 132, n_y = 132, n_z = 67). The periodic boundary condition was applied in the z direction. The uniform inlet velocity U_{in} was set to 1 at the left boundary. The calculation continued until a steady state was reached. The simulation was performed with various Reynolds numbers. For each case, the fluid viscosity was tuned to achieve the desired flow regime that was characterized by the Reynolds number Re:

$$\text{Re} = \frac{\rho U_{\text{in}} d}{\mu} \qquad (3\text{-}20)$$

Figure 3.8 presents the cross-sectional (a) velocity and (b) pressure contours of flow around a cylinder at a steady state condition with the Reynolds number Re = 5. **Figure 3.8(a)** shows that the velocity of the fluid is approximately zero inside the cylinder, showing that the immersed boundary method successfully described the solid boundary. **Figure 3.8(b)** shows that the pressure is high in front of the cylinder then significantly decreases in the direction of the main flow, indicating that a pressure drop occurs due to the existence of the cylinder. Thus, the constructed numerical simulation model can reasonably describe the flow and pressure drop around cylindrical obstacles such as a fibrous filter.

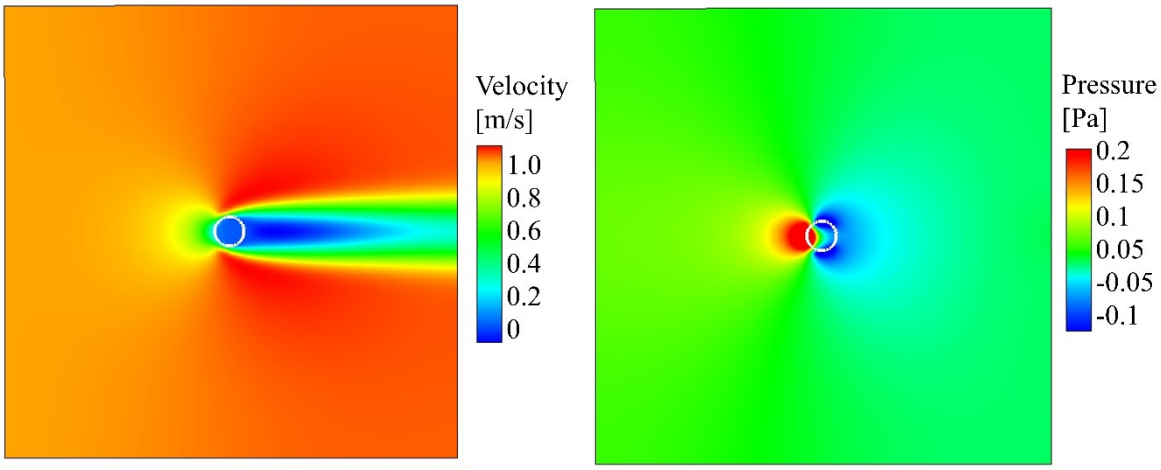

Figure 3.8 Cross-sectional (a) velocity and (b) pressure contours of flow around cylinder when Re = 5

The relationship between the Reynolds number and the drag coefficient was investigated to check the accuracy of the simulation model quantitatively. The drag coefficient was calculated from the drag force from the simulation results as follows:

$$C_{\mathrm{d}} = \frac{2F_{\mathrm{d}}}{\rho U_{\mathrm{in}}^2 A} \tag{3-21}$$

where C_{d} is the drag coefficient, F_{d} is the drag force, and A is the projected area of the cylinder. Based on the immersed boundary method, the drag force acting on the solid can be easily obtained by integrating the interaction between solid and fluid **f** over the solid volume as follows:

$$F_{\mathrm{d}} = -\rho \int_{V_{\mathrm{s}}} \mathbf{f}\, \mathrm{d}V \tag{3-22}$$

where V_{s} is the solid volume. **Figure 3.9** presents the relationship between the drag coefficient and the Reynolds number with a comparison of the drag coefficient calculated using the present method with the experimental results of Tritton et al. [31]. The results show that they are in good agreement over a wide range of the Reynolds numbers with an error below 5%. This result indicates that the present method gives accurate simulation results.

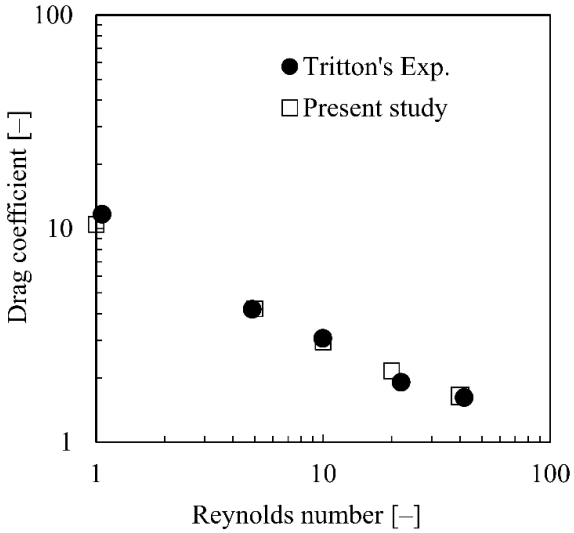

Figure 3.9 Drag coefficient as a function of Reynolds number

3.2.5 X-ray CT images

Direct numerical simulations were performed on commercial PPS (Procon, Toyobo Co., Ltd) and PI (P84, Toyobo Co., Ltd) nonwoven fabric filters. To create realistic morphologies, we scanned both fibrous filters using a high-resolution X-ray CT system (TDM1000H-Sμ, Yamato Science Co., Ltd). The principle of this system is to represent the filter as a stack of layers (**Figure 3.10a**), and each layer is then converted to a grayscale image. The samples were scanned at an energy level of 30 kV and 0.075 mA. The dimensions of the X-ray CT image results were 1024 pixels × 1024 pixels, with a pixel size of 0.78 μm.

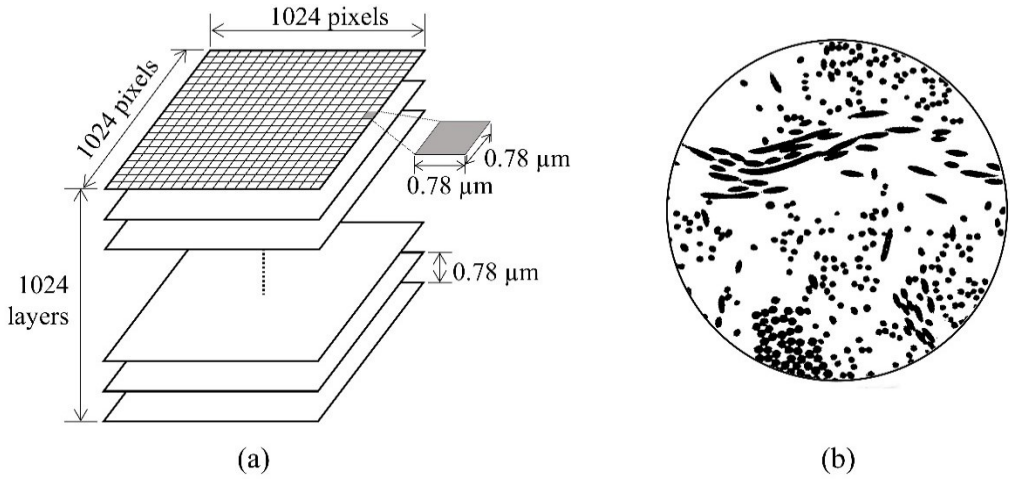

Figure 3.10 (a) Schematic illustration of X-ray Computed Tomography process and (b) representative binary image of a layer

Several further processes were carried out on the X-ray CT images results. First, noise reduction, inverting, and thresholding processes were conducted with Adobe Photoshop.

Then, the binary images (**Figure 3.10b**) were smoothed and converted to text file data using the Image J/Fiji software platform [32]. The text file data contained a combination of numbers in the range of 0 to 255 according to the color brightness of the image. Solid fiber, which was black in color, was represented by 0, while void space, which was white in color, was represented by 255. In the immersed boundary method, the evaluation of the solid volume fraction (α) is very important. Regarding the arbitrary-shape wall model in staggered grids, some researchers have applied the signed distance function (SDF) to determine the value of α[33,34]. The SDF value of a given point is determined by the minimum distance from the point to the surface of the wall. The value will be negative inside the wall and vice versa. In this study, we used the linear transformation of the text file data to determine the value of the solid volume fraction (α) used for the immersed boundary method. The value of α in a cell was calculated using:

$$\alpha = \frac{B_w - B}{B_w - B_b} \tag{3-23}$$

where B_w is the white color value, B_b is the black color value, and B is the value of the color brightness in the cell. If the value of color brightness is small, the value of α will approach 1, which represents the solid zone. In contrast, if the value of the color brightness is high, the value of α will approach 0, which represents the fluid zone. We constructed the filter domain using voxel data, with dimensions of 156 × 156 × 78 μm corresponding to the x, y, and z directions, respectively. It should be noted that the size of the filter domain was kept small to reduce the simulation time, and thus, the arrangement and porosity of fibers varied considerably with their locations in the actual filter. This variation may significantly affect the pressure drop within the filter. Here, we prepared six filter domains with a different porosity for each filter type by selecting a small part randomly from the X-ray CT image to correspond to the unbalanced fiber arrangement in a filter. The porosity of the filter domain was determined by the volume of the voids in the filter domain divided by the total volume of the filter domain using:

$$\varepsilon = \frac{\sum(1-\alpha)\Delta\Theta}{\sum\Delta\Theta} \tag{3-24}$$

where ε is the porosity and $\Delta\Theta$ is the cell volume, and the summation is taken for all the computational cells. The visualizations of the modeled filters with different porosities for both types of filters are presented in **Figure 3.11**.

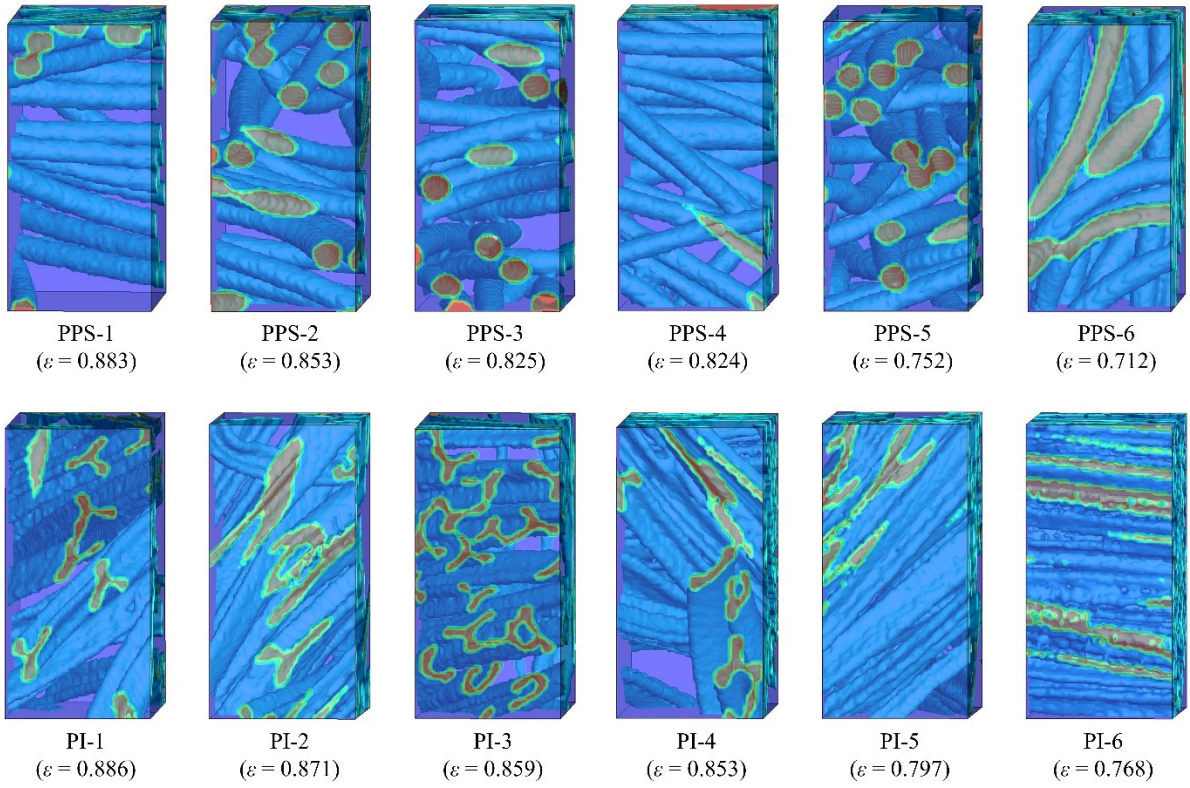

Figure 3.11 PPS and PI filter domains created from X-ray CT images

3.2.6 Simulation details

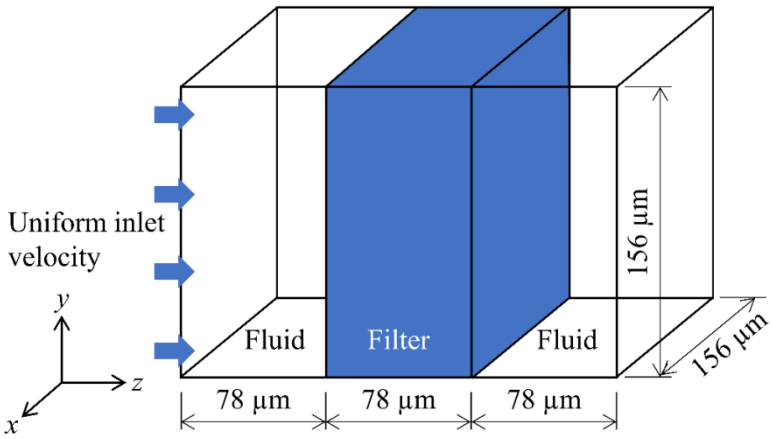

Figure 3.12 Computational domain for simulation of permeation through a filter

Figure 3.12 shows the computational domain used to simulate the permeation of gas through the realistic fibrous filter created by X-ray CT. The computational domain was divided into three sub-domains of the same size, which were the fluid domains in front of and behind the filter, and the filter domain created by the X-ray CT image. The size of the computational domain was 156 × 156 × 234 µm in the *x*, *y*, and *z* directions, respectively.

The main flow direction was set according to the flow along the *z*-axis. The flow field was divided into 100 × 100 × 150 cells in the *x*, *y*, and *z* directions, respectively (n_x = 100, n_y = 100, n_z = 150). A uniform flow was set at the inlet boundary (z = 0) with the specified superficial velocity. The inlet velocity was varied between 0.05 m/s and 0.125 m/s. At the right (outlet) boundary, the velocity was calculated by the Neumann condition, and the pressure was set to 0. The other boundaries were modeled as slip walls. The difference between the average pressure at the inlet boundary and the outlet boundary defined the pressure drop in this study. The density and viscosity of the fluid were set at constant values of 1.25 kg/m^3 and 1.76×10^{-5} Pa·s, respectively. Nitrogen gas at a temperature of 298.15 K was used as the fluid in this simulation. This fluid was employed in the experiment explained below. The physical properties of nitrogen gas and the detailed simulation conditions are given in **Table 3-1**.

Table 3-1 Conditions for simulations of gas permeation through a filter

$n_x \times n_y \times n_z$	100 × 100 × 150
Fluid density	1.25 kg/m^3
Fluid viscosity	1.76 × 10^{-5} Pa·s
Superficial velocity	0.05, 0.075, 0.1, 0.125 m/s

3.2.7 Experimental pressure drop measurement

An experiment was performed to measure the pressure drop across a fibrous filter and to compare this measurement with the simulation results. A schematic of the pressure drop measurement is given in **Figure 3.13**. A sample of the fibrous filter with dimensions of 25 × 10.5 cm was placed in the exposure chamber, and nitrogen gas fed from a gas cylinder flowed through the filter. The experiment was carried out at a temperature of 25 ± 3 °C. The flow rate was controlled by a mass flow controller (KOFLOC 8500; Kojima Instruments Inc.) within 0.05–0.133 m/s. The pressure drop across the filter cloth was measured using an inclined manometer (KM-306, Okano works, Ltd). The experimental conditions are given in **Table 3-2**. The porosity of the filter was measured using the specific gravity and mass of a sample filter measuring 3 × 3 cm. The thicknesses of the PPS and PI filters were 1.76 mm and 1.83 mm, respectively. Each experiment was conducted three times for each fibrous filter, and the average value was used in this study.

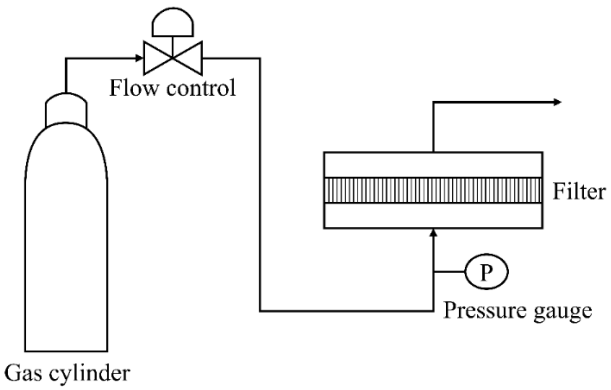

Figure 3.13 Experimental setup for measurement of pressure drop for nitrogen gas passing through a filter

Table 3-2 Experimental conditions

Fluid	Nitrogen
Temperature	20 ± 3 ˚C
Superficial velocity	0.05, 0.067, 0.083, 0.100, 0.117, 0.133 m/s

3.3 Results and Discussion

3.3.1 Investigation of the length of approach zone

It is important to confirm if the fluid flow is fully developed in the filter simulation. A simulation of PPS-2 (ε = 0.853) filter domain with several lengths of approach zone was carried out to show that the present approach zone was enough to develop the fluid flow. We compare the present approach zone with the length of 78 μm, with longer and shorter approach zones with the lengths of 117 μm and 39 μm, respectively. The simulation conditions are the same as with present conditions with the inlet velocity of 0.1 m/s. **Figure 3.14** presents the comparison of pressure contours with three approach zones. It is shown that the pressure drop in the shorter approach zone was significantly higher than the present result, while the longer approach zone gave an almost similar result with the present results. The calculated pressure drops of the shorter approach zone, present approach zone, and longer approach zone were 16.74 Pa/mm, 14.66 Pa/mm, and 14.27 Pa/mm, respectively. This result indicated that the length of the present approach zone was enough to develop the fluid flow in this simulation.

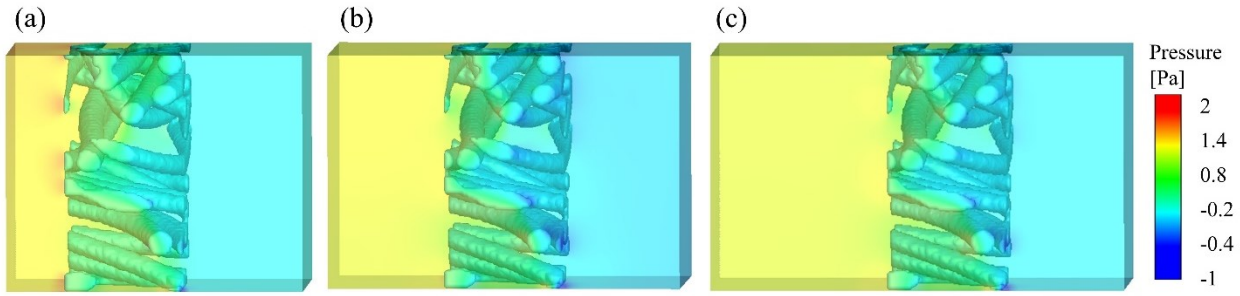

Figure 3.14 Pressure contours of PPS-2 with various approach zones (a) shorter, (b) present, and (c) longer approach zones

3.3.2 Comparison between PPS and PI filter pressure drops

A comparison between the PPS and the PI filter pressure drops was conducted. Based on the product information for the PPS and PI filters[35,36], the fiber shapes of PPS and PI are different. The shape of the PPS fiber is round, whereas the PI fiber has a trilobal shape. The average diameters of these PPS and PI fibers are 15 μm and 18 μm, respectively. The effect of the fiber shape on pressure drop was therefore investigated in this study.

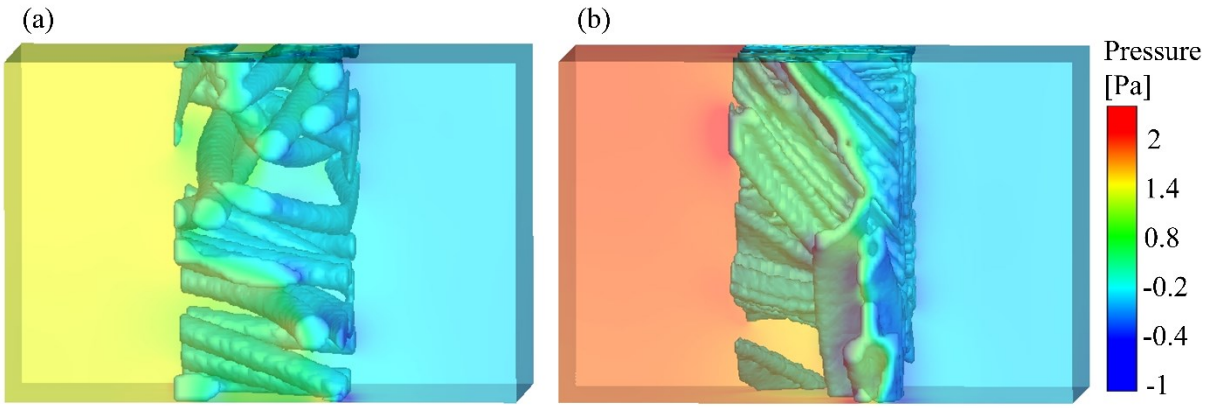

Figure 3.15 Pressure contours of (a) PPS and (b) PI filters with the same porosity (ε = 0.853)

We conducted a simulation of gas flowing through PPS and PI filters having the same filter porosity. PPS-2 and PI-4 were used as the filter domains because they both had the same filter porosity, ε = 0.853. **Figures 3.15(a)** and **3.15(b)** show the pressure contours of the PPS and PI filters in the steady state with a superficial velocity of 0.1 m/s, respectively. The pressure in front of the filter domain was high, and then it significantly decreased inside the filter along the main flow direction. This result indicates that the pressure drop occurred owing to the presence of the filter. In addition, the pressure in front of the filter domain for

the PI filter was higher than that for the PPS filter. From this observation, the pressure drop for the PI filter was qualitatively higher than the PPS filter for filters with equivalent porosity.

Figure 3.16 presents a comparison between the calculated pressure drop per unit thickness of the PPS and PI filters having the same porosity according to the superficial velocity. When the superficial velocity was set to 0.05 m/s, the pressure drops of the PPS and PI filters were 7.29 Pa/mm and 11.37 Pa/mm, respectively. When the superficial velocity was increased to 0.075 m/s, the pressure drops increased to 10.98 Pa/mm and 17.07 Pa/mm, respectively. As the superficial velocity was increased, the pressure drops of both filters displayed a linear increasing trend. This result matches the experimental results reported by Wang et al. [37], Bian et al. [38], and Xia et al. [39]. **Figure 3.16** also shows that the pressure drop in the PI filter was higher than the pressure drop in the PPS filter for all velocities. In addition to quantifying the pressure contour results (as shown in **Figure 3.15**), this result further confirmed that the PI filter produced a higher pressure drop than the PPS filter.

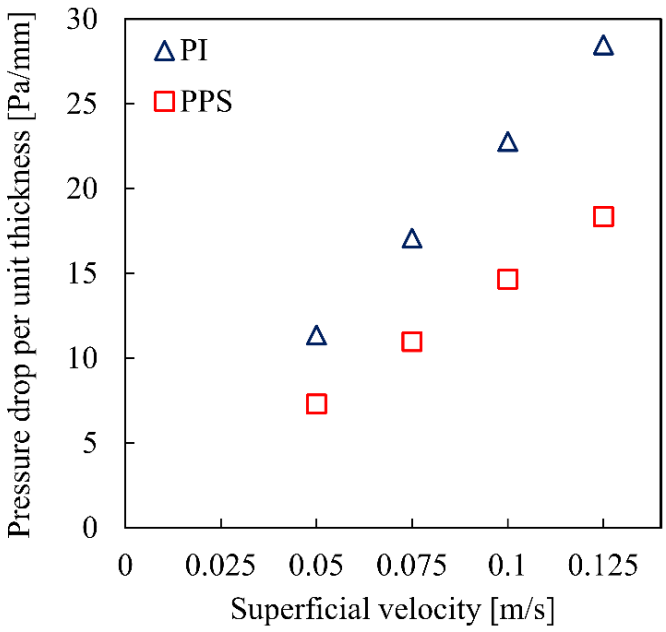

Figure 3.16 Comparison of pressure drop between PPS and PI filters with the same porosity ($\varepsilon = 0.853$) as a function of superficial velocity

3.3.3 *Effect of filter porosity on the pressure drop*

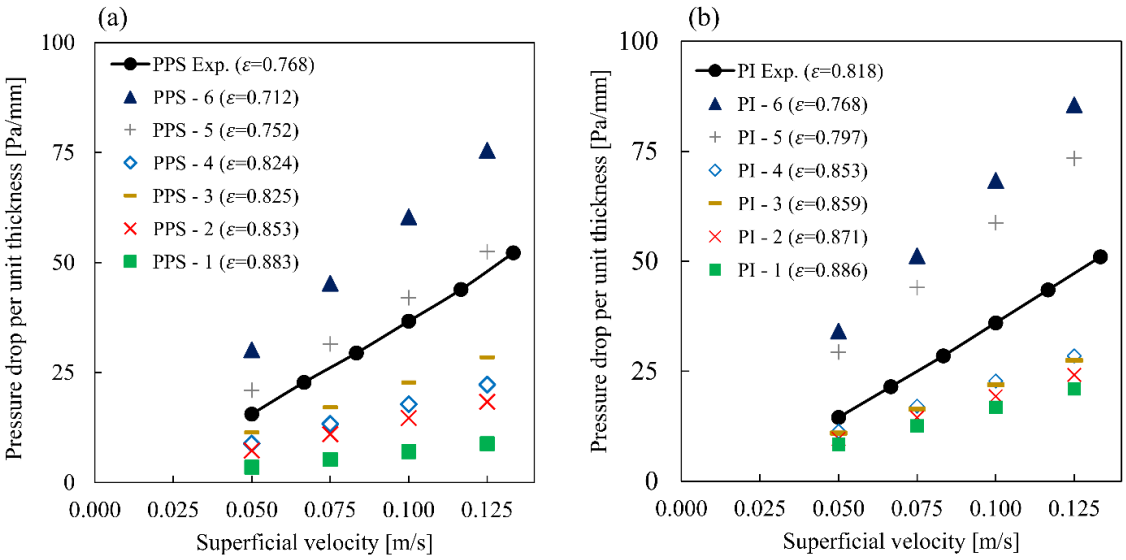

Figure 3.17 Effect of superficial velocity on pressure drop of (a) PPS and (b) PI filters with various porosities

The effect of filter porosity on the pressure drop was investigated by conducting a simulation with gas flowing through PPS and PI filters with various porosities. The porosity and calculated surface area of each filter domain are presented in **Table 3-3**. **Figure 3.17** illustrates the relationship between the calculated pressure drop per unit thickness and the superficial velocity at various porosities. As depicted in Figure **3.17(a)**, at the superficial velocity of 0.05 m/s, the pressure drops of PPS-1 (ε = 0.883) and PPS-6 (ε = 0.712) were 3.49 Pa/mm and 30.16 Pa/mm, respectively. In **Figure 3.17(b)** at the same velocity, the pressure drops of PI-1 (ε = 0.886) and PI-6 (ε = 0.768) were 8.36 Pa/mm and 34.13 Pa/mm, respectively. PPS-1 and PI-1 were the filter simulation domains with the highest porosity for each type of filter. Contrarily, PPS-6 and PI-6 were the domains with the lowest porosity. It was found that the pressure drop across the filter increased with a decrease in porosity. This can be explained by the fact that with decreasing filter porosity, the effective pore size for fluid flow decreased, and the surface area of the filter increased[40]. This led to an increase in the flow resistance of the filter, which resulted in an increase in the pressure drop[41].

Table 3-3 Calculated porosity and surface area for simulated filter domains

Filter	Porosity	Surface area [$\times 10^{-7}$ m^2]
PPS-1	0.883	1.28
PPS-2	0.853	1.77
PPS-3	0.825	2.10
PPS-4	0.824	2.13
PPS-5	0.752	2.47
PPS-6	0.712	2.75
PI-1	0.886	1.59
PI-2	0.871	1.70
PI-3	0.859	1.99
PI-4	0.853	2.20
PI-5	0.797	2.79
PI-6	0.768	3.58

The black line in each figure represents the experimental results for each filter. For the PPS filter, the experimental result ($\varepsilon = 0.768$) was located between the results of PPS-4 ($\varepsilon = 0.825$) and PPS-5 ($\varepsilon = 0.752$). For the PI filter, the experimental result ($\varepsilon = 0.818$) was located between the results of PI-4 ($\varepsilon = 0.853$) and PI-5 ($\varepsilon = 0.797$). Both results were also consistent with the order of filter porosities. The reliability of the simulation results was qualitatively proven by this result.

A number of previous studies have been carried out toward developing pressure drop relationships in a fibrous network. Davies[42] proposed an empirical formula to calculate the pressure drop in realistic fibrous filtration. Happel[11] used the free-surface model to predict the resistance to flow in assemblages of spherical particles and in the flow relative to cylinders. Flows parallel to cylinders and perpendicular to cylinders were simulated in the study. Drummond[43] simulated laminar viscous flow through regular arrays of parallel solid cylinders and calculated the pressure drops. Very recently, Yang et al[12] proposed a

predictive model to calculate the pressure drop across combined polydisperse spherical particle-cylindrical fiber networks. They developed an expression relating $\frac{dp^*}{dz^*}$ to both *Re* and the microstructure of fiber and fiber-particle networks. Their proposed expression is

$$\frac{dp^*}{dz^*}Re = 13.48\left(1-\varepsilon+V_{\mathrm{p}}\right)+85.94\frac{\left(1-\varepsilon+V_{\mathrm{p}}\right)^2}{\left(\varepsilon-V_{\mathrm{p}}\right)^3} \qquad (3\text{-}25)$$

where $\frac{dp^*}{dz^*}$ represents the dimensionless pressure drop per unit length, *Re* is the Reynolds number, ε is the filter porosity, and V_{p} is the particle solidity. Yang et al.[12] also provided an expression resulting from the non-dimensionless results proposed by Davies[42], Happel[11], and Drummond[43]. The expressions from Davies's study, Happel's study for flow parallel to cylinders, Happel's study for flow perpendicular to cylinders, and Drummond's study are respectively shown below:

Davies $$\frac{dp^*}{dz^*}Re = 64(1-\varepsilon)^{1.5}[1+56(1-\varepsilon)^3] \qquad (3\text{-}26)$$

Parallel to cylinder $$\frac{dp^*}{dz^*}Re = \frac{32(1-\varepsilon)}{\ln\left(\frac{1}{1-\varepsilon}\right)+\frac{1-(1-\varepsilon)^2}{1+(1-\varepsilon)^2}} \qquad (3\text{-}27)$$

Perpendicular to cylinder $$\frac{dp^*}{dz^*}Re = \frac{32}{3+\varepsilon-\frac{3}{1-\varepsilon}+\frac{2}{1-\varepsilon}\ln\left(\frac{1}{1-\varepsilon}\right)} \qquad (3\text{-}28)$$

Drummond's $$\frac{dp^*}{dz^*}Re = \frac{32(1-\varepsilon)}{\ln\left(\frac{1}{1-\varepsilon}\right)-1.476+2(1-\varepsilon)-1.774(1-\varepsilon)^2} \qquad (3\text{-}29)$$

The dimensionless pressure drop per unit length ($\frac{dp^*}{dz^*}$) in our study was calculated by equation below:

$$\frac{dp^*}{dz^*} = \frac{(p_{\mathrm{in}}-p_{\mathrm{out}})}{L}\frac{D_{\mathrm{fiber}}}{\rho U^2} \qquad (3\text{-}30)$$

where p_{in} represents the pressure in the inlet boundary, p_{out} is the pressure in the outlet boundary, L is the length of filter domain, D_{fiber} is the diameter of the fiber, ρ is the fluid density, and U is the superficial velocity of the fluid. To calculate the Reynolds number, we used the average diameter of each fiber and the density, viscosity, and superficial velocity of the fluid in each case.

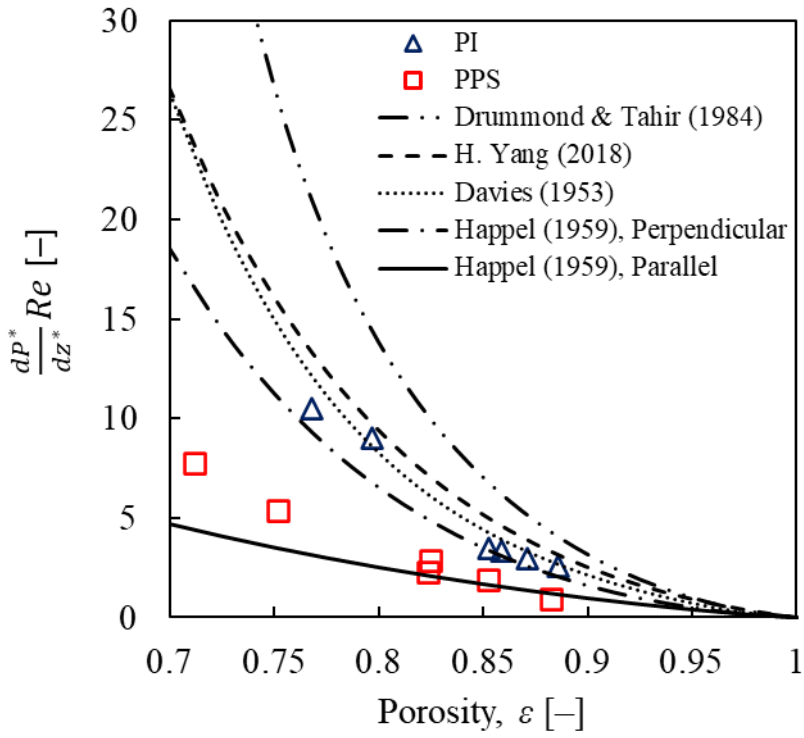

Figure 3.18 Comparison of present simulation results with existing models

The comparison of the present simulation results and the prediction model results proposed by Davies[42], Happel[11], Drummond[43], and Yang[12] is plotted in **Figure 3.18**. The product of the dimensionless pressure drop per unit length and Reynolds number ($\frac{dp^*}{dz^*}Re$) is plotted against the porosity of the filter (ε). The results show that in the high porous filter (PPS-1–4), the PPS filter results fit the results from Happel[11] for flow parallel to cylinders. This is because the arrangement of fibers in the PPS-1 to PPS-4 filters was mostly parallel to the main flow direction, as shown in **Figure 3.2**. The PPS-5 and PPS-6 results were located between Happel's results[11] for flow parallel and perpendicular to cylinders, probably because the fibers were arranged in parallel and perpendicular combinations to the main flow direction. For the PI filter, the results closely agreed with the results from Davies[42] and Yang et al[12]. This result is reasonable because the PI filter has an irregular arrangement and complex geometry, which was the case for the filter structures evaluated by Davies[42] and Yang et al[12]. These results quantitatively support the reliability of the present simulation results.

3.3.4 Flow characteristics in porous media

The permeation of fluid in porous filter media is characterized by Darcy's law[27], which describes the relationship between the average (macroscopic) velocity and the fluid macroscopic pressure drop through a porous medium. Eq. (3-31) is the one-dimensional form of Darcy's law:

$$J = \frac{K\Delta p}{\mu L} \tag{3-31}$$

where J is the permeation flux, which is the same as the superficial velocity in this study, K is the permeability, Δp is the pressure drop, and L is the filter thickness. Permeability K denotes the capability of a porous material to allow fluid flow, which depends on the microstructure of the solid phase in the porous media and is independent of the fluid properties.

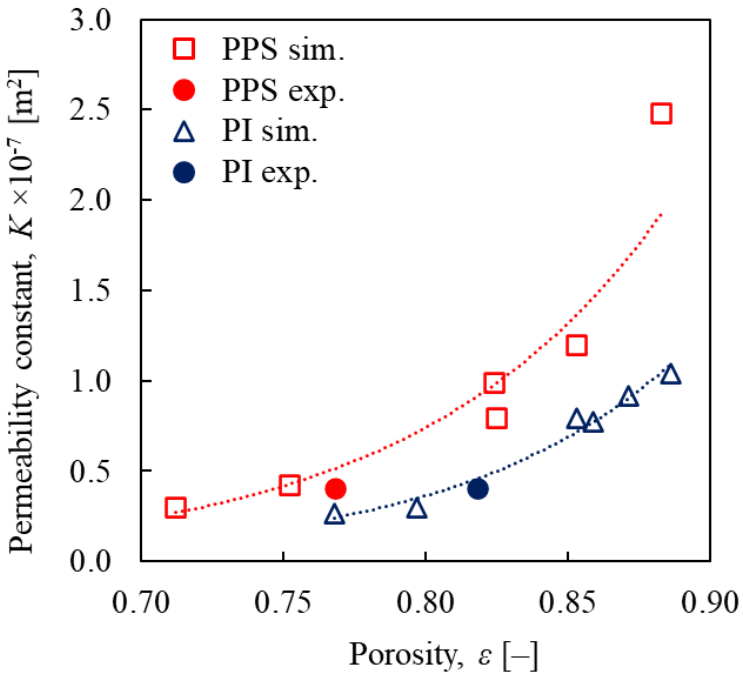

Figure 3.19 Relationship between porosity and permeability

The change in permeability as a function of porosity is shown for both filters in **Figure 3.19**. The permeability increased with an increase in the porosity for both filters. Non-linearity was observed for the permeability-porosity relationship. The slope increased with an increase in the porosity. This trend is consistent with those reported by Feng and Weinbaum[44], Crawford et al.[45], and Zhu et al.[46]. The permeabilities obtained from the simulation results deviated slightly from the trend line in both filters. This was probably

due to the complexity of the fiber arrangement. The fiber arrangement varied significantly for each domain. Although the fiber arrangement affects the pressure drop, the effect of porosity is more significant, as shown in these results. The experimental results of each filter are also plotted in **Figure 3.19**, where the experimental results for the permeability of both filters are correlated with the trend line, and indicate that the present simulation method is quantitatively reliable.

To investigate the reason why the permeability of the PPS filter was higher than that of the PI filter as shown in **Figure 3.19**, and why the pressure drop of the PPS filter was lower than that of the PI filter as shown in **Figure 3.16**, the flow around a single fiber was simulated. We performed the same processes used to create a filter domain to create a single fiber. The cross-sectional shape of each fiber was isolated from an X-ray CT image. The fiber being evaluated was located at the center of the *y*-*z* plane and was then pulled in the *x* direction. The dimensions of the computational domain in the *y* and *z* directions were 312 μm for each axis, and 78 μm in the *x* direction. A periodic boundary condition was applied in the *x* direction. The uniform inlet velocity was set to 0.1 m/s at the left boundary (z = 0). The pressure at the outlet boundary (z = 312 μm) was set to 0. The calculations continued until a steady state was reached.

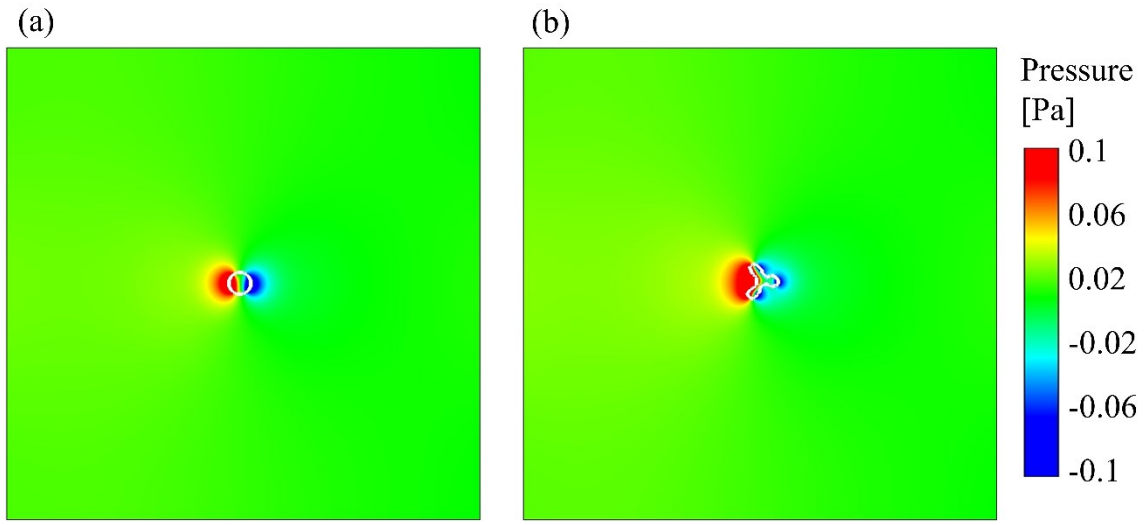

Figure 3.20 Pressure contours around (a) PPS and (b) PI single fibers for an inlet velocity of 0.1 m/s

Figure 3.20 shows a comparison of the pressure contours around single PPS and PI fibers. As shown in these contours, the pressure in front of the PI fiber was higher than for the PPS fiber. In addition, the drag forces acting on the PI and PPS fibers were 8.26×10^{-10}

N and 6.88×10^{-10} N, respectively, quantitatively showing that the drag force for the PI fiber was higher than for the PPS fiber. This was probably due to differences in the cross-sectional shapes. It was considered that this drag force difference between the two types of fibers contributed to the permeability difference between the two types of filters, as shown in **Figure 3.19**. From this result, we confirmed that the permeability of a filter was influenced not only by its porosity but also by the shape of its fibers.

3.3.5 Kozeny constant

Permeability and porosity have a close relationship that depends on the amount of void space in the material. The permeability may also be influenced by the complexity of the flow path inside the porous media. A common equation used to determine the permeability of porous media is the Kozeny–Carman equation[28,29], which estimates the flow resistivity in laminar flow. The Kozeny–Carman equation is given by

$$\frac{\Delta p}{L} = k\frac{(1-\varepsilon)^2}{\varepsilon^3}\mu {S_v}^2 u \tag{3-32}$$

where k is the Kozeny constant, ε is the porosity of the filter, S_v is the surface area per unit solid volume, and u is the superficial velocity. The Kozeny–Carman equation indicates that the velocity is proportional to the pressure drop and is inversely proportional to the fluid viscosity[47]. The Kozeny–Carman equation has been applied to evaluate the flow resistivity of various filters in previous research[48–50].

The Kozeny constant in Eq. (3-32) is a dimensionless value that represents the flow characteristics in particle bed and porous media, which are correlated with the shape of the flow path. The determination of the Kozeny constant is crucial for practical applications in a porous medium, and it should be a known value[51]. However, it is difficult to obtain the value of the Kozeny constant using experimental approaches because accurate measurement of the filter surface area is required. In this study, we estimate the value of the Kozeny constant numerically instead. The surface area per unit solid volume of the filter is calculated numerically using the local volume fraction of the solid (α) defined by the immersed boundary method as

$$S_v = \frac{A_s}{V_s} = \frac{\sum \delta \Delta\Theta}{\sum \alpha \Delta\Theta} = \frac{\sum |\nabla\alpha| \Delta\Theta}{\sum \alpha \Delta\Theta} \tag{3-33}$$

where A_s and V_s are the surface area and volume of the filter domain, respectively. δ is the delta function given by $\delta = |\nabla\alpha|$. A summation is taken for all the computational cells. By

using the immersed boundary method, the surface area of a fibrous filter having a complicated fiber arrangement can be estimated. Consequently, by introducing the surface area per unit solid volume, conditions such as porosity, viscosity, and superficial velocity, and the resultant pressure drop per filter thickness into Eq. (3-32), the Kozeny constant can be obtained.

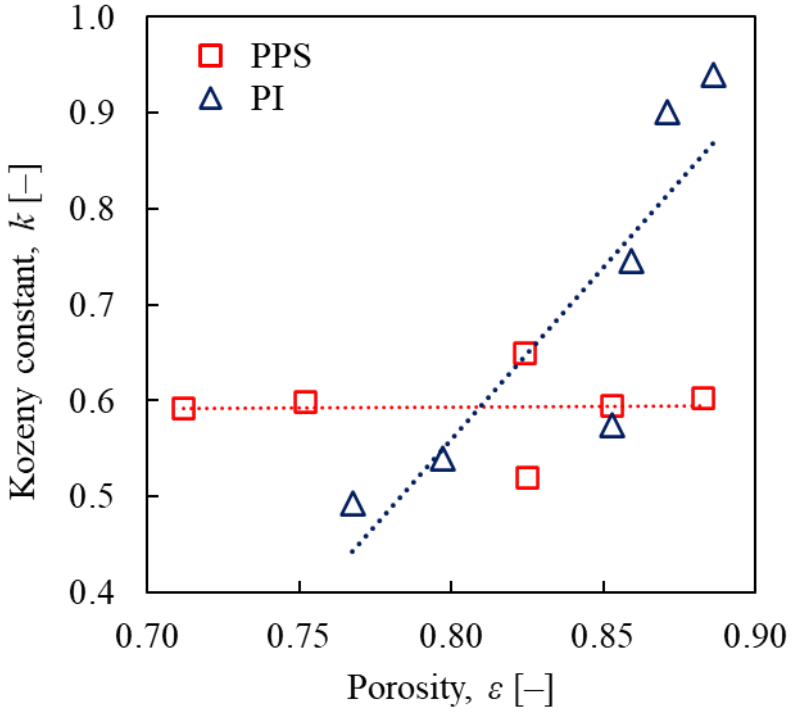

Figure 3.21 Kozeny constant as a function of porosity for each filter domain

The Kozeny constant as a function of filter porosity is shown in **Figure 3.21** and indicates that the change in porosity did not affect the Kozeny constant (~ 0.60) in the PPS filter. On the other hand, interestingly, the Kozeny constant of the PI filter increased with increasing filter porosity. The value of the Kozeny constant was high in the high porosity region, and vice versa. This difference may have been caused by the different flow paths between the two filter domains because of the different arrangements of the fibers. This trend agrees with the study reported by Ozgumus et al. [51].

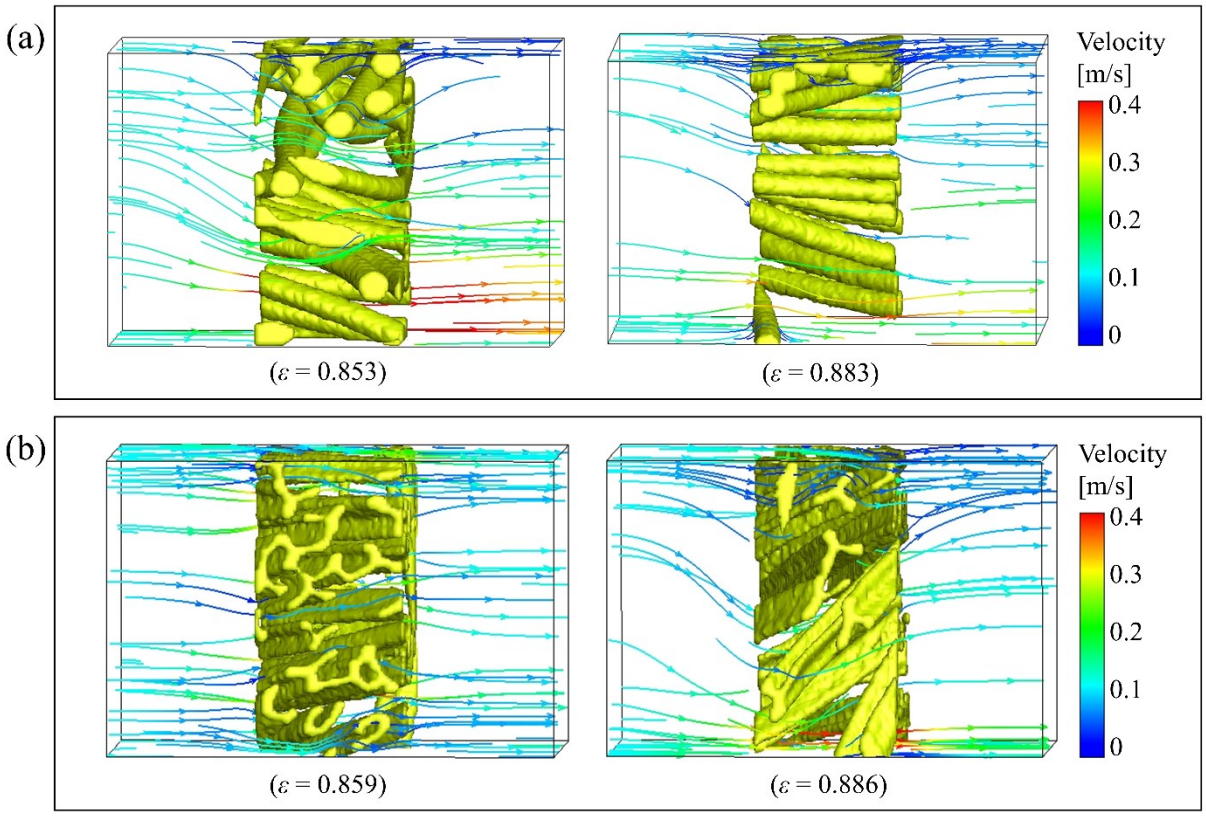

Figure 3.22 Effect of porosity on streamlines for (a) PPS and (b) PI filter

One of the most important parameters in the determination of the Kozeny constant is tortuosity. As an assumption of the Kozeny–Carman equation, tortuosity is defined as the ratio of the length of the flow path in a porous medium to the length of the flow path in the absence of the porous medium[51]. **Figure 3.22** compares the streamlines of different porosities for both filters. In **Figure 3.22 (a)**, the streamlines inside the filter media of PPS-2 ($\varepsilon = 0.853$) were similar to those of PPS-1 ($\varepsilon = 0.883$). Thus, it is assumed that the tortuosity was also similar for both porosities, whereas in **Figure 3.22 (b)**, the streamlines inside the filter domain of PI-3 ($\varepsilon = 0.859$) were shorter than those of PI-1 ($\varepsilon = 0.886$). These results can be used to qualitatively describe the results shown in **Figure 3.21**. Importantly, we can quantitatively estimate the value of the Kozeny constant using the present method, in particular, the calculation of surface area per unit solid volume. This data is very useful for practical applications using porous mediums.

3.4 Conclusions

In this study, we constructed a 3D numerical simulation model to investigate the permeation of gas through a fibrous filter. This model is based on CFD and the immersed boundary method and was used to consider the hydrodynamic interactions between a fluid

and solid. The X-ray CT images of polyphenylene sulfide (PPS) and polyimide (PI) filters were used to construct realistic geometries of the filter domains. Several filter domains with different porosities were simulated for various superficial velocities. The relationships among filter porosity, superficial velocity, and pressure drop of the filter were investigated. The following conclusions can be drawn from the results.

1. The effects of superficial velocity, filter porosity, and type of filter on the pressure drop were investigated and analyzed based on Darcy's law. The predictions from our numerical method were quantitatively in good agreement with our experimental measurements.

2. The permeability of the PI filter was lower than the PPS filter under the same porosity conditions. Utilizing our simulation method, we clarified that the reason was that the drag force acting on a single PI fiber was higher than on a single PPS fiber.

3. The Kozeny constant of the PPS filter was unaffected by changes in filter porosity, retaining a value of approximately $k = 0.6$, while the Kozeny constant of the PI filter was significantly affected by the filter porosity.

It is important to note that the pressure drop that occurred across the filter was also affected by particle deposition during the filtration process for the bag-type filters evaluated in this study. Thus, future work should introduce particle motion to further clarify the permeation process of a nonwoven fibrous filter.

References

[1] J. Steffens, J.R. Coury, Collection efficiency of fiber filters operating on the removal of nano-sized aerosol particles: I-Homogeneous fibers, Sep. Purif. Technol. 58 (2007) 99–105. https://doi.org/10.1016/j.seppur.2007.07.011.

[2] N. Mao, Y. Yao, M. Hata, M. Wada, C. Kanaoka, Comparison of filter cleaning performance between VDI and JIS testing rigs for cleanable fabric filter, Powder Technol. 180 (2008) 109–114. https://doi.org/10.1016/j.powtec.2007.03.017.

[3] L.W. Shacklette, R.L. Elsenbaumer, R.R. Chance, H. Eckhardt, J.E. Frommer, R.H. Baughman, Conducting complexes of polyphenylene sulfides, J. Chem. Phys. 75 (1981) 1919–1927. https://doi.org/10.1063/1.442217.

[4] F. Bertinelli, P.C. Bizzarri, C. Della Casa, S. Saltini, Poly(m-phenylene disulfide):

Antimony pentafluoride doping and infrared spectroscopy, J. Polym. Sci. Part B Polym. Phys. 24 (1986) 2197–2208. https://doi.org/10.1002/polb.1986.090241004.

[5] W.K. Son, H.K. Sang, S.G. Park, Synthesis and exchange properties of sulfonated poly(phenylene sulfide) with alkali metal ions in organic solvents, Bull. Korean Chem. Soc. 22 (2001) 53–58.

[6] M.L. Cecopieri-Gómez, J. Palacios-Alquisira, J.M. Domínguez, On the limits of gas separation in CO2/CH4, N2/CH4and CO2/N2binary mixtures using polyimide membranes, J. Memb. Sci. 293 (2007) 53–65. https://doi.org/10.1016/j.memsci.2007.01.034.

[7] D. Chen, R. Wang, W.W. Tjiu, T. Liu, High performance polyimide composite films prepared by homogeneity reinforcement of electrospun nanofibers, Compos. Sci. Technol. 71 (2011) 1556–1562. https://doi.org/10.1016/j.compscitech.2011.06.013.

[8] W. Tanthapanichakoon, M. Hata, K. hei Nitta, M. Furuuchi, Y. Otani, Mechanical degradation of filter polymer materials: Polyphenylene sulfide, Polym. Degrad. Stab. 91 (2006) 2614–2621. https://doi.org/10.1016/j.polymdegradstab.2006.05.005.

[9] W. Qiu, C.C. Chen, M.R. Kincer, W.J. Koros, Thermal analysis and its application in evaluation of fluorinated polyimide membranes for gas separation, Polymer (Guildf). 52 (2011) 4073–4082. https://doi.org/10.1016/j.polymer.2011.07.002.

[10] G.R. Sharma, C. Lind, M.R. Coleman, Preparation and properties of polyimide nanocomposites with negative thermal expansion nanoparticle filler, Mater. Chem. Phys. 137 (2012) 448–457. https://doi.org/10.1016/j.matchemphys.2012.09.009.

[11] J. Happel, Viscous flow relative to arrays of cylinders, AIChE J. 5 (1959) 174–177. https://doi.org/10.1002/aic.690050211.

[12] H. Yang, S. He, H. Ouyang, M.J. Anderson, L. Shen, C.J. Hogan, The pressure drop across combined polydisperse spherical particle – Cylindrical fiber networks, Chem. Eng. Sci. 192 (2018) 634–641. https://doi.org/10.1016/j.ces.2018.08.006.

[13] T. Ando, K. Akamatsu, S. ichi Nakao, M. Fujita, Simulation of fouling and backwash dynamics in dead-end microfiltration: Effect of pore size, J. Memb. Sci. 392–393

(2012) 48–57. https://doi.org/10.1016/j.memsci.2011.11.051.

[14] T. Ishigami, H. Fuse, S. Asao, D. Saeki, Y. Ohmukai, E. Kamio, H. Matsuyama, Permeation of Dispersed Particles through a Pore and Transmembrane Pressure Behavior in Dead-End Constant-Flux Microfiltration by Two-Dimensional Direct Numerical Simulation, Ind. Eng. Chem. Res. 52 (2013) 4650–4659. https://doi.org/10.1021/ie302448x.

[15] Y. Kagawa, T. Ishigami, K. Hayashi, H. Fuse, Y. Mino, H. Matsuyama, Permeation of concentrated oil-in-water emulsions through a membrane pore: Numerical simulation using a coupled level set and the volume-of-fluid method, Soft Matter. 10 (2014) 7985–7992. https://doi.org/10.1039/c4sm00705k.

[16] Y. Mino, Y. Kagawa, H. Matsuyama, T. Ishigami, Permeation of oil-in-water emulsions through coalescing filter: Two-dimensional simulation based on phase-field model, AIChE J. 62 (2016) 2525–2532. https://doi.org/10.1002/aic.15206.

[17] Y. Yoshida, Y. Inoue, A. Shimosaka, Y. Shirakawa, J. Hidaka, Effect of aperture structure of Dutch weave mesh on flow resistivity, J. Chem. Eng. Japan. 48 (2015) 730–741. https://doi.org/10.1252/jcej.14we168.

[18] T. Ishigami, Y. Mino, Simulation of permeation of colloidal particle dispersion through membrane pores in microfiltration, J. Soc. Powder Technol. Japan. 54 (2017) 362–369. https://doi.org/10.4164/sptj.54.362.

[19] P. Iassonov, T. Gebrenegus, M. Tuller, Segmentation of X-ray computed tomography images of porous materials: A crucial step for characterization and quantitative analysis of pore structures, Water Resour. Res. 45 (2009) 1–12. https://doi.org/10.1029/2009WR008087.

[20] B. Ferrol, D.H. Rothman, Lattice-Boltzmann simulations of flow through Fontainebleau sandstone, Transp. Porous Media. 20 (1995) 3–20. https://doi.org/10.1007/BF00616923.

[21] C. Pan, M. Hilpert, C.T. Miller, Lattice-Boltzmann simulation of two-phase flow in porous media, Water Resour. Res. 40 (2004) 1–14. https://doi.org/10.1029/2003WR002120.

[22] M.L. Porter, M.G. Schaap, D. Wildenschild, Lattice-Boltzmann simulations of the capillary pressure-saturation-interfacial area relationship for porous media, Adv. Water Resour. 32 (2009) 1632–1640. https://doi.org/10.1016/j.advwatres.2009.08.009.

[23] E.S. Boek, M. Venturoli, Lattice-Boltzmann studies of fluid flow in porous media with realistic rock geometries, Comput. Math. with Appl. 59 (2010) 2305–2314. https://doi.org/10.1016/j.camwa.2009.08.063.

[24] A.Q. Raeini, M.J. Blunt, B. Bijeljic, Direct simulations of two-phase flow on micro-CT images of porous media and upscaling of pore-scale forces, Adv. Water Resour. 74 (2014) 116–126. https://doi.org/10.1016/j.advwatres.2014.08.012.

[25] A.Q. Raeini, B. Bijeljic, M.J. Blunt, Modelling capillary trapping using finite-volume simulation of two-phase flow directly on micro-CT images, Adv. Water Resour. 83 (2015) 02–110. https://doi.org/10.1016/j.advwatres.2015.05.008.

[26] T. Kajishima, S. Takiguchi, H. Hamasaki, Y. Miyake, Turbulence Structure of Particle-Laden Flow in a Vertical Plane Channel Due to Vortex Shedding, JSME Int. J. Ser. B. 44 (2001) 526–535. https://doi.org/10.1299/jsmeb.44.526.

[27] H. Darcy, Les Fontaines Publiques de la Ville de Dijon, in: Paris: Dalmont, 1856.

[28] J. Kozeny, Ueber kapillare Leitung des Wassers im Boden, Sitzungsber Akad. Wiss., Wien. 136 (1927) 271–306.

[29] P.C. Carman, Fluid flow through granular beds, Transactions. 15 (1937) 150–166. https://doi.org/10.1016/S0263-8762(97)80003-2.

[30] T. Kajishima, K. Taira, Computational Fluid Dynamics Incompressible Turbulent Flows, 2017. https://doi.org/10.1007/978-3-319-45304-0.

[31] D.J. Tritton, Experiments on the flow past a circular cylinder at low Reynolds numbers, J. Fluid Mech. 6 (1959) 547–567. https://doi.org/10.1017/S0022112059000829.

[32] J. Schindelin, I. Arganda-Carreras, E. Frise, V. Kaynig, M. Longair, T. Pietzsch, S. Preibisch, C. Rueden, S. Saalfeld, B. Schmid, J.Y. Tinevez, D.J. White, V.

Hartenstein, K. Eliceiri, P. Tomancak, A. Cardona, Fiji: An open-source platform for biological-image analysis, Nat. Methods. 9 (2012) 676–682. https://doi.org/10.1038/nmeth.2019.

[33] Y. Mori, C.Y. Wu, M. Sakai, Validation study on a scaling law model of the DEM in industrial gas-solid flows, Powder Technol. 343 (2019) 101–112. https://doi.org/10.1016/j.powtec.2018.11.015.

[34] H. Yao, Y. Mori, K. Takabatake, X. Sun, M. Sakai, Numerical investigation on the influence of air flow in a die filling process, J. Taiwan Inst. Chem. Eng. 90 (2018) 9–17. https://doi.org/10.1016/j.jtice.2017.11.031.

[35] Bag filter material [Toyobo P84], (n.d.). https://www.toyobo.co.jp/seihin/fb/procon/p84.html (accessed January 8, 2019).

[36] Bag filter material [Toyobo Procon], (n.d.). https://www.toyobo.co.jp/seihin/fb/procon/procon.html (accessed January 8, 2019).

[37] Q. Wang, Y. Bai, J. Xie, Q. Jiang, Y. Qiu, Synthesis and filtration properties of polyimide nanofiber membrane/carbon woven fabric sandwiched hot gas filters for removal of PM 2.5 particles, Powder Technol. 292 (2016) 54–63. https://doi.org/10.1016/j.powtec.2016.01.008.

[38] Y. Bian, L. Zhang, C. Chen, Experimental and modeling study of pressure drop across electrospun nanofiber air filters, Build. Environ. 142 (2018) 244–251. https://doi.org/10.1016/j.buildenv.2018.06.021.

[39] T. Xia, Y. Bian, L. Zhang, C. Chen, Relationship between pressure drop and face velocity for electrospun nanofiber filters, Energy Build. 158 (2018) 987–999. https://doi.org/10.1016/j.enbuild.2017.10.073.

[40] S. Choi, K.C. Oh, C.B. Lee, The effects of filter porosity and flow conditions on soot deposition/oxidation and pressure drop in particulate filters, Energy. 77 (2014) 327–337. https://doi.org/10.1016/j.energy.2014.08.049.

[41] A. Inayat, H. Freund, A. Schwab, T. Zeiser, W. Schwieger, Predicting the specific surface area and pressure drop of reticulated ceramic foams used as catalyst support,

Adv. Eng. Mater. 13 (2011) 990–995. https://doi.org/10.1002/adem.201100038.

[42] C.N. Davies, The Separation of Airborne Dust and Particles, Proc. Inst. Mech. Eng. Part B Manag. Eng. Manuf. 1 (1953) 185–213. https://doi.org/10.1177/095440545300100113.

[43] J.E. Drummond, M.I. Tahir, Laminar viscous flow through regular arrays of parallel solid cylinders, Int. J. Multiph. Flow. 10 (1984) 515–540. https://doi.org/10.1016/0301-9322(84)90079-X.

[44] J. Feng, S. Weinbaum, Lubrication theory in highly compressible porous media: the mechanics of skiing, from red cells to humans, J. Fluid Mech. 422 (2000) S0022112000001725. https://doi.org/10.1017/S0022112000001725.

[45] R. Crawford, G.F. Jones, L. You, Q. Wu, Compression-dependent permeability measurement for random soft porous media and its implications to lift generation, Chem. Eng. Sci. 66 (2011) 294–302. https://doi.org/10.1016/j.ces.2010.10.037.

[46] Z. Zhu, Q. Wang, Q. Wu, On the examination of the Darcy permeability of soft fibrous porous media; new correlations, Chem. Eng. Sci. 173 (2017) 525–536. https://doi.org/10.1016/j.ces.2017.08.021.

[47] B. Kruczek, Carman--Kozeny Equation, in: E. Drioli, L. Giorno (Eds.), Encycl. Membr., Springer Berlin Heidelberg, Berlin, Heidelberg, 2016: pp. 306–308. https://doi.org/10.1007/978-3-662-44324-8_1995.

[48] A. Nakayama, F. Kuwahara, Y. Sano, Concept of equivalent diameter for heat and fluid flow in porous media, AIChE J. 53 (2007) 732–736. https://doi.org/10.1002/aic.11092.

[49] D. Vidal, C. Ridgway, G. Pianet, J. Schoelkopf, R. Roy, F. Bertrand, Effect of particle size distribution and packing compression on fluid permeability as predicted by lattice-Boltzmann simulations, Comput. Chem. Eng. 33 (2009) 256–266. https://doi.org/10.1016/j.compchemeng.2008.09.003.

[50] H.L. Liu, W.R. Hwang, Permeability prediction of fibrous porous media with complex 3D architectures, Compos. Part A Appl. Sci. Manuf. 43 (2012) 2030–2038.

https://doi.org/10.1016/j.compositesa.2012.07.024.

[51] T. Ozgumus, M. Mobedi, U. Ozkol, Determination of kozeny constant based on porosity and pore to throat size ratio in porous medium with rectangular rods, Eng. Appl. Comput. Fluid Mech. 8 (2014) 308–318. https://doi.org/10.1080/19942060.2014.11015516.

Chapter 4

Direct Numerical Simulation of Permeation of Particles through a Realistic Fibrous Filter Obtained from X-ray Computed Tomography Images Utilizing Signed Distance Function

4.1 Introduction

Gas–solid two-phase flows are often encountered in various industrial processes. A bag filter is a typical gas–solid flow system that, due to their economic appeal and collection efficiency, is frequently used in chemical, environmental, and energy industries to control the emissions of dust and harmful materials [1]. Polyphenylene sulfide (PPS) is one of the most widely used materials for bag filters because it is extremely resistant to chemicals and highly durable under high-temperature conditions (160 – 240 °C)[2–4]. Filtration processes have recently received more attention to meet air pollutant emission standards, which have become stricter because of the urgent need to improve the air quality and reduce the emission of contaminants that may be harmful to human health.

The pressure drop across the filter media is a crucial aspect of the filtration system of bag filters, which is a key factor in estimating the filtration life and required operating power. During filtration, dust is deposited on the surface of the filter media forming a filter cake, which is responsible for increasing the pressure drop of the system. Many researchers have studied the bag filter mainly through an experimental approach, especially the effect of operating conditions [5–7], filtration velocity [8,9], and filter treatment [10,11] on the cake formation. However, the interaction between particles and filters is still unclear, as well as how the cake layer grows on the filter media surfaces causing increased pressure drops. The flow in a bag filter system is too complicated to fully characterize experimentally because of the complex geometry of the fibrous material.

Numerical simulations are effective and useful for studying the flow field and particle motion within porous media such as bag filters. Several researchers have also investigated the filtration system of porous media using numerical simulation, in both 2D and 3D cases. For 2D simulation cases, most researchers have used simple shapes, such as cylindrical fibers. Karadimos and Ocone [12], Wang et al. [13], Mino et al. [14,15], and Muller [16] used a simple 2D cylindrical fiber model to simulate the filtration process in a fibrous filter.

Karadimos and Ocone simulated the loading process of aerosol particles on a 2D cylindrical fiber and investigated the influence of fluid flow recalculation around a single fiber during the loading process. Wang et al. investigated the particle deposition on a cylindrical fiber filter under laminar flow using the lattice Boltzmann method. Mino et al. simulated the permeation of oil-in-water emulsions through a coalescing filter using the lattice Boltzmann method. They investigated the effect of fiber diameter [14] and filter structure [15]. Fuse et al. [17] also investigated the permeation of dispersed particles through a pore, and the transmembrane pressure behavior in dead-end microfiltration using 2D direct numerical simulation. For 3D simulation cases, researchers have usually used simple geometries such as filtration through cylindrical pores and filtration through cylindrical fibers. For example, Ando et al. [18] simulated the permeation of particles through cylindrical pores in dead-end microfiltration. They investigated the effect of pore size on particle fouling. Tao et al.[19] simulated the filtration of microparticles within arranged cylindrical fibers using a coupled simulation based on computational fluid dynamics and the discrete element method (CFD-DEM). They examined the pressure drop and filtration efficiency of the system. Fotovati et al.[20] and Pradhan et al.[21] investigated the effect of 3D fiber orientation distribution on filtration media performance using a modified discrete phase model and a stochastic ordinary differential equation model, respectively. They created a filter with a regular arrangement of uniform cylindrical straight fibers. Fotovati et al.[20] focused only on in-plane fiber orientation, whereas Pradhan et al.[21] varied the fiber orientation only in the perpendicular plane, and the parallel plane orientation was kept constant. Hosseini and Tafreshi [22] generated 3D fibrous material to simulate filtration efficiency and the fibrous filter pressure drop. Yue et al. [23] established a three-dimensional random structure of a fibrous filter and investigated the filtration process using the CFD-DEM method. They assumed that the fiber arrangement was three-dimensionally random, and all fibers had an in-plane fiber orientation at a random angle and the same diameter. Although 3D geometries of fibrous media have been successfully created, several assumptions are still taken while creating a fibrous filter. Recently, our group has successfully developed a 3D fluid dynamics simulation method that utilized X-ray CT images of an actual fibrous filter.he robustness of the method was proved by simulating single-phase flow permeation through a fibrous filter, and the simulated pressure drop was in good agreement with experimental results and previous empirical equations [24]. The simulation of two-phase flow and droplet coalescence of an oil-in-water emulsion permeating through a fibrous filter was also conducted using our method [25].

In numerical simulations, the wall boundary is usually modeled by surface equations [26] or meshes [27]. The surface equations are useful in creating simple regimes, *for example*, spheres, cylinders, rectangular, and cones, but it is not easy to express complex geometry shaped walls. The meshes are more adaptable for arbitrary shapes, but it is difficult to detect collisions between particles and walls. A simple boundary model where a scalar field expresses the wall boundary with a signed distance function (SDF) was proposed to solve these problems [28]. An arbitrarily shaped wall boundary can be easily created without any complicated algorithm, and the collision can be detected without any complicated procedures. The application of SDF has been proved through validation tests in die-filling, hopper, mill, and screw conveyors [29–32]. Although the robustness of the SDF model was demonstrated in some practical granular flow systems, the application of the SDF model to filtration systems has not yet been examined. It is challenging to calculate the SDF of the actual filter media due to its complex geometry, as shown in the X-ray CT images. In previous studies, a number of researchers have reconstructed the SDF from arbitrary shapes using the fast marching method [28,33] and an interpolation method that finds the closest point on the interface [34,35] in the numerical simulation of free-surface flow. In specific, a coupled level set and volume of fluid method has been employed.

Although these methods can describe the SDF, Cummins et al. pointed out that the error in the curvature defined by the reconstructed SDF did not decrease at high spatial resolutions [36]. Hayashi et al. explained that the interface profile reconstructed from the Cahn-Hilliard equation based on the phase-field model [37] improved the accuracy of the curvature and normal vector, which is used for the calculation of the contact force between the surface and the particle in the discrete element method (DEM) owing to the linearity of the interface profile reconstructed in the phase-field model [38].

In the present study, we propose a new method to create an SDF from the microstructure of an actual bag filter obtained from X-ray CT images by utilizing a phase-field model and a level set method. A direct numerical simulation model was constructed to investigate the permeation of particles through a fibrous filter by coupling the immersed boundary method and SDF. A commercial polyphenylene sulfide (PPS) nonwoven fabric filter was utilized. Because this model realistically expresses the microstructure of the fibrous filter, the fluid flow around the fibers, and the contact between particles and the fiber surface were accurately described during simulations. To demonstrate our simulation method, direct numerical simulations of the permeation of particles through the realistic microstructure

created from X-ray CT images of the PPS filter were performed. This study focused on the physical interaction between the gas–solid flow and the fibers, where the fibers were randomly arranged and oriented perpendicularly and parallelly to the main flow direction. From the simulation results, the suitability and applicability of the present numerical framework to simulate gas–solid flow inside an actual fibrous filter were confirmed.

4.2 Numerical methods

4.2.1 Fluid and particle motions

In this model, the incompressible Newtonian fluid is governed by the continuity and Navier–Stokes equations, which are expressed as follows:

$$\nabla \cdot \mathbf{u} = 0 \tag{4-1}$$

$$\frac{\partial \mathbf{u}}{\partial t} + \mathbf{u} \cdot \nabla \mathbf{u} = -\frac{1}{\rho}\nabla p + \frac{1}{\rho}\nabla \cdot \eta \nabla \mathbf{u} + \mathbf{g} + \mathbf{f} \tag{4-2}$$

where **u** is the velocity, t is the time, p is the pressure, and **g** is the gravitational acceleration. The density ρ and viscosity η of the fluid were assumed to be constant. A Cartesian grid system was used for the arrangement of the Eulerian variables.

The motion of each particle is tracked based on the Lagrangian approach using Newton's law of motion. The translational and rotational motions of a solid particle are given by

$$m_{\mathrm{p}} \frac{d\mathbf{v}_{\mathrm{p}}}{dt} = \mathbf{F}_{\mathrm{h}} + \sum \mathbf{F}_{\mathrm{c}} + m_{\mathrm{p}}\mathbf{g} \tag{4-3}$$

$$I_{\mathrm{p}} \frac{d\boldsymbol{\omega}_{\mathrm{p}}}{dt} = \mathbf{T}_{\mathrm{h}} + \sum \mathbf{T}_{\mathrm{c}} \tag{4-4}$$

where m_{p} denotes the mass of the particle, $\mathbf{v}_{\mathrm{p}}$ is the translational velocity of the particle, I_{p} is the moment of inertia, $\boldsymbol{\omega}_{\mathrm{p}}$ is the angular velocity, and $\mathbf{F}_{\mathrm{h}}$, $\mathbf{F}_{\mathrm{c}}$, $\mathbf{T}_{\mathrm{h}}$, and $\mathbf{T}_{\mathrm{c}}$ are the hydrodynamic and contact forces, and the hydrodynamic and contact torques acting on a particle, respectively. Note that the van der Waals force acting on the particles is neglected because the calculation of the contact force between the particle and the fiber surface using SDF is the focus of this study.

The hydrodynamic interaction between the solid (particles and filter) and fluid is expressed as the momentum exchange at the solid–fluid interface. The immersed boundary method (IBM) [39,40] was employed to solve these momentum exchanges. The volume-averaged velocity **u** is defined as follows:

$$\mathbf{u} = \alpha \mathbf{u}_\mathrm{p} + (1 - \alpha)\mathbf{u}_\mathrm{f} \tag{4-5}$$

where α represents the local volume fraction of the solids in the computational cell. $\mathbf{u_p}$ and $\mathbf{u}_\mathrm{f}$ are the velocities of the solid phase and fluid phase, respectively.

The velocity inside the particle can be decomposed using the translation, and the rotational components of the particle motion as given by

$$\mathbf{u}_\mathrm{p} = \mathbf{v}_\mathrm{p} + \boldsymbol{\omega}_\mathrm{p} \times \mathbf{r} \tag{4-6}$$

where $\mathbf{r}$ is the relative position vector between the center of the particle and the grid. The force $\mathbf{f}$ is introduced to modify the calculated velocity to the desired velocity according to each phase, such that $\mathbf{f}$ is defined as follows:

$$\mathbf{f} = \frac{\alpha\left(\mathbf{u}_\mathrm{p} - \mathbf{u}^*\right)}{\Delta t} \tag{4-7}$$

where $\mathbf{u}^*$ is the fluid velocity temporarily obtained in each iteration, and Δt is the time step. If the cell is located inside the solid region ($\alpha = 1$), the velocity is equal to the velocity of the solid. Conversely, if the cell is located within the fluid region ($\alpha = 0$), the velocity is equal to the local fluid velocity. The solid volume fraction of the particle was estimated using the smoothed profile method [41].

The hydrodynamic force and torque acting on the particle are obtained by integrating the interaction force over the particle volume:

$$\mathbf{F}_\mathrm{h} = -\rho \int_{V_\mathrm{p}} \mathbf{f} \mathrm{d}V \tag{4-8}$$

$$\mathbf{T}_\mathrm{h} = -\rho \int_{V_\mathrm{p}} \mathbf{f} \times \mathbf{R}\, \mathrm{d}V \tag{4-9}$$

where V_p is the volume of the particle and $\mathbf{R}$ is the relative position vector from the center of the particle.

This study employed the DEM [42] to calculate the contact force acting on each particle. The particles were modeled as solid spheres, and it was assumed that the particles could overlap each other when the contact occurred. The contact force $\mathbf{F}_\mathrm{c}$ between the particles is divided into the normal and tangential components as follows:

$$\mathbf{F}_\mathrm{c} = \mathbf{F}_{\mathrm{c_n}} + \mathbf{F}_{\mathrm{c_t}} \tag{4-10}$$

where the subscripts n and t indicate the normal and tangential components, respectively. The contact force acting on a solid particle is given by elastic and damping forces. The elastic

force is expressed by analogy with Hooke's law for springs. The normal component $\mathbf{F}_{c_n}$ is expressed as

$$\mathbf{F}_{c_n} = -k_p \boldsymbol{\delta}_n - \eta_p \mathbf{v}_n \tag{4-11}$$

and the tangential component by:

$$\mathbf{F}_{c_t} = \begin{cases} -k_p \boldsymbol{\delta}_n - \eta_p \mathbf{v}_n & \left(|\mathbf{F}_{c_t}| \le \mu^{pp} |\mathbf{F}_{c_n}|\right) \\ -\mu_p |\mathbf{F}_{c_n}| \dfrac{\mathbf{v}_t}{|\mathbf{v}_t|} & \left(|\mathbf{F}_{c_t}| > \mu^{pp} |\mathbf{F}_{c_n}|\right) \end{cases} \tag{4-12}$$

where k_p is the spring constant, $\boldsymbol{\delta}$ is the overlap distance between particles, η_p is the damping coefficient, $\mathbf{v}$ is the translational velocity of the particle, and μ_p is the friction coefficient. The damping coefficient is acquired based on the energy dissipation, given by

$$\eta_p = -2(\ln e)\sqrt{\frac{m_p k_p}{\pi^2 + (\ln e)^2}} \tag{4-13}$$

where e represents the restitution coefficient.

4.2.2 Wall boundary model of fiber surface

The boundary condition of the fiber surface for fluid computation was also described by IBM. An arbitrary shape wall boundary can be easily created by IBM. The velocity of the fibers was assumed to be zero in this study. When we set $\mathbf{u}_p = 0$ in Eq. (4-7), the velocity is forced according to the solid volume fraction α in the cell of the fiber, and the no-slip condition on the fiber surface is implicitly achieved. Although no specifications of the boundary conditions around the solid are required, the no-slip boundary conditions on the solid surface can be realized in the structured grid system. This method is suitable for the description of solids with complex geometries [42,43], such as fibrous filters.

The contact interaction between the particles and the filter was calculated as the contact between the particles and the wall boundary, where the arbitrary-shaped wall boundary model was expressed by the scalar field with the SDF. The advantage of the SDF model is that the collision detection procedure is unaffected by the complexity of the boundaries. The SDF, denoted by ϕ, is defined as follows:

$$\phi(\mathbf{x}) = d(\mathbf{x}) s(\mathbf{x}) \tag{4-14}$$

where $d(\mathbf{x})$ is the minimal distance from the position vector $\mathbf{x}$ to the surface of the solid, and $s(\mathbf{x})$ is the sign, which is negative for $\mathbf{x}$ inside the solid and vice versa. The normal component

of the contact force based on the improved SDF model by Shigeto and Sakai [29] is expressed as follows:

$$\mathbf{F}_{\mathrm{cn}}^{\mathrm{SDF}} = -k_{\mathrm{p}}\boldsymbol{\delta}_{\mathrm{n}}^{\mathrm{SDF}}|\nabla\phi| - \eta_{\mathrm{p}}\mathbf{v}_{\mathrm{n}} \tag{4-15}$$

and the tangential component by:

$$\mathbf{F}_{\mathrm{c_t}} = \begin{cases} -k_{\mathrm{p}}\boldsymbol{\delta}_{\mathrm{t}}^{\mathrm{SDF}} - \eta_{\mathrm{p}}\mathbf{v}_{\mathrm{t}} & \left(|\mathbf{F}_{\mathrm{c_t}}| \le \mu^{\mathrm{pw}}|\mathbf{F}_{\mathrm{c_n}}|\right) \\ -\mu_{\mathrm{p}}|\mathbf{F}_{\mathrm{c_n}}|\dfrac{\mathbf{v}_{\mathrm{t}}}{|\mathbf{v}_{\mathrm{t}}|} & \left(|\mathbf{F}_{\mathrm{c_t}}| > \mu^{\mathrm{pw}}|\mathbf{F}_{\mathrm{c_n}}|\right) \end{cases} \tag{4-16}$$

The superscript SDF indicates the case when an overlap occurs between particle and solid (filter structure) surfaces obtained from the SDF. The purpose of the simulation in this study is to qualitatively represent the contact behavior of particles on the fiber surface by using SDF. Therefore, the parameters of stiffness and friction coefficient of the fiber used in the simulation are based on the previous studies [29–32], which had been sufficiently validated by comparing simulations and experiments in several studies. The value of the parameters of the fiber are also adopted the same with the particle because the effect of hydrodynamics force on particle motion is more dominant than the effect of stiffness[45]. The application of the SDF in the DEM simulation has been validated in several studies, such as in a die-filling [46], in an industrial blender [47], and in a ribbon mixer [48].

The wall boundary model combined with the SDF and IBM has been validated sufficiently. This method has been employed in several industrial applications such as fluidized beds [31], spouted beds [49], and gas–solid flows between thin walls [50]. The simulation results were shown to be in good agreement with the experimental results, and thus, the adequacy of the wall boundary model combined with the SDF and IBM has been proven.

4.2.3 Creation of filter domain

A commercial PPS fibrous filter (Procon, Toyobo Co., Ltd) was employed in this simulation. The microstructure of the filter was modelled in the simulation based on an image processing method using X-ray CT, which was reported in our previous work [24]. The filter sample was scanned using a high-resolution X-ray CT system at an energy level of 30 kV and 0.075 mA (TDM1000H-Sμ, Yamato Science Co., Ltd). The X-ray CT images were then processed as follows. First, Adobe Photoshop was used to reduce the noise, invert, and set the threshold of the images to obtain a binary image of the PPS filter. After that, the images were smoothed and converted to text file data using the open-source ImageJ/Fiji

software, which outputs a combination of numbers in the range from 0 to 255 according to the color brightness of each pixel. Finally, the solid volume fraction α used for the IBM was determined by linear interpolation of the text file data. Illustration of image processing procedure is shown in **Figure 4.1** and the detailed explanation can be found in our previous work [24].

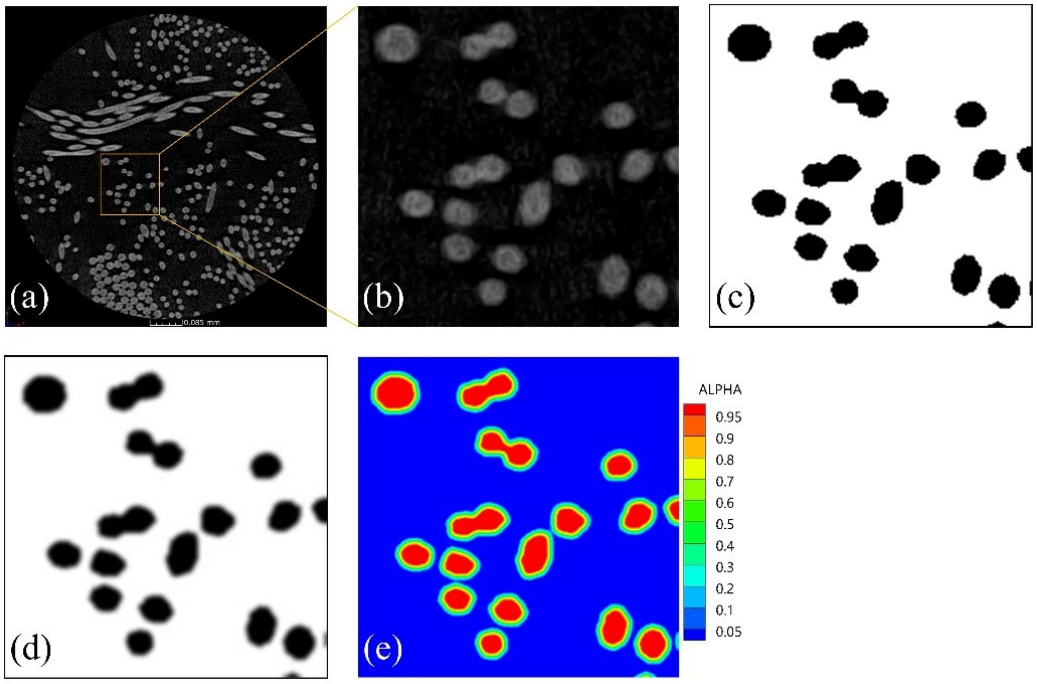

Figure 4.1 Image processing procedure for X-ray CT images of PPS filter: (a) a slice of X-ray CT images, (b) images after noise reduction, (c) images after inverting and thresholding, (d) images after smoothing process by Fiji, and (e) contour of solid volume fraction

The filter domain used for the simulation was created using voxel data with dimensions of 58.5 × 58.5 × 58.5 μm corresponding to the *x*, *y*, and *z* directions, respectively. It should be noted that the size of the filter domain should be kept small to reduce the simulation time. Four filter domains were prepared. The visualization of each domain is presented in **Figure 4.2**. It can be seen that the arrangement and fiber orientation of each filter domain are clearly different. The porosity of each filter domain was calculated using the solid volume fraction α:

$$\varepsilon = \frac{\sum(1-\alpha)\Delta\Theta}{\sum\Delta\Theta} \tag{4-17}$$

where ε is the porosity, and $\Delta\Theta$ is the cell volume, and the summation is taken for all the grid cells in the filter domain.

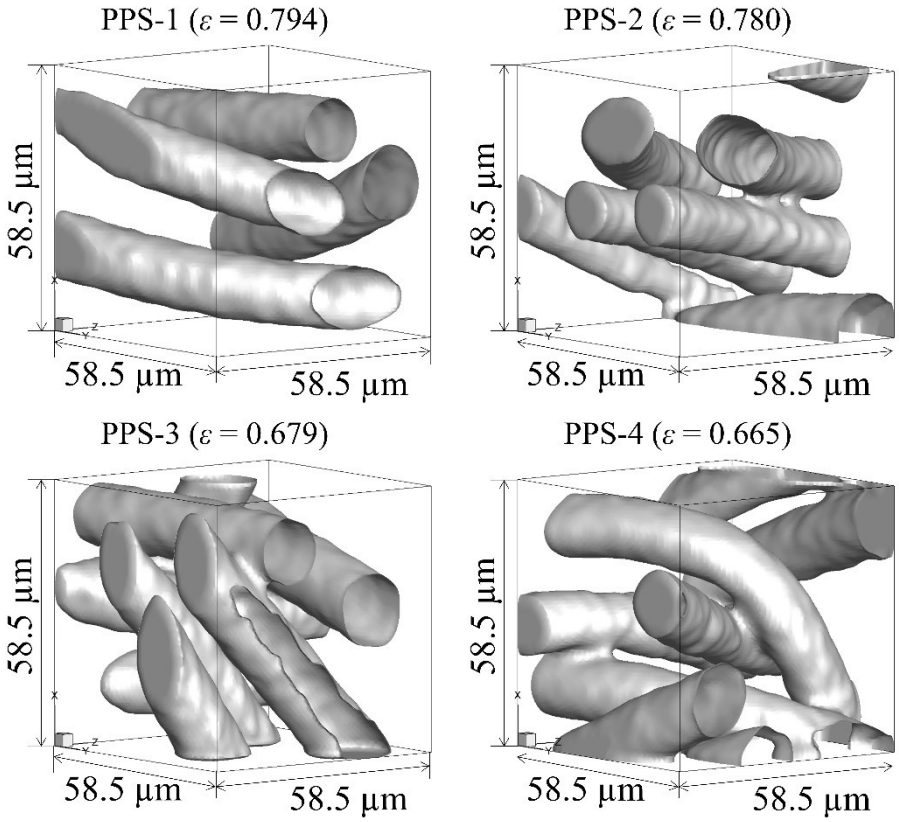

Figure 4.2 Filter domains created from X-ray CT images. The length of all sides of the domains is equally 58.5 μm.

4.2.4 Calculation of signed distance function from complex geometry obtained by X-ray CT images

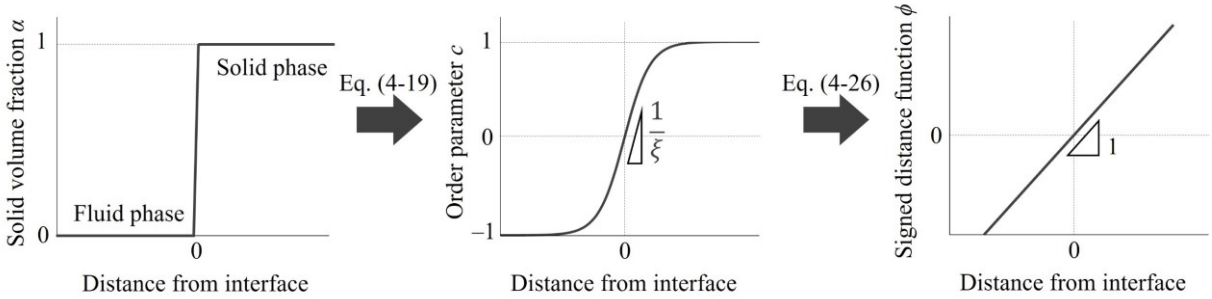

Figure 4.3 One-dimensional schematic illustration of the present scheme for calculating the signed distance function from solid volume fraction obtained from X-ray CT processing.

In this study, we propose a method to calculate the SDF value around the complex geometry of the filter microstructure obtained from X-ray CT images using the phase-field model and the level set method [51]. The scheme of this method is shown in **Figure 4.3**.

First, the solid volume fraction of the filter microstructure obtained from the X-ray CT images was transformed into the order parameter c for the phase-field model, where $c = 1$ for the solid, $c = -1$ for the fluid, and $-1 < c < 1$ for the interface. The aim of this procedure is to convert the solid–fluid interface with a sharp interface profile to a smoothed interface profile defined by the phase-field model. When an interface was located at the yz-plane (normal to the x-axis), the interface profile of the order parameter was analytically expressed as

$$c(\mathbf{x}) = \tanh\left(\frac{\mathbf{x}}{\xi}\right) \tag{4-18}$$

where ξ is the width of the interfacial region and is set to $1.5\Delta x$ (Δx is the mesh size). To obtain the order parameter from the solid volume fraction, the following Cahn-Hilliard equation was employed.

$$\frac{\partial c}{\partial \tau} = M\nabla^2\mu \tag{4-19}$$

where τ is the pseudo time, and M is the mobility, which is a positive constant that affects the reconstruction of the diffusive interface. μ is the chemical potential and is expressed as follows:

$$\mu = f'(c) - \kappa\nabla^2 c \tag{4-20}$$

where κ is the gradient energy coefficient. $f(c)$ is the bulk energy, which is written in the following double-well potential.

$$f(c) = -\frac{a}{4}(2c^2 - c^4) \tag{4-21}$$

where a is a positive constant, and the potential yields two minima at $c(\mathbf{x}) = -1$ and $c(\mathbf{x}) = 1$. In addition, at equilibrium, the following relationship holds for a, κ, and ξ.

$$\xi = \sqrt{\frac{2\kappa}{a}} \tag{4-22}$$

By iteratively calculating Eq. (4-19), the order parameter can be obtained from the solid volume fraction. Note that, if the number of iterations is increased, the interfacial shape will gradually change so that the interface area is minimized. Thus, it is necessary to set the number of iterations to an appropriate value. In this study, the number of iterations of Eq. (4-19) was set to 200. Here, considering that the profile of the solid volume fraction is $0 \leq \alpha \leq 1$ and the profile of the order parameter is $-1 \leq c \leq 1$, $c_0 = 2\alpha - 1$ was used as the

initial value for calculating Eq. (4-19). The central difference and Euler schemes were applied to calculate the right-hand side and unsteady term of Eq. (4-19), respectively. The pseudo time step and mobility were set to 8.2×10^{-7} s and 5×10^{-13} $m^3 \cdot s/kg$, respectively.

Next, we obtain the SDF from the order parameter. Because the interface profile of the order parameter is described as a hyperbolic function, as shown in Eq. (4-18), the order parameter is mathematically linear at the solid surface. Hence, the SDF at the solid surface can be calculated as follows:

$$\phi_0 = \xi c \tag{4-23}$$

Using the obtained ϕ_0 as the initial value of ϕ, the following reinitialization equation is solved:

$$\frac{\partial \phi}{\partial \tau} = \mathrm{sign}(\phi)(1 - |\nabla \phi|) \tag{4-24}$$

where sign(ϕ) is the smoothed sign function and is given by

$$\mathrm{sign}(\phi) = \frac{\phi}{\sqrt{\phi^2 + \Delta x^2}} \tag{4-25}$$

Eq. (24) can be rewritten in the following advection equation.

$$\frac{\partial \phi}{\partial \tau} + \mathbf{w} \cdot \nabla \phi = \mathrm{sign}(\phi) \tag{4-26}$$

where

$$\mathbf{w} = \mathrm{sign}(\phi) \frac{\nabla \phi}{|\nabla \phi|} \tag{4-27}$$

This procedure is called the reinitialization process in the level set method, in which the SDF is reconstructed according to the interface shape. Eq. (4-26) implies that ϕ is advected with the characteristic velocity **w** pointing outwards from the surface [52]. Therefore, by iteratively calculating Eq. (4-26) until the solution converges, the SDF on the solid surface propagates across the entire computational domain, resulting in a field of the SDF. The essentially non-oscillatory and Runge-Kutta schemes were applied to calculate the convection and unsteady terms of Eq. (4-26), respectively [52].

The shape of the filter might be slightly changed during the reinitialization process because of the non-conservation property of the volume. In the present reinitialization process, the filter volume has decreased by less than 4%. We should investigate the installation of a method for preserving volume in a future work. Therefore, the solid volume

fraction of the filter needs to be recalculated based on the SDF, as proposed by Sun and Sakai [43]. The cell can be categorized as a fluid zone ($\phi > 0$) and a solid zone ($\phi \leq 0$). The solid cells are identified by the SDF value, where ϕ is non-positive for at least one of the two adjacent cells. It should be noted that Eq. (4-26) results in the sign of ϕ being negative in the fluid zone and positive in the solid zone. Therefore, we inverted the sign of ϕ after calculating Eq. (4-26) in order to make it consistent with the settings proposed by Sun and Sakai et al [43].

4.2.5 Simulation details

The governing equations for the fluid flow were solved numerically using the explicit fractional step method. The central difference method was applied to discretize the convection and diffusion terms. The pressure gradient and continuity equations were solved by the projection method [53]. The differential equations were solved iteratively using the alternating direction implicit method [54]. The velocity and position vectors of the particle computation were updated using the symplectic Euler scheme. The time step Δt was limited by the Courant-Friedrichs-Lewy condition and the diffusion number condition of the fluid computation, and the stiffness in the contact by DEM:

$$\Delta t \leq \min\left(\frac{C\Delta x}{|\mathbf{u}|_{\max}}, \frac{D\rho\Delta x^2}{\eta}, 2\sqrt{\frac{m_p}{k}}\right) \tag{4-28}$$

where C is the Courant number, which is usually less than 0.3, and D is the diffusion number, which is less than 0.5. The simulations were performed with a stable time step that satisfied Eq. (4-28).

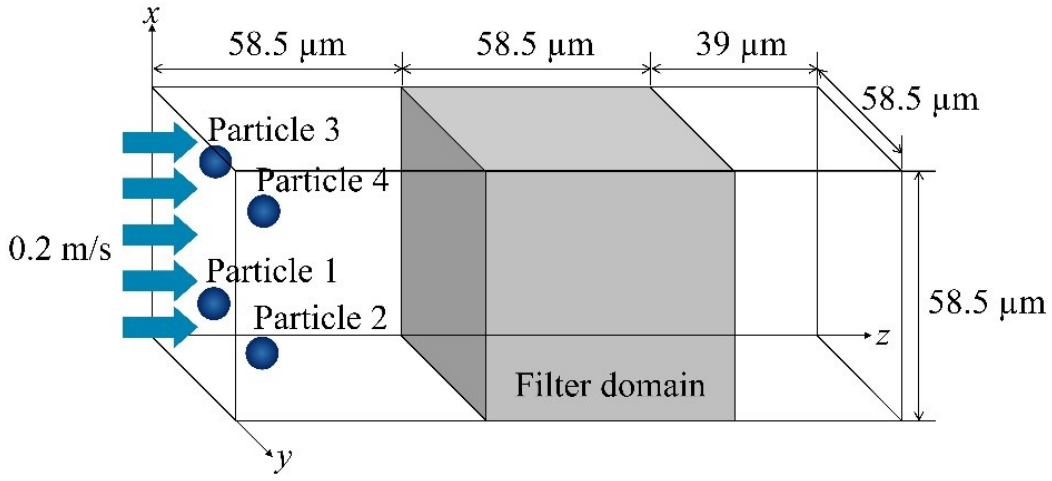

Figure 4.4 Computational domain for simulation of particle permeation through the filter domain.

Figure 4.4 shows the computational domain for the simulations. The size of the computational domain was 58.5 × 58.5 × 156 μm, and the domain was equally divided into 75 × 75 × 200 cells in the *x*, *y*, and *z* directions, respectively. The main flow direction was set according to the flow along the *z*-axis. A total of four particles (Particle 1, 2, 3, and 4) with a diameter of 5 μm, together with a fluid, were set to flow from the left to the right boundaries. 4 particles were chosen because it is easy to track the particle position and will be used to investigate the permeation behavior during permeation process. For the boundary conditions, the inlet velocity on the feed side was set as uniform at a constant value of 0.2 m/s. The Neumann condition was applied to the outlet boundary. The slip boundary conditions were applied to the other boundaries. The velocity and pressure at the steady state obtained from the simulation in the absence of particles were used as initial conditions. The center of each particle was initially placed at (*x* [μm], *y* [μm], *z* [μm]) = Particle 1 (14.6, 14.6, 10), Particle 2 (14.6, 43.9, 10), Particle 3 (43.9, 14.6, 10), and Particle 4 (43.9, 43.9, 10). The particles then flowed with the same translational velocity as the inlet uniform velocity of the fluid. Nitrogen gas at a temperature of 298.15 K was used as the fluid and glass bead was used as particles in this simulation. The physical properties of the fluid and particles are listed in **Table 4-1**.

Table 4-1 Physical properties of the fluid and particles used in the simulation

Fluid properties	
Viscosity	1.76×10^{-5} Pa·s
Density	1.25 kg/m^3
Particle properties	
Density	2500 kg/m^3
Diameter	5 μm
Spring constant	50 N/m
Coefficient of restitution	0.9
Coefficient of friction	0.3

4.3 Results and Discussion

First, we calculated the SDF value of each filter domain using our method. **Figure 4.5(a)** shows the iso-surface of PPS-2, where the SDF was equal to 0. The fiber surface shown by the SDF was smoother than the original fiber surface reconstructed from the X-ray CT

process, as shown in **Figure 4.2**, especially at the edges. This is due to the nature of the Cahn-Hilliard equation. Choi et al. applied the Cahn-Hilliard equation for smoothing piecewise linear shapes of various objects [55]. They explained that the gradient energy coefficient κ, which determines the interface thickness, affects the degree of surface smoothing. Increasing the value of κ increases the smoothness of the surface, whereas decreasing it may ultimately turn the surface into a profile mosaic. Although the shape was slightly changed, the representation of the original filter shape was still successfully created. **Figure 4.5(b)** shows a comparison of the SDF value and solid volume fraction α. The SDF value of the cell inside the filter is negative, as shown by the dashed line, and the SDF value is positive when the cell is located in the fluid region. The red line represents $\alpha = 0.5$. It is clearly seen that the location of $\alpha = 0.5$ corresponds to an SDF value of 0, which is located at the surface of the fibers. In addition, it can be seen that the smooth SDF contours were arranged at equal intervals according to the surface shape. This indicates that our method is useful for calculating the SDF value of the complicated geometry created from X-ray CT images.

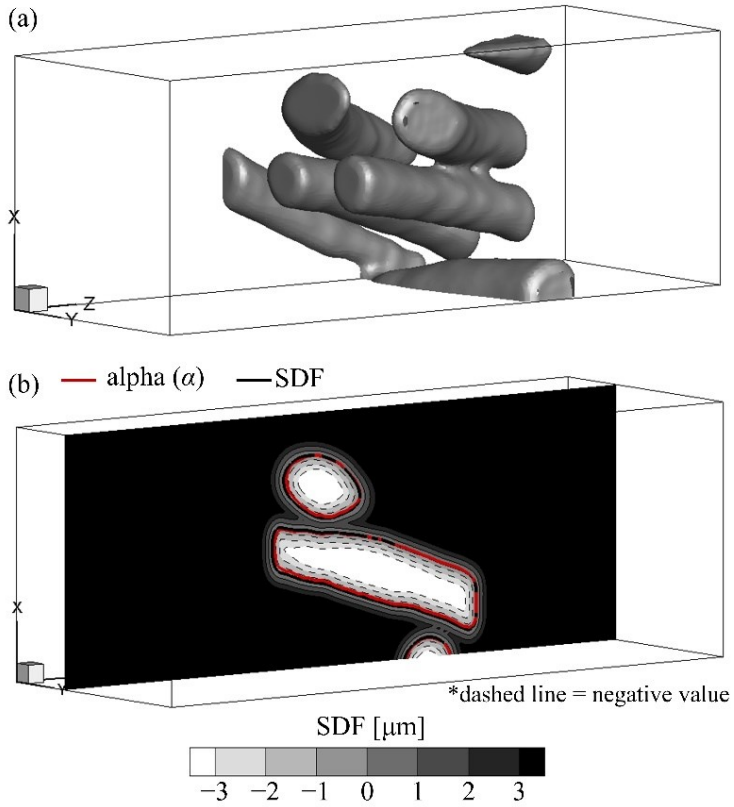

Figure 4.5 SDF in the computational domain including PPS-2. (a) Iso-surface of SDF value = 0 and (b) cross-sectional view of SDF and iso-surface of solid volume fraction value = 0.5 at y = 18.25 μm.

4.3.1 Application of the signed distance function

To check the application of the SDF model, we first compared the permeation behaviors of the four particles through PPS-3 with and without SDF. It should be noted that in a very recent study, Pan et al. simulated the particle and fluid behavior through a realistic porous membrane obtained by X-ray CT [56]. This study did not consider the contact forces between the particle and the solid surface. This is because the fluid drag force was considered to be dominant in the simulation. However, Mino et al. quantitatively showed that the contact force between the particle and solid surface has a significant effect on the permeation behavior in the pore, even in systems where fluid drag is dominant [57]. In order to clarify the effect of the contact force between the particle and the solid surface on the particle permeation behavior through the realistic porous structure obtained by X-ray CT, we compared the simulation with and without SDF.

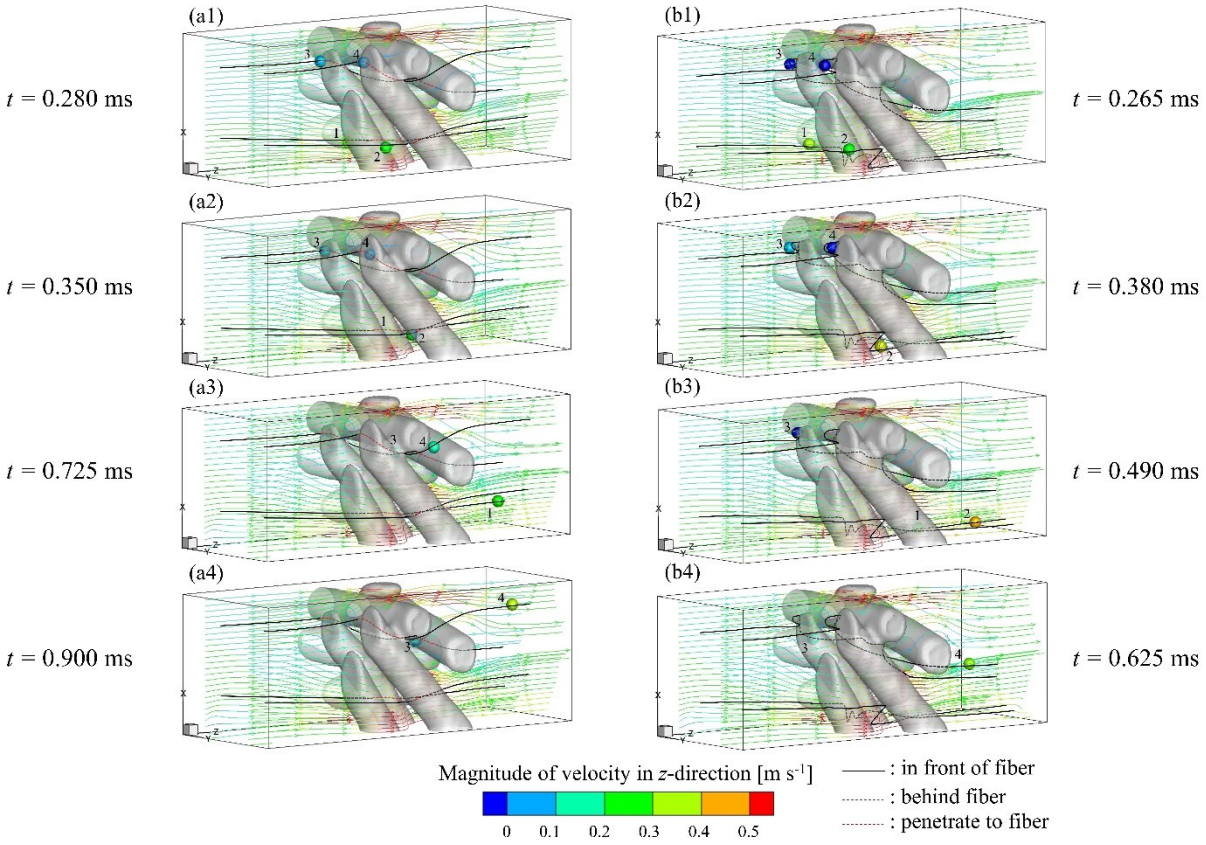

Figure 4.6 Time variation of permeation behavior of particles through PPS-3 (a) without SDF and (b) with SDF. Colors of particle and streamlines represent magnitude of velocity in *z*-direction.

Figure 4.6 (a) and **4.6 (b)** illustrate the snapshots of the permeation behaviors of particles through PPS-3 without SDF and with SDF, respectively. The line corresponds to the trajectory of each particle, where solid black line indicates the particle in front of the fiber, grey dash line indicates the particle behind the fiber, and the red dash line indicates the particle penetrating into fiber. The particles and streamline colors correspond to the magnitude of the translational velocity in the main flow direction. In both cases, all of the particles were transported to the filter domain accompanied by the fluid flow. Without SDF, Particles 3 and 4 passed through the fiber surfaces and penetrated into filter despite the presence of fibers (**Figure 4.6 (a1)** and **4.6 (a2)**). This occurred because in the case without SDF, the distance between the particle and the surface of the fiber could not be calculated. Thus, the contact force between the particles and the fiber surfaces could not be calculated. These particles moved through inside the fiber as shown in **Figure 4.6 (a2)** and **4.6 (a3)**. The particle velocities of Particles 3 and 4 significantly decreased because the velocity inside the fiber was set to 0. The particles then exited from the fibers and transported towards the right boundary of the computational domain accompanied by the fluid flow (**Figure 4.6 (a3)** and **4.6 (a4)**). Particles 1 and 2 were also immersed in the fiber (**Figure 4.6 (a2)**) because they were slightly in contact with them. Then, the particles moved towards the right boundary of the domain. From the above results, it was found that reasonable particle behaviors could not be expressed without appropriate boundary conditions on the fiber surface when the particles were in contact with the fibers. With SDF, Particles 3 and 4 contacted the front of the fibers and bounced back several times, as shown in **Figure 4.6 (b1)** and **4.6 (b2)**. Because the fibers were tightly arranged in the upper part of the filter domain, the particles could easily come in contact with the fibers. After the particles moved while being in contact with the surface of the fiber (**Figure 4.6 (b2)** and **4.6 (b3)**), they were transported through the gaps between the fibers and then towards the right boundary of the computational domain accompanied by the fluid flow (**Figure 4.6 (b3)** and **4.6 (b4)**). Particles 1 and 2 entered the filter domain through the bottom region (**Figure 4.6 (b1)**) and contacted the fibers (**Figure 4.6 (b2)**). The particles were then transported by the fluid flow (**Figure 4.6 (b2)** and **4.6 (b3)**). All of the particles were in contact with the fiber, and the contact behaviors were reasonable due to the SDF.

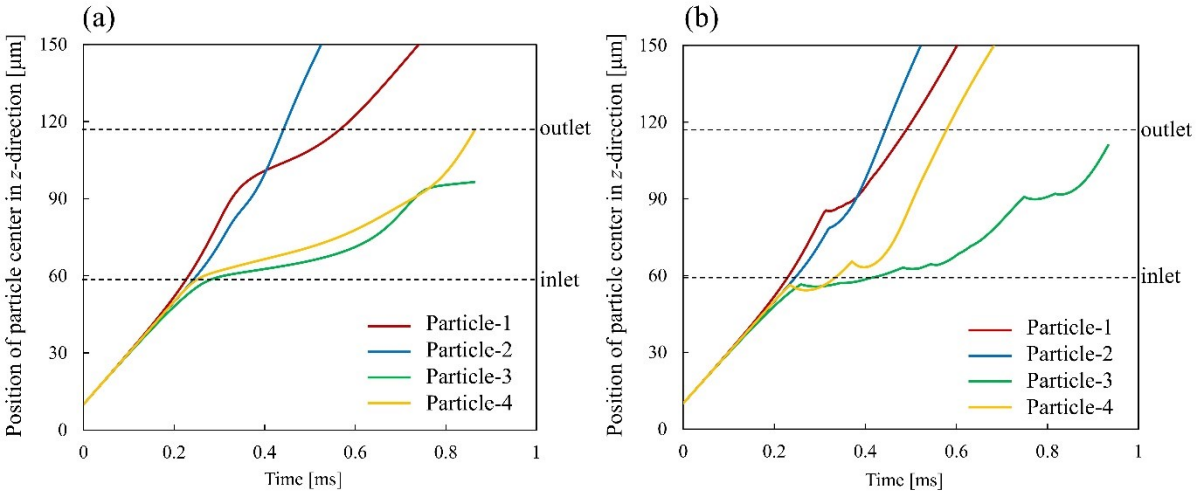

Figure 4.7 Trajectories of particles during permeation through PPS-3: (a) without SDF, and (b) with SDF

For a more detailed investigation of the particle behavior, the particle position in the main flow direction was tracked. **Figure 4.7 (a)** and **4.7 (b)** show the trajectories of the particles passing through PPS-3 without SDF and with SDF, respectively. In both cases, the positions of the particle center initially increased with time, indicating that the particles moved towards the filter domain. Without SDF (**Figure 4.7 (a)**), the position of the center of Particle 2 reached 150 μm earlier than in the other cases, showing that Particle 2 immediately left the filter domain after detaching from the fiber. This is due to the fact that Particle 2 did not penetrate into a fiber as well as the other particles, as shown in **Figure 4.6 (a1)**. For Particles 3 and 4, the slope of the particle center was significantly decreased by approximately 0.2 ms. This occurred because Particles 3 and 4 penetrated deep into the fibers, as shown in **Figure 4.6 (a2)** and **4.6 (a3)**. The slope of the particle center, which represents the particle velocity, significantly decreased when the particle was immersed in the fiber and increased gradually after the particle was detached from the fiber. With SDF (**Figure 4.7 (b)**), in the cases of Particles 1 and 2, the slopes of the particle position changed at approximately 0.3 ms, showing that Particles 1 and 2 only contacted once with the fibers (**Figure 4.6 (b2)**) and then left the filter domain (**Figure 4.6 (b3)**). This occurred because there were only a few fibers in their flow paths. On the other hand, in the case of Particle 3, the position of the particles barely changed from approximately 0.25 ms to 0.45 ms. This indicates that the particle moved on the fiber surface after contact with the fiber, as seen in **Figure 4.6 (b1)** and **4.6 (b2)**. In Particles 3 and 4, several inflection points in the slope of the particle position can be seen. Particles 3 and 4 made several contacts with the fibers because there were several fibers in their flow paths (**Figure 4.6 (b1)** – **4.6 (b3)**). With SDF, since both the snapshots and the

particle trajectories showed reasonable results, we can say that the permeation of particles through a complicated geometry of a fibrous filter was successfully simulated by applying SDF.

4.3.2 Effect of fiber orientation

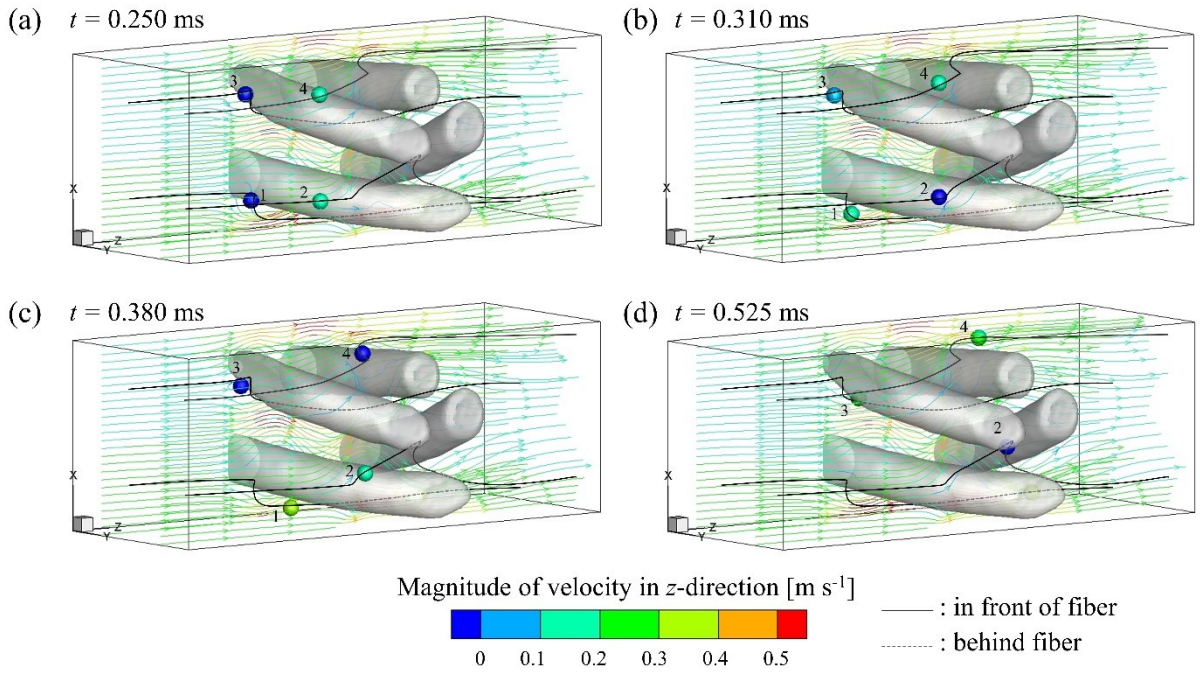

Figure 4.8 Time variation of permeation behavior of particles through PPS-1. Colors of particle and streamlines represent magnitude of velocity in *z*-direction.

In this study, we investigated the effect of the filter structure, i.e. fiber orientation, on the permeation behavior of particles through the PPS fibrous filter. First, we simulated the permeation behavior of the particles through a filter domain with a perpendicular fiber orientation. PPS-1 contains four fibers oriented relatively perpendicular to the main flow direction. The porosity of PPS-1 was ε = 0.794. **Figure 4.8** shows the snapshots of the permeation behaviors of particles through PPS-1. Particles 1 and 3 contacted the front fibers at the inlet of the filter domain (**Figure 4.8 (a)**). The dark blue color on Particles 1 and 3 indicates that the particle bounced back and moved in the opposite direction of the main flow (**Figure 4.8 (a)**). Particle 1 was pushed back by the fluid flow and then moved below the bottom fiber (**Figure 4.8 (b)** and **4.8 (c)**). The velocity of Particle 1 gradually increased as it passed through the narrow flow path and then exited from the filter domain without making further contact with the fibers (**Figure 4.8 (c)** and **4.8 (d)**). At the same time, Particle 2 contacted the upper side of the bottom fiber (**Figure 4.8 (a)** – **4.8 (c)**) and flowed through

the gap between the two front fibers (**Figure 4.8 (d)**), while Particle 3 was still restrained in front of the upper fiber because it contacted with a flat surface (**Figure 4.8 (b)** and **4.8 (c)**). After contact with the upper side of the back fiber, Particle 4 moved through the upper part of the filter domain and then exited (**Figure 4.8 (c)** and **4.8 (d)**). For PPS-1, all particles were in contact with the fibers.

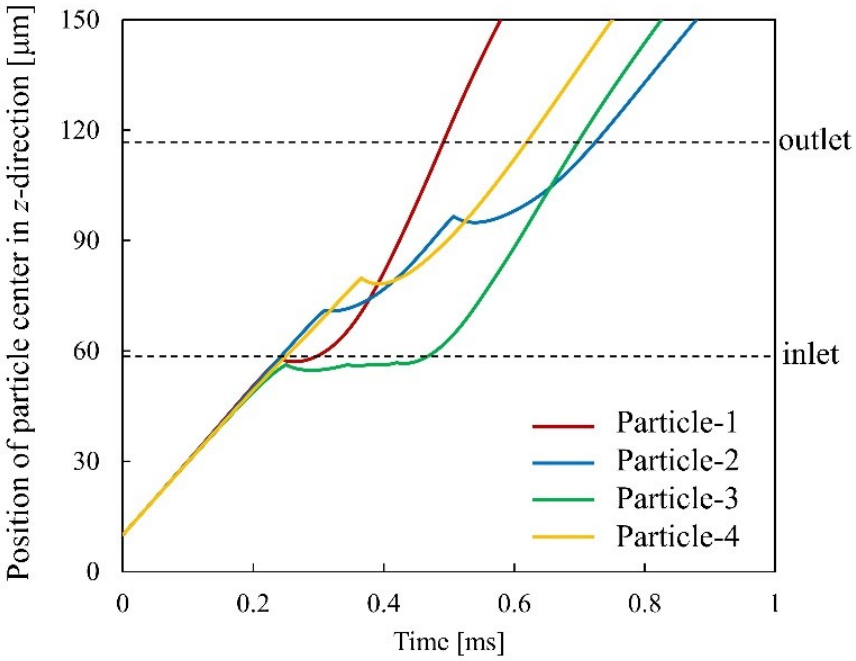

Figure 4.9 Trajectories of particles during permeation through PPS-1.

Figure 4.9 shows the trajectories of the particles passing through PPS-1. In the early stage when the particles approached the inlet of the filter domain, the position of the particle center increased with almost the same slope. This indicated that they moved at the same velocity until the particles were positioned near the inlet of the filter domain. In the case of Particle 1, the slope of the particle position was sharply changed at approximately 0.25 ms and then continuously increased with time, showing that Particle 1 only contacted once with the fiber at the inlet of PPS-1 (**Figure 4.8 (a)**) and then left from the filter domain without further contact. For Particle 2, inflection points can be seen at approximately 0.32 and 0.51 ms, indicating that Particle 2 contacted the fiber twice, as shown in (**Figure 4.8 (b)** and **4.8 (d)**). The position of the center of Particle 3 remained almost the same below approximately 60 μm, which corresponds to the inlet of PPS-1, from approximately 0.25 to 0.45 ms. This occurred because Particle 3 was restrained in front of the inlet of the filter domain, as shown in (**Figure 4.8 (a)** – **4.8 (c)**), and started to permeate to the filter domain after that (**Figure**

4.8 (d)). For Particle 4, the slope sharply changed at approximately 0.38 ms, showing that Particle 4 only contacted once, as shown in **Figure 4.8 (c)**.

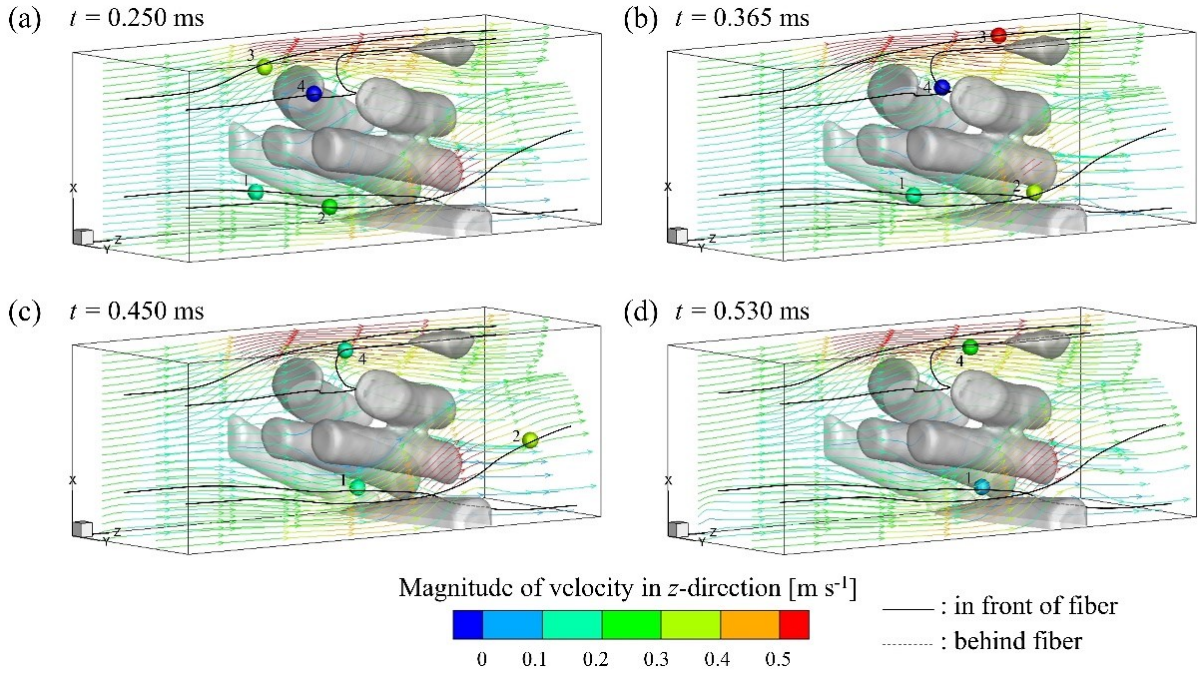

Figure 4.10 Time variation of permeation behavior of particles through PPS-2. Colors of particle and streamlines represent magnitude of velocity in *z*-direction.

Then, we investigated the permeation behavior of the particles through PPS-2. The porosity of PPS-2 was $\varepsilon = 0.780$. PPS-2 contained five fibers oriented relatively parallel to the main flow direction. **Figure 4.10** illustrates the snapshots of the permeation of particles through PPS-2. Particle 4 contacted the left upper fiber (**Figure 4.10 (a)**) and then contacted the right upper fiber (**Figure 4.10 (b)**). The other particles entered the filter domain with various velocities according to the flow paths and fluid velocity around them. Particle 3 entered the filter domain (**Figure 4.10 (a)**) and then went through the filter domain very fast (**Figure 4.10 (b)**) since it passed through the upper region of the filter domain where the fluid velocity was high. On the other hand, Particles 1 and 2 entered the filter domain at relatively the same velocity as the lower part, as shown in **Figure 4.10 (a)**. Then, the velocity of Particle 2 gradually increased since it passed through a small gap between the perpendicular and right fibers until it left the filter domain (**Figure 4.10 (b)** and **4.10 (c)**). Particle 1 was slightly in contact with the right fiber, as shown in **Figure 4.10 (d)**, then bounced downward and flowed over the perpendicular fiber. In contrast to the case of the perpendicular fibers (PPS-1), only Particles 1 and 4 contacted the fibers and the other particles flowed away without contact during the permeation process, despite having lower

porosity than PPS-1. This occurred because parallel fibers have a smaller projected contact area and a more dominant open space area than perpendicular fibers under the same porosity, and therefore the contact probability is also smaller.

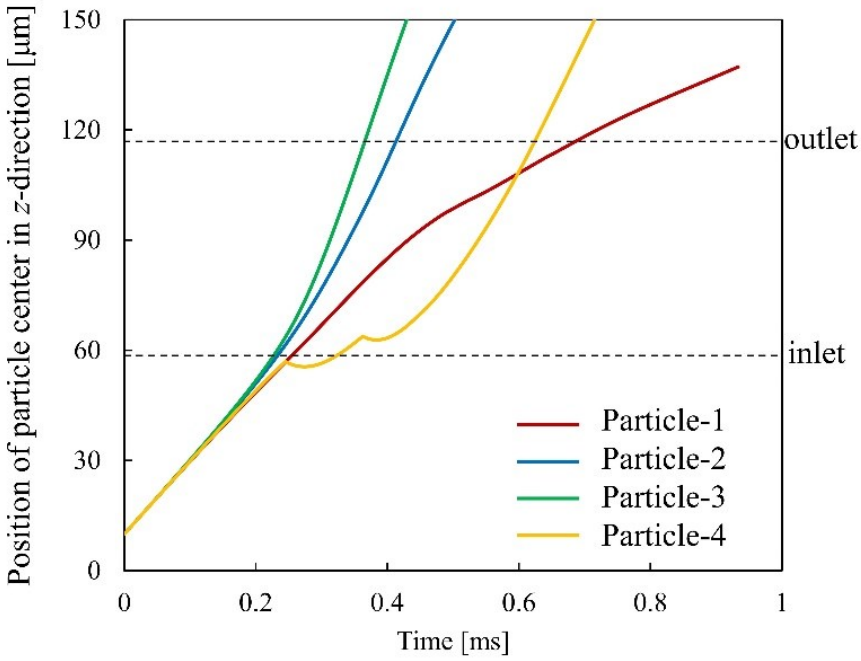

Figure 4.11 Trajectories of particles during permeation through PPS-2.

Figure 4.11 shows the trajectories of the particles passing through PPS-2. Similar to the case of PPS-1, the positions of all particle centers increased with time until the inlet of the filter domain, indicating that the particles moved with the same velocity in front of the filter domain. The position of Particle 1 continuously increased until approximately 0.45 ms when the slope of the particle position slightly decreased. This indicates that the particle velocity decreased because it contacted with the right fiber, as shown in **Figure 4.10 (d).** The trends of Particles 2 and 3 were nearly identical. The slopes were roughly equal until the position approached the inlet of the filter domain and increased thereafter. No clear inflection points could be seen in the trends of Particles 2 and 3, except at the inlet of the filter domain, which means that the particles did not contact any fibers during the permeation process. In the case of Particle 4, inflection points were found at approximately 0.25 and 0.35 ms, showing that two contacts occurred, as shown in **Figure 4.10 (a)** and **4.10 (b)**. After the second contact, the slope of the particle center, which is the particle velocity, increased gradually because the particle passed through a high-velocity region in the upper part of the filter domain (**Figure 4.10 (d)**).

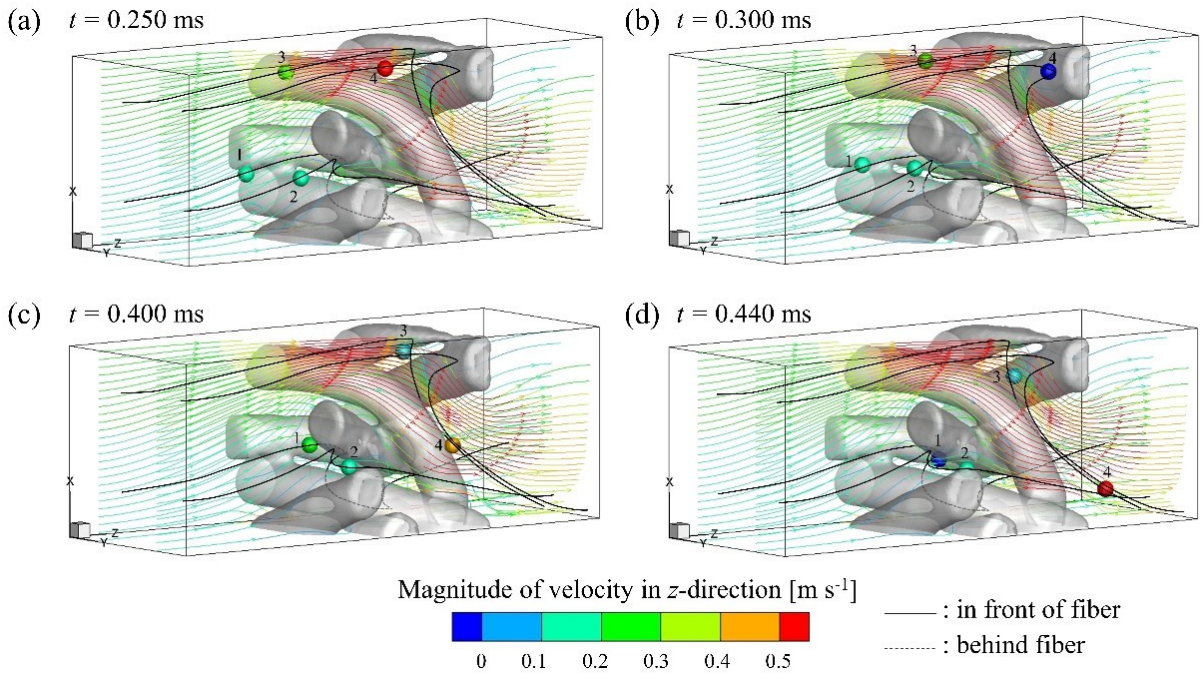

Figure 4.12 Time variation of permeation behavior of particles through PPS-4. Colors of particle and streamlines represent magnitude of velocity in z-direction.

We also investigated the behavior of particles that permeated through more complex fibers. PPS-4 contains parallel, perpendicular, and curved fibers with a porosity of $\varepsilon = 0.665$. **Figure 4.12** shows the snapshots of the permeation of particles through PPS-4. Particle 4 entered the filter domain with high velocity (**Figure 4.12 (a)**) and then bounced back after contact with the back fiber (**Figure 4.12 (a)**). Because the fluid velocity on the right side of the filter domain was high, Particle 4 was pushed back (**Figure 4.12 (c)**) and left the filter domain at high velocity (**Figure 4.12 (d)**). Particle 3 entered the filter domain through the upper side, then contacted the back fiber (**Figure 4.12 (c)**) and bounced downward (**Figure 4.12 (d)**). Particles 1 and 2 entered the filter domain through the lower part, where several fibers were tightly arranged. Particle 2 slightly contacted the bottom side of the middle parallel fiber (**Figure 4.12 (c)**) and then flowed through the gap between the fibers (**Figure 4.12 (d)**). Particle 1 was in contact with the middle fiber (**Figure 4.12 (d)**) and then bounced downward. Similar to the case of perpendicular fibers (PPS-1). All of the particles were in contact with the fibers during the permeation process. The frequency of contact increased as the number of fibers increased with more complex arrangements.

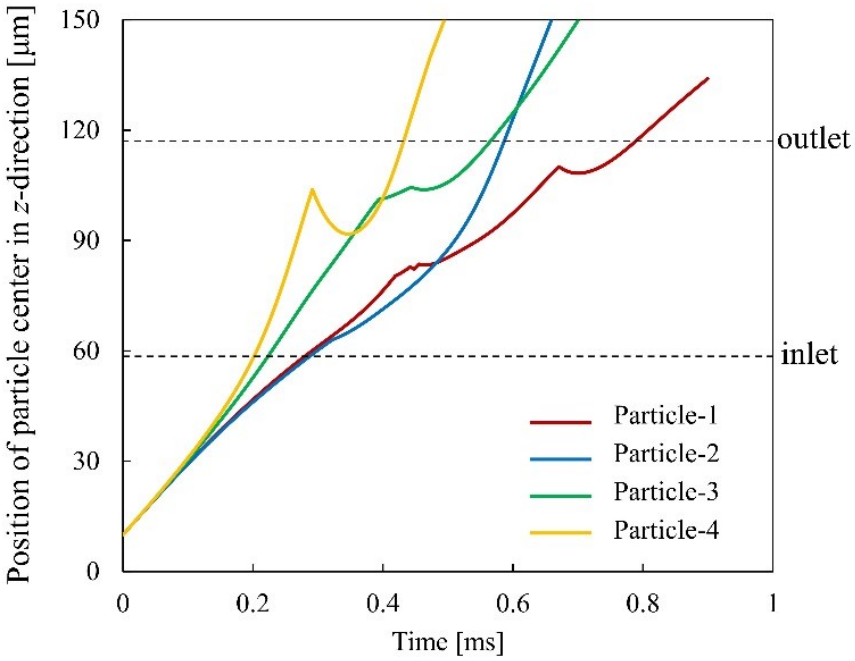

Figure 4.13 Trajectories of particles during permeation through PPS-4.

Figure 4.13 shows the trajectories of the particles passing through PPS-4. At the initial stage, 2 different trends can be seen, namely, the trend of Particles 1 and 2, which moved through the lower velocity region at the bottom of the filter domain, and trends of Particles 3 and 4, which moved through the higher-velocity region in the upper part of the filter domain, as shown in **Figure 4.12 (a)**. In the case of Particle 1, the slope of the particle position was changed at approximately 0.44 ms, showing that this particle contacted the center fiber, as shown in **Figure 4.12 (d)**. Another inflection point can be clearly seen at approximately 0.66 ms, indicating that the contact occurred again. Particle 1 was inside the filter from approximately 0.28 to 0.79 ms, which was longer than the other particles. This occurred because of the presence of several fibers around the flow path of Particle 1, which easily made contact and held Particle 1 within the filter domain. For Particle 2, the slope of the particle position increased after approximately 0.32 ms because the fluid velocity was higher owing to the narrow flow path within the filter domain. No inflection point is clearly seen, although contact is inferred because of the slight change in trajectory (**Figure 4.12 (c)**). For Particle 3, the slope of the particle position decreased from approximately 0.40 to 0.44 ms. This occurred because Particle 3 contacted the back fiber and moved down (**Figure 4.12 (c)** and **4.12 (d)**). For Particle 4, the inflection point was clearly seen at approximately 0.30 ms when the contact occurred with the back fiber, as shown in **Figure 4.12 (b)**. The position of Particle 4 was decreased until 0.35 ms, showing that Particle 4 bounced back. This

occurred because Particle 4 flowed relatively fast when the contact occurred, as shown by the red color in **Figure 4.12 (a)**.

From the above results, it can be seen that the permeation behavior of the particles changed significantly due to the differences in the filter microstructure. The particles tended to contact the fibers in a perpendicular orientation because their projected areas were larger than those in a parallel orientation. The residence time of the particle inside the filter structure differed greatly under this situation, depending on the initial position. The trajectory was significantly different even after the particles entered the filter depending on their flow path. In addition, lower porosity increased the frequency of contacts, thus increasing the duration of the particles inside the filter structure.

It is difficult to quantitatively compare our study with previous experiments studies. This is because the filter thickness and size used for the present simulation are much smaller than actual filters used for experiments. However, results correspond with the previous studies [20,21,58], where the parallel (*in-plane*) fiber orientation has a little effect on the filtration process because of less contact between particles and fiber. While the perpendicular (*through-plane*) fiber orientation has a greater effect on the filtration process due to the frequency of contact.

3.4 Conclusions

A direct numerical simulation model was developed to investigate the permeation behavior of particles through a PPS fibrous filter. This model was based on a two-way coupled scheme involving DEM and SDF, which was used to calculate the contact forces between particles and the filter surface, and a direct numerical simulation that included IBM used to calculate the hydrodynamic interaction between the fluid and the solids. X-ray CT images were used to construct realistic geometries of the microstructure of the PPS filter. We proposed a method to calculate the SDF value around the complex geometry of the filter microstructure obtained from the X-ray CT images by the phase-field model and level set method. Our numerical framework, which utilizes a simple algorithm, can efficiently calculate the contact forces between particles and the complicated geometry of fibrous filters. The permeation of four particles through several filter domains with different microstructures was simulated using this method. The effect of filter porosity and filter microstructure, such as the fiber orientation, on the permeation behavior of particles was investigated. The following conclusions can be drawn from the results:

1. SDF was successfully calculated around the filter microstructure obtained from X-ray CT images.

2. The behaviors of the particles in contact with the fiber surface can be reasonably described by applying SDF.

3. The permeation behavior of particles was significantly affected by the structure of the filter media.

4. Particles tend to contact the perpendicular orientation fibers rather than parallel orientation fibers because the projected contact area is larger in the perpendicular fibers.

We successfully demonstrated that the porosity and structure of the fibrous filter media, such as the arrangement and fiber orientation, significantly affected the particle behaviors inside the filter media. These results can be used for the optimization of the design of the bag filter where the filter with more perpendicular fiber orientation could increase the ability of the filter media to capture the particles. However, despite the fact that the pressure drop across the filter media was markedly affected by the deposition, accumulation, and adsorption of particles during the filtration process, the number of particles was limited in this study. The simulation model developed in this study can be easily extended to systems with adhesive forces and several particles. Thus, future work should increase the number of particles in the simulation and study the effect of the adhesion force between particles, and between the particles and the fiber surfaces.

References

[1] J. Steffens, J.R. Coury, Collection efficiency of fiber filters operating on the removal of nano-sized aerosol particles: I-Homogeneous fibers, Sep. Purif. Technol. 58 (2007) 99–105. https://doi.org/10.1016/j.seppur.2007.07.011.

[2] W. Tanthapanichakoon, M. Furuuchi, K. hei Nitta, M. Hata, S. Endoh, Y. Otani, Degradation of semi-crystalline PPS bag-filter materials by NO and O2 at high temperature, Polym. Degrad. Stab. 91 (2006) 1637–1644. https://doi.org/10.1016/j.polymdegradstab.2005.12.008.

[3] W. Cai, G. Hu, Oxidation degradation of polyphenylene sulfide needle felt at different

sulfuric acid dew point temperatures, High Perform. Polym. 27 (2015) 94–99. https://doi.org/10.1177/0954008314540311.

[4] M.I.F. Rozy, K. Ito, K. Une, T. Fukasawa, T. Ishigami, M. Wada, K. Fukui, A continuous-flow exposure method to determine degradation of polyphenylene sulfide non-woven bag-filter media by NO2 gas at high temperature, Adv. Powder Technol. 30 (2019) 2881–2889. https://doi.org/10.1016/j.apt.2019.08.032.

[5] M. Saleem, G. Krammer, R.U. Khan, M.S. Tahir, Influence of operating parameters on cake formation in pilot scale pulse-jet bag filter, Powder Technol. 224 (2012) 28–35. https://doi.org/10.1016/j.powtec.2012.02.016.

[6] X. Simon, D. Bémer, S. Chazelet, D. Thomas, Downstream particle puffs emitted during pulse-jet cleaning of a baghouse wood dust collector: Influence of operating conditions and filter surface treatment, Powder Technol. 261 (2014) 61–70. https://doi.org/10.1016/j.powtec.2014.04.028.

[7] M. Lupion, M. Rodriguez-Galan, B. Alonso-Fariñas, F.J. Gutierrez Ortiz, Investigation into the parameters of influence on dust cake porosity in hot gas filtration, Powder Technol. 264 (2014) 592–598. https://doi.org/10.1016/j.powtec.2014.05.042.

[8] M. Saleem, G. Krammer, Effect of filtration velocity and dust concentration on cake formation and filter operation in a pilot scale jet pulsed bag filter, J. Hazard. Mater. 144 (2007) 677–681. https://doi.org/10.1016/j.jhazmat.2007.01.094.

[9] Y.H. Joe, J. Shim, H.S. Park, Evaluation of the can velocity effect on a bag filter, Powder Technol. 321 (2017) 454–457. https://doi.org/10.1016/j.powtec.2017.08.030.

[10] M. Saleem, R.U. Khan, M.S. Tahir, G. Krammer, Experimental study of cake formation on heat treated and membrane coated needle felts in a pilot scale pulse jet bag filter using optical in-situ cake height measurement, Powder Technol. 214 (2011) 388–399. https://doi.org/10.1016/j.powtec.2011.08.037.

[11] S. Schiller, H.J. Schmid, Highly efficient filtration of ultrafine dust in baghouse filters using precoat materials, Powder Technol. 279 (2015) 96–105.

https://doi.org/10.1016/j.powtec.2015.03.048.

[12] A. Karadimos, R. Ocone, The effect of the flow field recalculation on fibrous filter loading: A numerical simulation, Powder Technol. 137 (2003) 109–119. https://doi.org/10.1016/S0032-5910(03)00132-3.

[13] H. Wang, H. Zhao, Z. Guo, C. Zheng, Numerical simulation of particle capture process of fibrous filters using Lattice Boltzmann two-phase flow model, Powder Technol. 227 (2012) 111–122. https://doi.org/10.1016/j.powtec.2011.12.057.

[14] Y. Mino, Y. Kagawa, H. Matsuyama, T. Ishigami, Permeation of oil-in-water emulsions through coalescing filter: Two-dimensional simulation based on phase-field model, AIChE J. 62 (2016) 2525–2532. https://doi.org/10.1002/aic.15206.

[15] Y. Mino, A. Hasegawa, H. Shinto, H. Matsuyama, Lattice-Boltzmann flow simulation of an oil-in-water emulsion through a coalescing filter: Effects of filter structure, Chem. Eng. Sci. 177 (2018) 210–217. https://doi.org/10.1016/j.ces.2017.11.027.

[16] T. Müller, J. Meyer, G. Kasper, Low Reynolds number drag and particle collision efficiency of a cylindrical fiber within a parallel array, J. Aerosol Sci. 77 (2014) 50–66. https://doi.org/10.1016/j.jaerosci.2014.07.007.

[17] T. Ishigami, H. Fuse, S. Asao, D. Saeki, Y. Ohmukai, E. Kamio, H. Matsuyama, Permeation of Dispersed Particles through a Pore and Transmembrane Pressure Behavior in Dead-End Constant-Flux Microfiltration by Two-Dimensional Direct Numerical Simulation, Ind. Eng. Chem. Res. 52 (2013) 4650–4659. https://doi.org/10.1021/ie302448x.

[18] T. Ando, K. Akamatsu, S. ichi Nakao, M. Fujita, Simulation of fouling and backwash dynamics in dead-end microfiltration: Effect of pore size, J. Memb. Sci. 392–393 (2012) 48–57. https://doi.org/10.1016/j.memsci.2011.11.051.

[19] R. Tao, M. meng Yang, S. qing Li, Filtration of micro-particles within multi-fiber arrays by adhesive DEM-CFD simulation, J. Zhejiang Univ. Sci. A. 19 (2018) 34–44. https://doi.org/10.1631/jzus.A1700156.

[20] S. Fotovati, H. Vahedi Tafreshi, B. Pourdeyhimi, Influence of fiber orientation distribution on performance of aerosol filtration media, Chem. Eng. Sci. 65 (2010) 5285–5293. https://doi.org/10.1016/j.ces.2010.06.032.

[21] A.K. Pradhan, D. Das, R. Chattopadhyay, S.N. Singh, Effect of 3D fiber orientation distribution on particle capture efficiency of anisotropic fiber networks, Powder Technol. 249 (2013) 205–207. https://doi.org/10.1016/j.powtec.2013.08.011.

[22] S.A. Hosseini, H.V. Tafreshi, 3-D simulation of particle filtration in electrospun nanofibrous filters, Powder Technol. 201 (2010) 153–160. https://doi.org/10.1016/j.powtec.2010.03.020.

[23] C. Yue, Q. Zhang, Z. Zhai, Numerical simulation of the filtration process in fibrous filters using CFD-DEM method, J. Aerosol Sci. 101 (2016) 174–187. https://doi.org/10.1016/j.jaerosci.2016.08.004.

[24] M.I.F. Rozy, M. Ueda, T. Fukasawa, T. Ishigami, K. Fukui, Direct numerical simulation and experimental validation of flow resistivity of nonwoven fabric filter, AIChE J. 66 (2020). https://doi.org/10.1002/aic.16832.

[25] M. Ueda, M.I.F. Rozy, T. Fukasawa, T. Ishigami, K. Fukui, Phase-Field Simulation of the Coalescence of Droplets Permeating through a Fibrous Filter Obtained from X-ray Computed Tomography Images: Effect of the Filter Microstructure, Langmuir. 36 (2020) 4711–4720. https://doi.org/10.1021/acs.langmuir.0c00640.

[26] M. Sakai, H. Takahashi, C.C. Pain, J.P. Latham, J. Xiang, Study on a large-scale discrete element model for fine particles in a fluidized bed, Adv. Powder Technol. 23 (2012) 673–681. https://doi.org/10.1016/j.apt.2011.08.006.

[27] P.W. Cleary, R. Morrisson, S. Morrell, Comparison of DEM and experiment for a scale model SAG mill, Int. J. Miner. Process. 68 (2003) 129–165. https://doi.org/10.1016/S0301-7516(02)00065-0.

[28] K. Yokoi, Numerical method for interaction between multiparticle and complex structures, Phys. Rev. E - Stat. Nonlinear, Soft Matter Phys. 72 (2005) 1–7. https://doi.org/10.1103/PhysRevE.72.046713.

[29] Y. Shigeto, M. Sakai, Arbitrary-shaped wall boundary modeling based on signed distance functions for granular flow simulations, Chem. Eng. J. 231 (2013) 464–476. https://doi.org/10.1016/j.cej.2013.07.073.

[30] H. Yao, Y. Mori, K. Takabatake, X. Sun, M. Sakai, Numerical investigation on the influence of air flow in a die filling process, J. Taiwan Inst. Chem. Eng. 90 (2018) 9–17. https://doi.org/10.1016/j.jtice.2017.11.031.

[31] Y. Mori, C.Y. Wu, M. Sakai, Validation study on a scaling law model of the DEM in industrial gas-solid flows, Powder Technol. 343 (2019) 101–112. https://doi.org/10.1016/j.powtec.2018.11.015.

[32] M. Sakai, Y. Mori, X. Sun, K. Takabatake, Recent progress on mesh-free particle methods for simulations of multi-phase flows: A review, KONA Powder Part. J. 37 (2020) 132–144. https://doi.org/10.14356/kona.2020017.

[33] S. James A., Level Set Methods and Fast Marching Methods, Cambridge University Press, Cambridge, UK, 1999.

[34] Y. Kagawa, T. Ishigami, K. Hayashi, H. Fuse, Y. Mino, H. Matsuyama, Permeation of concentrated oil-in-water emulsions through a membrane pore: Numerical simulation using a coupled level set and the volume-of-fluid method, Soft Matter. 10 (2014) 7985–7992. https://doi.org/10.1039/c4sm00705k.

[35] Z. Wang, J. Yang, B. Koo, F. Stern, A coupled level set and volume-of-fluid method for sharp interface simulation of plunging breaking waves, Int. J. Multiph. Flow. 35 (2009) 227–246. https://doi.org/10.1016/j.ijmultiphaseflow.2008.11.004.

[36] S.J. Cummins, M.M. Francois, D.B. Kothe, Estimating curvature from volume fractions, Comput. Struct. 83 (2005) 425–434. https://doi.org/10.1016/j.compstruc.2004.08.017.

[37] J.W. Cahn, J.E. Hilliard, Free energy of a nonuniform system. I. Interfacial free energy, J. Chem. Phys. 28 (1958) 258–267. https://doi.org/10.1063/1.1744102.

[38] K. Hayashi, Application of Cahn-Hilliard Equation to the Evaluation of Surface

Tension Force, Japanese J. Multiph. Flow. 20 (2006) 244–251.

[39] T. Kajishima, S. Takiguchi, H. Hamasaki, Y. Miyake, Turbulence Structure of Particle-Laden Flow in a Vertical Plane Channel Due to Vortex Shedding, JSME Int. J. Ser. B. 44 (2001) 526–535. https://doi.org/10.1299/jsmeb.44.526.

[40] Y. Mino, H. Shinto, S. Sakai, H. Matsuyama, Effect of internal mass in the lattice Boltzmann simulation of moving solid bodies by the smoothed-profile method, Phys. Rev. E. 95 (2017) 1–10. https://doi.org/10.1103/PhysRevE.95.043309.

[41] Y. Nakayama, R. Yamamoto, Simulation method to resolve hydrodynamic interactions in colloidal dispersions, Phys. Rev. E - Stat. Nonlinear, Soft Matter Phys. 71 (2005) 1–7. https://doi.org/10.1103/PhysRevE.71.036707.

[42] P.A. Cundall, O.D.L. Strack, A discrete numerical model for granular assemblies, Géotechnique. 29 (1979) 47–65. https://doi.org/10.1680/geot.1979.29.1.47.

[43] X. Sun, M. Sakai, Numerical simulation of two-phase flows in complex geometries by using the volume-of-fluid/immersed-boundary method, Chem. Eng. Sci. 139 (2016) 221–240. https://doi.org/10.1016/j.ces.2015.09.031.

[44] X. Sun, M. Sakai, Immersed boundary method with artificial density in pressure equation for modeling flows confined by wall boundaries, J. Chem. Eng. Japan. 50 (2017) 161–169. https://doi.org/10.1252/jcej.16we115.

[45] Y. Tsuji, T. Kawaguchi, T. Tanaka, Discrete particle simulation of two-dimensional fluidized bed, Powder Technol. 77 (1993) 79–87. https://doi.org/10.1016/0032-5910(93)85010-7.

[46] Y. Tsunazawa, Y. Shigeto, C. Tokoro, M. Sakai, Numerical simulation of industrial die filling using the discrete element method, Chem. Eng. Sci. 138 (2015) 791–809. https://doi.org/10.1016/j.ces.2015.09.014.

[47] M. Sakai, Y. Shigeto, G. Basinskas, A. Hosokawa, M. Fuji, Discrete element simulation for the evaluation of solid mixing in an industrial blender, Chem. Eng. J. 279 (2015) 821–839. https://doi.org/10.1016/j.cej.2015.04.130.

[48] G. Basinskas, M. Sakai, Numerical study of the mixing efficiency of a ribbon mixer using the discrete element method, Powder Technol. 287 (2016) 380–394. https://doi.org/10.1016/j.powtec.2015.10.017.

[49] Y. Mori, K. Takabatake, Y. Tsugeno, M. Sakai, On artificial density treatment for the pressure Poisson equation in the DEM-CFD simulations, Powder Technol. 372 (2020) 48–58. https://doi.org/10.1016/j.powtec.2020.05.116.

[50] K. Takabatake, M. Sakai, Flexible discretization technique for DEM-CFD simulations including thin walls, Adv. Powder Technol. 31 (2020) 1825–1837. https://doi.org/10.1016/j.apt.2020.02.017.

[51] M. Sussman, P. Smereka, S. Osher, A Level Set Approach for Computing Solutions to Incompressible Two-Phase Flow, J. Comput. Phys. 114 (1994) 146–159. https://doi.org/10.1006/jcph.1994.1155.

[52] M. Sussman, E. Fatemi, P. Smereka, S. Osher, An improved level set method for incompressible two-phase flows, Comput. Fluids. 27 (1998) 663–680. https://doi.org/10.1016/S0045-7930(97)00053-4.

[53] A.J. Chorin, The numerical solution of the Navier-Stokes equations for an incompressible fluid, Bull. Am. Math. Soc. 73 (1967) 928–932. https://doi.org/10.1090/S0002-9904-1967-11853-6.

[54] T.. Pulliam, D.. Chaussee, A diagonal form of an implicit approximate-factorization algorithm, J. Comput. Phys. 39 (1981) 347–363. https://doi.org/10.1016/0021-9991(81)90156-X.

[55] Y. Choi, D. Jeong, J. Kim, Curve and Surface Smoothing Using a Modified Cahn-Hilliard Equation, Math. Probl. Eng. 2017 (2017). https://doi.org/10.1155/2017/5971295.

[56] Z. Pan, X. Zhang, Z. Sun, F. Jiang, L. Lin, Y. Liang, M. Tang, J. Wang, High fidelity simulation of ultrafine PM filtration by multiscale fibrous media characterized by a combination of X-ray CT and FIB-SEM, J. Memb. Sci. 620 (2021) 118925. https://doi.org/10.1016/j.memsci.2020.118925.

[57] Y. Mino, S. Sakai, H. Matsuyama, Simulations of particulate flow passing through membrane pore under dead-end and constant-pressure filtration condition, Chem. Eng. Sci. 190 (2018) 68–76. https://doi.org/10.1016/j.ces.2018.05.061.

[58] J. Happel, Viscous flow relative to arrays of cylinders, AIChE J. 5 (1959) 174–177. https://doi.org/10.1002/aic.690050211.

Chapter 5

Summary and Conclusions

Polyphenylene sulfide (PPS) filter media has widely used in many filtration applications. Thus, an improvement in the filtration performance and durability of the filter media is very useful for technical applications. This dissertation was aimed at studying the improvement of the performance and durability of filter media by investigating using both experimental and numerical simulations. The major highlights of this dissertation are as follows:

1. NO_2 gas at high-temperature conditions has a very strong effect on the degradation of polyphenylene sulfide (PPS) filter media. The tensile strength and elongation of the PPS filter media for both machine direction (MD) and transverse direction (TD) significantly decreased by increasing the exposure time to NO_2 gas. Their reductions was observed more markedly in TD than in the MD. The physical appearance of the PPS fiber was damaged during exposure to NO_2 gas showed by many protrusions on the surface, cracking, and splitting, which ultimately reduced the tensile strength of the filter media. The exposure to NO_2 gas also enhanced the oxidation of atom S in the PPS and introduced new oxygen-containing functional groups such as –SO– and O=S=O into the PPS molecular structure. An unreacted core model in the cylindrical coordinate system can be applied as a model to estimate the change in NO_2 concentration in the exhaust gas, which is in good agreement with the experimental data.
2. The permeation of gas through a fibrous filter was successfully performed by coupling computational fluid dynamics and the immersed boundary method. The realistic geometry of the fibrous filter successfully re-created using filter image processing utilizing X-ray CT images of PPS and PI fibrous filters. The robustness of our method was successfully validated by comparing the simulated pressure drop of our numerical method with the experimental data and existing empirical equations where the results were in good agreement. Our method also could be used to investigate the permeability of PPS and PI fibrous filter, where the permeability of the PI filter was lower than the PPS filter under the same porosity conditions because the drag force acting on a single PI fiber was higher than on a single PPS fiber.
3. As a further application of X-ray CT images of fibrous filter, we successfully calculated the signed distance function around the complex filter microstructure by using the Phase-field model and the Level set method. By this technique, we could reasonably

describe the behaviors of the particles in contact with the fiber surface. We also could investigate the permeation behavior of particles through PPS fibrous filter. Our results show that the permeation behavior of particles was significantly affected by porosity and the structure of the filter media such as the arrangement and fiber orientation. The particles tend to contact the perpendicular orientation fibers rather than parallel orientation fibers because the projected contact area is larger in the perpendicular fibers. These results can be used for the optimization of the design of the bag filter where the filter with more perpendicular fiber orientation could increase the ability of the filter media to capture the particles and increasing the collection efficiency.

The present research represents a promising method to investigate the permeation process both particles and fluid through complex porous media using numerical simulation. Moreover, we expect that our method could be used to improve the performance of filter media used for the filtration system. However, our present is still limited on two-phase flow, and the interaction force between particles and particle-filter is also still neglected. Thus, for further research, the number of particles should be increased by considering interaction forces such as van der Waals force and electrostatic force and extend the simulation model into a three-phase flow simulation. Other types of filter media and harmful gas in various concentrations and temperatures should be used regarding the investigation of the durability of the filter media.

List of Publications

1. **M.I.F. Rozy**, K. Ito, K. Une, T. Fukasawa, T. Ishigami, M. Wada, K. Fukui, A continuous-flow exposure method to determine degradation of polyphenylene sulfide non-woven bag-filter media by NO2 gas at high temperature, ***Advanced Powder Technology***. 30 (2019) 2881–2889.
2. **M.I.F. Rozy**, M. Ueda, T. Fukasawa, T. Ishigami, K. Fukui, Direct numerical simulation and experimental validation of flow resistivity of nonwoven fabric filter, ***AIChE Journal***. 66 (2020).
3. M. Ueda, **M.I.F. Rozy**, T. Fukasawa, T. Ishigami, K. Fukui, Phase-Field Simulation of the Coalescence of Droplets Permeating through a Fibrous Filter Obtained from X-ray Computed Tomography Images: Effect of the Filter Microstructure, ***Langmuir***. 36 (2020) 4711–4720.
4. **M.I.F. Rozy**, Y. Maemoto, M. Ueda, T. Fukasawa, T. Ishigami, K. Fukui, M. Sakai, Y. Mino, K. Gotoh, Direct numerical simulation of permeation of particles through a realistic fibrous filter obtained from X-ray computed tomography images utilizing signed distance function, ***Powder Technology***. 385 (2021) 131–143.
5. **M.I.F. Rozy**, M. Ueda, T. Fukasawa, T. Ishigami, K. Fukui, Direct numerical simulation of flow resistivity and oil droplets coalescence on X-ray CT images of nonwoven fabric filter. The 18th Asian Pacific Confederation of Chemical Engineering Congress (APCChE 2019).

Acknowledgment

Praise be to the Allah SWT almighty for His merciful blessing.

I would like to express my deepest gratitude to Professor Kunihiro Fukui who allowed me to work in his group and gave his valuable time and expertise to make this dissertation possible. I am also grateful to Associate Professor Toru Ishigami and Assistant Professor Tomonori Fukasawa who helped and taught me to gather the knowledge needed to compose this dissertation.

Special gratitude to Professor Satoshi Nakai and Associate Professor Shin-ichi Kihara for the constructive critics, suggestions, and insights to improve the quality of this dissertation.

I would like to thank all my former and current colleagues of the Fine Particle Technology Laboratory, special mention goes to Masaki Ueda, Yuto Maemoto, Kazuki Une, Keiya Ito, Genki Ichiba who assisted me and collaborated with me during my research. Furthermore, I would like to acknowledge all my co-authors Assoc. Prof. Mikio Sakai from University of Tokyo, Prof. Kuniaki Gotoh and Assist. Prof. Yasushi Mino from Okayama University for the collaboration work and constructive advice improving the quality of the manuscripts and this dissertation.

I am also indebted to the Ministry of Education, Culture, Sports, Science, and Technology of Japan (MEXT) for the master and doctoral scholarship and Hosokawa Foundation for the research fund.

I am truly grateful to my friends in Indonesia and Higashi Hiroshima, special mention for Ratri for their ongoing support and continual encouragement. My acknowledgment would be incomplete without thanking the biggest source of my strength and motivation, my beloved mother, Sriati, my father, Subandi, and my brother Yoga. I would like to dedicate this work to them for listening and praying for me continuously.

Mohammad Irwan Fatkhur Rozy